



Universidad  
Carlos III de Madrid

**Department of Thermal and Fluids Engineering**

**UNDERGRADUATE THESIS**

**TOWARDS THE NUMERICAL  
SIMULATION OF THE FILLING  
PROCESS OF THE LEFT VENTRICLE  
OF THE HEART**

Author: Susana Izquierdo Bermúdez

Advisors: Juan Carlos del Álamo

Javier Rodríguez Rodríguez

Óscar Flores

Leganés, October 2010



**Title:** Towards the numerical simulation of the filling process of the left ventricle of heart

**Author:** Susana Izquierdo Bermúdez

**Advisors:** Juan Carlos del Álamo

Javier Rodríguez Rodríguez

Óscar Flores

## EL TRIBUNAL

Presidente:

\_\_\_\_\_

Vocal:

\_\_\_\_\_

Secretario:

\_\_\_\_\_

Realizado el acto de defensa y lectura del Proyecto Fin de Carrera el día \_\_ de \_\_\_\_\_ de 20\_\_ en Leganés, en la Escuela Politécnica Superior de la Universidad Carlos III de Madrid, acuerda otorgarle la CALIFICACIÓN de

VOCAL

SECRETARIO

PRESIDENTE





*A mis padres y a mi hermana*



## **AGRADECIMIENTOS**

Quiero comenzar con un grandísimo agradecimiento a mis directores de proyecto. A Javier Rodríguez por haber confiado en mí todos estos años, por haberme brindado la oportunidad de trabajar junto a él, por su continuo apoyo y por haberme abierto las puertas para poder realizar este proyecto en la Universidad de California, San Diego (UCSD). A Juan Carlos del Álamo por haberme introducido en este interesantísimo proyecto y haberme mostrado la increíble labor de investigación que su grupo desarrolla en la UCSD en el ámbito de la bioingeniería. Su inestimable ayuda ha sido fundamental para el desarrollo de este proyecto y a él debo agradecerle lo mucho que he aprendido. También quiero agradecer a Oscar Flores el gran apoyo que me ha brindado. Su preocupación y amabilidad han sido de gran ayuda.

A mis padres tengo que agradecerles todo lo que soy. Su apoyo incondicional y cariño han sido fundamentales tanto en los buenos como en los malos momentos. Ellos me han ayudado a dar cada paso de mi camino.

A mi hermana. Su constante motivación y admiración me han animado a superarme cada día. Su eterna compañía y apoyo ha sido un pilar sólido todos estos años.

A mis amigos de siempre, por los muchísimos grandes momentos que hemos compartido durante tantos años de amistad. En especial quiero agradecer a Isa y a Alex su infinito apoyo y confianza. Ellos han sido y serán siempre una parte fundamental mi de vida.

A mis amigos de la Universidad que han conseguido que la etapa que estoy a punto de cerrar sea sin duda una de las más felices de toda mi vida. Leticia, Reyes y Almudena han sabido siempre dar el toque de alegría y diversión. Carlos, Manuel y Jacobo han sido para mí una gran motivación y han demostrado en innumerables ocasiones que siempre estarán ahí. No hay palabras para agradecer la amistad, apoyo y confianza de todos ellos.

Por último, no puedo olvidarme de todo el resto de mi familia y amigos. Todos han aportado su granito de arena a mi vida y son responsables de un modo u otro de que hoy sea lo que soy.

Muchas gracias a todos.



## **ABSTRACT**

Heart failure is a leading cause of death nowadays. A high proportion of patients with heart failure experience asynchronous myocardial contraction. Cardiac resynchronization therapy is intended to re-establish the synchrony in the motion of the ventricles. However, about 40% of the patients do not respond favorable to this therapy for reasons that are not fully understood. A better knowledge of the ventricular flow under controlled synchrony condition is needed to understand the benefits of cardiac resynchronization therapy.

The flow of blood generated by the heart is the result of synchronized electromechanical events and fluid dynamics processes. During diastole, filling period of the cardiac cycle, the fluid dynamics of the left ventricle are governed by a large vortex ring that contributes to an efficient channeling of the blood coming from the mitral valve and prevents blood stagnation, helping to wash out the blood mass coming into the left ventricle. The ultimate outcome expected from this research is to understand the dependence of the time evolution of this vortex on the duration of the left ventricle filling phases, and to determine how this dependence affects the blood flow transport in the left ventricle and global ventricular function.

This work is part of an interdisciplinary project involving experts from different fields, ranging from cardiology, echocardiography and magnetic resonance imaging, to fluid dynamics, computational mechanics and image processing. The specific aim of this thesis is to develop a numerical code in FORTRAN95 to simulate the filling process of the left ventricle of the heart in order to study ventricular hemodynamic before and after the implantation of biventricular pacers.

From the numerical point of view, a key factor of the flow that needs to be modeled is the existence of moving boundaries. The immersed boundary method implemented here allows us to deal with moving geometries in Cartesian structured grids, thereby requiring significantly less computational time than competing methods without sacrificing accuracy. A 2D flow solver based on finite differences in a standard geometry has been developed. The idea is to start with a simple problem where the complexity can be increased step by step. Computationally efficient algorithms have been used to integrate in time the Navier-Stokes equations and to solve the linear system of equations resulting from the spatiotemporal discretization. The capabilities and limitations of the numerical code have been illustrated by applying the code to canonical flow problems. To reach the final aim of simulating numerically the filling process of the left ventricle of the heart, the present code should be extended to three dimensions, refined and parallelized to allow for multi-processors simulations.



## **RESUMEN**

Las enfermedades cardiovasculares son una de las principales causas de muerte en el mundo actual. El latido asíncrono del ventrículo izquierdo y derecho del corazón es el responsable de una proporción importante de los fallos cardíacos. La Terapia de Resincronización Cardíaca mejora la coordinación de las contracciones del corazón mediante marcapasos que estimulan ambos ventrículos (marcapasos biventriculares) para que se contraigan de manera simultánea. En torno al 40% de los pacientes no responden adecuadamente a esta terapia. Por ello es muy importante entender mejor cómo es el transporte de sangre en el corazón.

El flujo que se produce en el corazón es el resultado de la sincronización de una serie de eventos electromecánicos y procesos fluidodinámicos. Durante la diástole, periodo del ciclo cardíaco durante el cual se produce el llenado del corazón, la fluidodinámica del ventrículo izquierdo está gobernada por un vórtice que contribuye a canalizar la sangre que viene de la válvula mitral y evita el estancamiento de la misma en el ventrículo. El propósito final de esta investigación es entender la dependencia de la evolución temporal de este vórtice durante el periodo de llenado del ventrículo y determinar cómo afecta al transporte de flujo sanguíneo en el ventrículo izquierdo y a la función ventricular global.

El trabajo que aquí se presenta es parte de un proyecto interdisciplinar en el que están involucrados expertos de diferentes campos, abarcando desde cardiología y eco-cardiografía hasta fluidodinámica, mecánica computacional y procesamiento de imágenes. El objetivo particular de este trabajo está dentro del desarrollo de un código numérico en FORTRAN95 para simular el proceso de llenado del ventrículo izquierdo del corazón que ayudará a entender mejor los cambios en la dinámica ventricular antes y después de la implantación de marcapasos biventriculares. Este proyecto da los primeros pasos hacia dicho objetivo.

Desde el punto de vista numérico, el primer asunto a superar es la existencia de fronteras que se mueven. El método de las fronteras embebidas usado aquí, permite tratar dicha geometría en mallas estructurales que no se adaptan al cuerpo requiriendo menor coste computacional que otros métodos. Se ha desarrollado un modelo para resolver un flujo bidimensional para una geometría estándar. La idea es comenzar con un problema sencillo al que se pueden ir incorporando las complejidades inherentes al problema a modelar. Se ha utilizado un algoritmo computacionalmente eficiente para integrar en el tiempo las ecuaciones de Navier-Stokes y para resolver el sistema lineal de ecuaciones que resulta de la discretización espaciotemporal. Las capacidades y limitaciones del código numérico se ilustran por medio de una serie de ejemplos. Para alcanzar el objetivo final de simular numéricamente el llenado del ventrículo izquierdo del corazón, el código desarrollado tiene que ser extendido a tres dimensiones, refinado y paralelizado para permitir simulaciones con procesadores múltiples.





# CONTENTS

<b>Chapter 1.....</b>	<b>17</b>
<b>1 Introduction and aims.....</b>	<b>17</b>
1.1 Introduction.....	17
1.2 Approach .....	19
1.3 Objectives .....	20
1.4 Content.....	20
<b>Chapter 2.....</b>	<b>23</b>
<b>2 The cardiovascular system .....</b>	<b>23</b>
2.1 Circulation.....	23
2.1.1 Circulation cycle.....	24
2.2 The heart .....	25
2.2.1 Introduction.....	25
2.2.2 Cardiac cycle .....	26
2.2.2.1 Pressure - Volume cycle .....	29
2.2.2.2 Cardiac muscle.....	30
2.2.2.3 Factors affecting the performance of the heart.....	30
2.2.3 Electric system.....	30
2.2.3.1 Electrocardiogram .....	32
2.2.4 Heart valves .....	34
2.2.4.1 Mitral valve.....	34
2.2.4.2 Aortic Valve.....	34
2.3 Blood.....	35
2.4 Vessels .....	36
2.4.1 Vessels flow description .....	37
<b>Chapter 3.....</b>	<b>39</b>
<b>3 Diastology .....</b>	<b>39</b>
3.1 Ventricular diastolic filling and function.....	39
3.1.1 Definition of diastole .....	39
3.1.2 Measurements of diastolic function.....	40
3.2 Flow propagation inside the ventricle.....	41
3.3 Doppler assessment of diastolic LV filling.....	43

3.3.1	Introduction.....	43
3.3.2	Normal transmitral Doppler flow velocity pattern.....	43
3.3.3	Doppler tissue velocity imaging.....	45
3.3.4	Color M-mode transmitral flow.....	45
3.3.5	Normal Pulmonary vein Doppler Flow velocity pattern.....	46
3.4	Diastolic heart failure .....	47
3.4.1	Introduction.....	47
3.4.2	Definition of diastolic dysfunction.....	48
3.4.3	Causes of diastolic dysfunction .....	48
3.4.4	Assessment of diastolic dysfunction .....	48
3.4.5	Stages of diastolic dysfunction .....	49
3.5	Pacing and diastolic heart failure .....	50
3.5.1	Introduction.....	50
3.5.2	Cardiac resynchronization therapy.....	50
3.5.2.1	Optimization of atrioventricular (AV) delay and diastolic function .....	51
3.5.2.2	Optimization of intraventricular (VV) delay and diastolic function.....	52
<b>Chapter 4</b>	<b>.....</b>	<b>53</b>
<b>4</b>	<b>Fluid dynamic model.....</b>	<b>53</b>
4.1	Introduction.....	53
4.2	The inlet flow .....	54
4.3	The domain.....	55
<b>Chapter 5</b>	<b>.....</b>	<b>57</b>
<b>5</b>	<b>Numerical model .....</b>	<b>57</b>
5.1	Introduction.....	57
5.2	Mathematical model .....	58
5.3	Mesh discretization .....	59
5.3.1	Introduction.....	59
5.3.2	Types of grids.....	59
5.3.2.1	Body conformal grids.....	59
5.3.2.2	Non body conformal grids: Immersed Boundaries .....	60
5.3.3	Choice of the grid .....	61
5.3.4	Variable arrangement on the grid .....	62
5.4	Discretization of the equations .....	64
5.4.1	Spatial discretization .....	64

5.4.1.1	Approximating derivatives.....	64
5.4.2	Temporal discretization.....	65
5.4.2.1	Theoretical basis.....	66
5.4.2.2	Integration procedure .....	67
5.4.3	Immersed boundaries.....	69
5.4.3.1	Description of the method .....	69
5.4.3.2	Numerical procedure.....	70
5.4.3.3	Interpolation techniques .....	70
5.4.4	Properties of the numerical scheme .....	75
5.4.4.1	Consistency.....	75
5.4.4.2	Stability .....	75
5.4.4.3	Convergence .....	75
5.5	Solution of the algebraic system of equations.....	76
5.5.1	Introduction.....	76
5.5.2	Direct methods.....	77
5.5.2.1	Gauss elimination .....	77
5.5.2.2	Lu decomposition .....	78
5.5.3	Iterative methods .....	78
5.5.3.1	Methods analyzed in this study.....	78
5.5.3.2	Sparse Iterative Methods .....	84
5.5.3.3	Multigrid .....	85
5.5.4	Quantitative analysis .....	86
5.5.4.1	Direct Methods versus Traditional Iterative Methods .....	86
5.5.4.2	Full Direct Methods versus Sparse Iterative Methods .....	89
5.6	Validation of the code .....	90
5.6.1	Introduction.....	90
5.6.2	CASE 1: Cavity flow. ....	91
5.6.3	CASE 2: Lamb-Oseen vortex .....	92
5.6.3.1	Introduction.....	92
5.6.3.2	Lamb-Oseen vortex.....	92
5.6.3.3	Code evolution .....	95
5.6.4	CASE 3: Immersed circle .....	103
5.6.4.1	Introduction.....	103

5.6.4.2	Case 3a. Circle in presence of a cavity flow.....	103
5.6.4.3	Case 3b. Circle in presence of a vortex.....	108
5.6.4.4	Cases 3c and 3d. Moving circle.....	109
<b>Chapter 6.....</b>		<b>113</b>
<b>6</b>	<b>Conclusions and future work.....</b>	<b>113</b>
6.1	Conclusions.....	113
6.2	Future work .....	114
<b>References.....</b>		<b>117</b>

# Chapter 1

---

## 1 Introduction and aims

Nowadays, heart failure is a challenging health problem in developed countries. In about half of the patients, heart failure is caused by impaired ventricular filling. Experimental studies have described complex flow patterns inside the human left ventricle suggesting that a large vortex ring that forms during early diastole contributes decisively to the overall cardiac function. This chapter is an introduction to the topic, describing the main features and the significance of the problem. This work is a part of a broader interdisciplinary project that involves experts from different fields, ranging from cardiology, echocardiography and magnetic resonance imaging, to fluid dynamics, computational mechanics and image processing. The general approach of the project is described, emphasizing on the particular aims of this particular work. At the end of the chapter, the structure of the work is presented.

### 1.1 Introduction

Heart disease remains a leading cause of death worldwide and has become a challenging health problem in developed countries. In Spain alone, more than 7 hundred thousand people suffer symptomatic **heart failure (HF)** (1). An aging population and improved survival rates of other heart diseases are associated with an increase of the HF incidence in the last decade (2, 3). Cardiovascular diseases are also very costly. According to a study developed by researchers in the University of Oxford and published in the “European Heart Journal”, only in Spain the costs ascend to 7.000 million Euros per year. In Europe, about 181.000 million are spent on to treat cardiovascular diseases every year.

Diastolic heart failure is caused by impaired ventricular filling and is present in about half of all heart failure patients (4) (5). Studies have shown that heart failure patients who do not receive effective treatments to

improve heart function have a poor quality of life and a high risk of death. The mortality rate for these individuals is high with 74 percent passing away within five years (4). Thus, better knowledge of the pathology and time evolution of the HF syndrome, as well as new diagnosis tools, are required.

The dynamics of the cardiac **left ventricle (LV)** during diastolic filling may play a critical role in dictating overall cardiac health. The inherent complexity of LV diastole, in its electrical, muscular and hemodynamic processes, has prevented the development of tools to accurately predict and diagnose heart failure at early stages when corrective measures are most effective. The flow patterns inside the human LV are complex. Special attention should be taken to a large vortex ring that develops during early diastole and causes the blood inside the LV to swirl constantly until it is ejected towards the aorta. The LV vortex ring contributes to an efficient channeling of the blood transit coming from the mitral valve (6) and facilitates that the blood mass coming into the LV during one beat is washed out completely after a few beats (7), which prevents intraventricular blood stagnation.

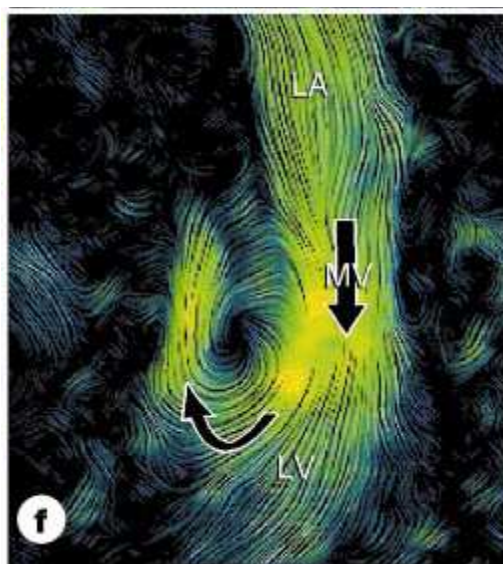


**Figure 1.1 Vortex ring formation. Streamlines pass from the left atrium through the open mitral valve to the left ventricle, with asymmetric recirculation (curved arrow) round the anterior leaflet of the mitral valve. (8)**

The coordination between the timing of the LV vortex and the timing of the electromechanical events of the heart is an important factor that may influence the efficiency of blood flow transport through the LV (9). The LV vortex can only contribute to channeling blood transit towards the aorta if it is synchronized with myocardial relaxation and contraction. Time evolution of the LV vortex is influenced by both its intrinsic fluid dynamics(10), and interactions with the myocardium and valves through pressure forces(11). The overarching of this research is to understand the dependence of the time evolution of the LV vortex on the duration of the LV filling phases, and to determine how this dependence affects blood flow transport in the LV and global ventricular function.

The outcome of this project could have a great impact in **cardiac resynchronization therapy (CRT)** by providing a tool to establish an individualized and optimized programming of biventricular pacers.

CRT has shown to reduce the mortality and morbidity and improve LV function in patients with HV and LV systolic dysfunction (12-15). However, up to 35-40% of patients undergoing CRT do not respond favorably. The reasons for this are not completely known but may include inadequate criteria for patient selection and

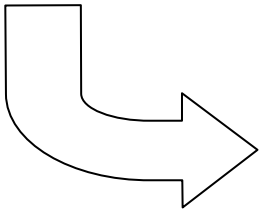
suboptimal programming of the device after implantation and during follow-up (16-18). Achieving a favorable outcome from CRT may be dependent on proper atrioventricular (AV) and intraventricular (VV) delays programming, which enable the LV contraction to take place under the most appropriate preload conditions. Optimization of the AV and VV delays has been shown to produce improvements in cardiac output and it appears necessary in up to 55% of patients undergoing CRT during follow up (19-21). A better understanding of how blood is transported within the LV may help in the development of an efficient method for optimization and may increase the range of patients who can benefit from it.

## 1.2 Approach

This work is part of an interdisciplinary project that combines experimental and clinical studies in animal models and human volunteers with numerical simulation tools.

The clinical side of this project is being carried out in the Non-invasive Cardiology Unit at the Hospital Gregorio Marañón in Madrid (Drs. Javier Bermejo and Raquel Yotti). It involves the development and validation of a novel noninvasive modality to display time-resolved flow maps in the LV (Aim1), and the application of this modality to a group of patients undergoing CRT in order to evaluate the effect of biventricular pacing on the dynamics of LV vortices and blood transport in the LV, and on echocardiographic indices of global LV function.

The specific task addressed by the present work is the development of a numerical code which allows for simulating the filling flow in the left ventricle.

<b>Overarching:</b> Understand the dependence of the time evolution of the LV vortex on the duration of the LV filling phases, and to determine how this dependence affects blood flow transport in the LV and global ventricular function		
<b>Aim 1:</b> To develop a novel noninvasive modalities to display time resolved flow maps in LV  	<b>Aim 2:</b> To evaluate the effect of biventricular pacing on the properties of the LV vortex and echocardiographic indices of global LV function in patients undergoing CRT	
	2.a) Obtain conventional echocardiographic image sequences in non-ischemic DCM patients undergoing CTR and analyze them to evaluate the flow parameters for different pacing programmings.	2.b) Numerical simulation to evaluate the effect of the different pacing programmings on the properties of the LV vortex, on blood flow transport in the LV and on echocardiographic indices of global function.

## 1.3 Objectives

The main objective of this work is to develop a numerical code to simulate the filling process of the left ventricle. This code is intended to provide a tool to understand better the changes in ventricular hemodynamic after the implantation of biventricular pacers in patients undergoing CRT.

In computational fluid dynamics, the primary issues are accuracy, computational efficiency, and, particularly in our case, the handling of complex geometry and moving boundaries. The immersed boundary method allows for dealing with such geometry in Cartesian structured grid, thereby requiring significantly less computational time than competing methods without sacrificing accuracy. Keeping always on mind the presence of immersed boundaries, this work implements a numerical approach to the problem using FORTRAN95. The specific tasks that were performed in the present thesis were:

- To develop a 2D flow solver based on finite differences in a standard geometry (cavity) for validation purposes.
- To design a computationally efficient method to solve the linear system of equations resulting from the spatiotemporal discretization.
- Development of an interpolation technique to impose the required conditions on the immersed boundaries in fixed geometries.
- To develop an efficient time integration procedure consisting of a fractional-step method in combination a low-storage semi-implicit Runge-Kutta method, and to optimize this technique for immersed boundaries.
- To validate the code performance under certain conditions. Some examples will be presented to show the capabilities and limitations of the developed model.

In order to achieve the final aim of simulating numerically the filling process of the left ventricle of the heart, future work should address the following tasks:

- To refine the immersed boundary method for moving geometries.
- To extend the implementation to three dimensions for axisymmetric geometries.
- To develop a Multigrid Method to solve the system of equations.
- To parallelize the code to allow for multi-processor simulations.

Further details about future directions will be presented in section 6.2 at the end of the project.

## 1.4 Content

This work is divided in six chapters, going from general knowledge about cardiology to the particularities and numerical specifications of our problem.

The first chapter presents a general description and motivation of the project. A brief introduction shows the importance of the problem to deal with and its practical application. The general approach to face the problem is presented, and the particular aim of this project is placed in this general approach. Last but not least, the particular objectives to be reached are defined.



Chapter 2 presents a qualitative description of the cardiovascular system. Basic features of the heart, blood and vessels need to be known in order to understand the problem. The heart requires special attention from its mechanical and electrical point of view because it is a key aspect on the global understanding of the problem.

Chapter 3 focuses its attention in the diastole, period of the cardiac cycle that corresponds with the ventricular filling. The relevance of diastole and its relation with heart failure is pointed out. As in a high percentage of the heart failure patients the problem arises from an inappropriate synchronization of the two ventricles that compose the heart, the attention is concentrated in cardiac resynchronization therapy. It is also important to understand the hemodynamic of left ventricle filling and to know the available techniques that are commonly used for describing the filling process of the left ventricle.

Chapter 4 is the first step to develop a numerical model able to simulate the blood flow transport in the left ventricle. A set of simplifications are carry out and justified to define the fluid dynamic model. As result, the domain and boundary conditions are specified.

Chapter 5 is the core of the project and works on the development of the numerical model. The problem, reduced to a set of differential equations, is discretized and solved on a staggered grid following a fractional-step method in combination a low-storage semi-implicit Runge-Kutta method. A computationally efficient method to solve the linear system of equations is designed and compared with other methods. Finally, the code is validated analyzing its solution under different conditions. First, we study a cavity flow in a square domain where the upper boundary is moving on the horizontal direction. The second case compares the analytical solution of a well-known problem with the one provided by our numerical model. Last case studies the response of the code to the existence of immersed boundaries.

In the last chapter, Chapter 6, the obtained conclusions are summarized and future researching lines are proposed.



# Chapter 2

---

## 2 The cardiovascular system

The development of a numerical model to describe the filling process of the left ventricle of the heart cannot be performed without understanding the basic features of the cardiovascular system. That is why this chapter presents a qualitative description of the circulatory system and its three functional parts: the heart, the blood and the vessels. As we are interested in the filling of the ventricle, we will focus on the heart, the responsible of pumping the blood through the system. Afterwards, we will briefly describe blood and vessels.

### 2.1 Circulation

The circulation is an evolutionary consequence of body size. In large organisms, diffusion is not adequate to supply nutrients to centrally located cells, nor to eliminate waste products. The primary role of the circulatory system is the distribution of dissolved gases and other molecules for nutrition, growth, and repair. Secondary roles have also evolved:

- Fast chemical signaling to cells by means of circulating hormones or neurotransmitters.
- Dissipating heat by delivering heat from the core to the surface of the body.
- Mediating inflammatory and host defense response against invading microorganisms.

The circulatory system of humans integrates three basic functional parts:

- The heart (pump)
- The blood (circulated liquid)
- The vessels (set of containers)

### 2.1.1 Circulation cycle

The circulation forms a closed loop, so the description can begin anywhere (see Figure 2.1). Beginning in the left side, the left heart receives blood that is rich in  $O_2$  and pumps this blood into the systemic arteries. These form a tree of progressively smaller vessels that supply fully oxygenated blood to all of the organs and tissues of the body. From the smallest of the systemic arteries blood flows into the systemic capillaries, which are roughly the diameter of a single red blood cell. It is in the capillaries that the actual exchange of  $O_2$  and  $CO_2$  takes place. The blood that leaves the systemic capillaries carries less  $O_2$  and more  $CO_2$  than the blood that entered them.

Leaving the systemic capillaries, the blood enters the systemic veins, through which it flows in vessels of progressively increasing size toward the right side of the heart.

The right heart pumps blood into the pulmonary arteries, which form a tree that distributes the blood to the tissues of the lung. The smallest branches of this tree give rise to the pulmonary capillaries, where  $CO_2$  leaves the blood stream and  $O_2$  enters from the air space of the lungs. Leaving the pulmonary capillaries, the oxygenated blood is collected in the pulmonary veins, through which it flows back to the left heart. This completes the circulation. The average time required for a red blood cell to complete the circuit is about 1 minute.

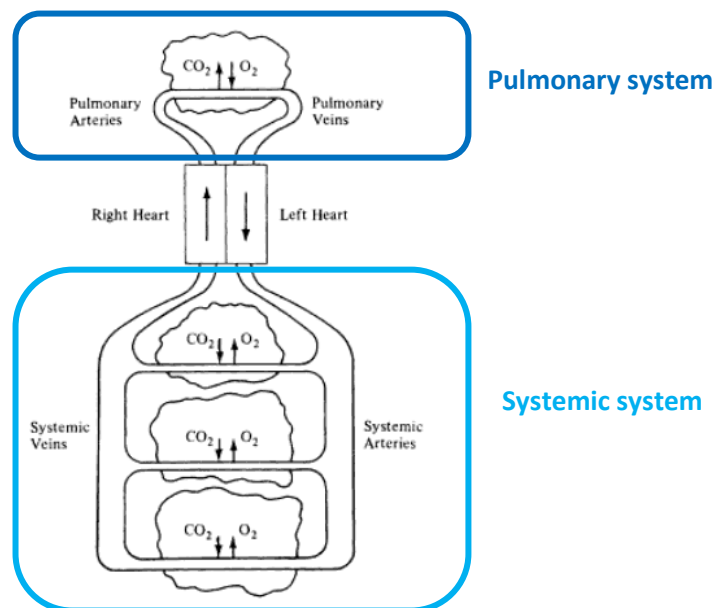


Figure 2.1. Plan of the circulation (22)

It is important to point out that the flow resistance in the pulmonary system is much lower than in the systemic circulation. The systemic manometric pressure is about six times the pulmonary pressure and the systemic blood volume is ten times the pulmonary blood volume. Further details are presented in Table 2.1.

Table 2.1. Normal Resting Pressures and Volumes of the Systemic and Pulmonary Arteries and Veins (23)

	P (mmHg)	V(liters)
Systemic arteries (sa)	100	1.0
Systemic veins (sv)	2	3.5
Pulmonary arteries (pa)	15	0.1
Pulmonary veins (pv)	5	0.4

There are many factors which affect the circulation system. One example is aging, which causes stiffening of the arterial system with an increase in systolic arterial pressure. This sometimes leads to myocardial hypertrophy and prolonged relaxation (24). Exercise is other factor that has a great impact over the circulation cycle. During exercise, the demand of oxygen increases. This increased need of oxygen is reached thanks to a higher heart rate, an increased stroke volume and a higher extraction of oxygen from blood. Typical values are listed in Table 2.2.

Table 2.2 Typical circulation parameters in normal conditions and with exercise (23)

	Normal conditions	With exercise
Stroke volume ( $V_{\text{stroke}}$ )	0.07 l/beat	0.1 l/beat
Heart rate (F)	80 beats/min	200 beats/min
Cardiac output (Q)	5.6 l/min	20-25 l/min

## 2.2 The heart

### 2.2.1 Introduction

The heart is the prime mover of blood. It contracts periodically and pumps blood throughout the body in two phases. In the first phase, diastole, the heart relaxes and fills with blood. In the second phase, systole, it contracts and pumps blood out as shown in Figure 2.2.

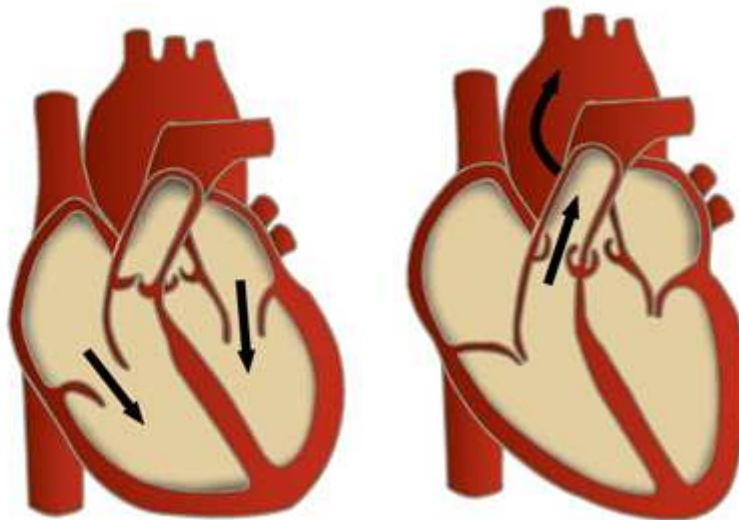


Figure 2.2. Heart filling (diastole, left) and heart pumping (systole, right) (25)

In each cycle, the left and right ventricles are first filled with blood from the left and right atria, respectively. Both atria operate more as passive reservoirs than as mechanical pumps. However, they do contract, and this contraction does enhance ventricular filling and cardiac output to a small degree. Then by the deceleration of the blood stream a pressure field is generated, which closes the valves between the atria and the ventricles (mitral valve for left side and tricuspid valve for the right). The contraction of the heart muscle begins and the pressures in the ventricles rise. When the pressure in the left ventricle exceeds that in the aorta, and the pressure in the right ventricle exceeds that in the pulmonary artery, the aortic valve in the left ventricle and the pulmonary valve in the right ventricle are pushed open, and blood is ejected into the aorta

and the lung. This is the systolic phase. The ejection continues until the deceleration of the jets of blood leads the pressure to close the valves. Then the muscle relaxes. The pressures decrease, and the diastolic phase begins (26). Figure 2.3 shows the heart components mentioned above.

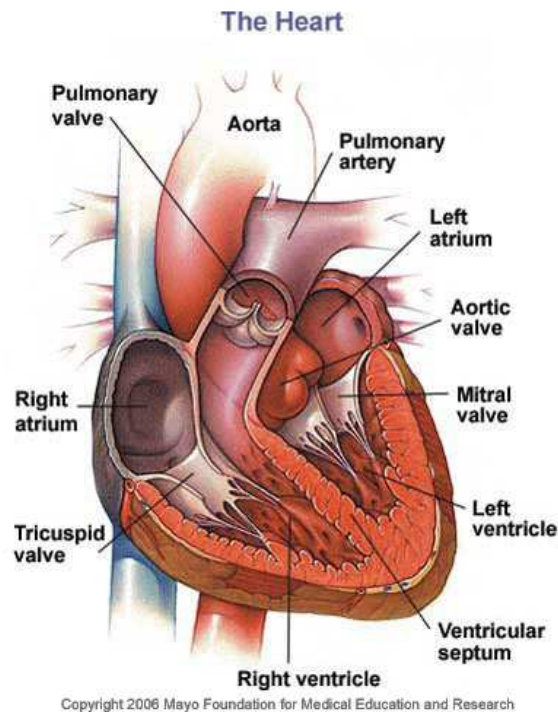
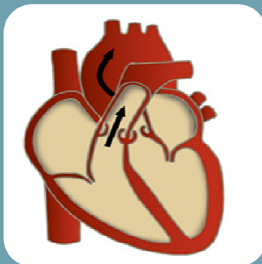


Figure 2.3. Heart components. (25)

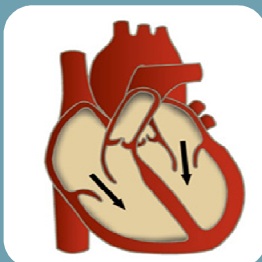
### 2.2.2 Cardiac cycle

The following table presents the different phases that can be identified in the cardiac cycle.



#### Systole

- **Isovolumic contraction:** the ventricular chamber is developing sufficient pressure to exceed the pressure in the artery and thereby open the interposing valve (pulmonary or aortic)
- **Ejection:** blood is being actively expelled from the ventricular chamber.



#### Diastole

- **Isovolumic relaxation:** the chamber pressure is rapidly declining until it falls below atrial pressure and thereby opens the interposing valve (tricuspid or mitral).
- **Passive filling (rapid filling phase):** blood moves from the atrium to the ventricle thus dissipating any pressure gradient.
- **Diastasis (slow filling phase):** there is little movement of blood as the pressures in the atrium and ventricle matched.
- **Atrial contraction:** the atrium undergoes active contraction and develops increased pressure thus re-establishing a pressure gradient between the atrium and ventricle and causing a second burst of ventricular filling.

Thus, during the cardiac cycle pressures and ventricular volumes are changing. Figure 2.4 presents the evolution of pressures and volumes in the left ventricle.

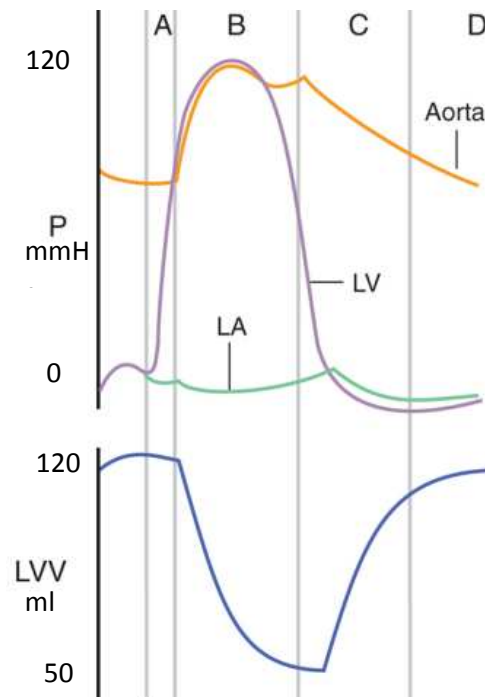


Figure 2.4. Time sequence of events during a single cardiac cycle. Pressures (P) in the aorta, left ventricle (LV), and left atrium (LA). Isovolumic contraction (A), ejection (B), isovolumic relaxation (C) and filling (D). LVV=left ventricle volume. (27)

The heart is a system of two pumps linked in series. The muscular wall of the left ventricle is thicker and more powerful than that of the right ventricle. The interventricular septum welding the two pumps together is even thicker. The thick muscular walls of the ventricles are mainly responsible for exerting the pumping function of the heart.

The mechanism **right ventricular emptying** involves three motions (Figure 2.5):

1. The longitudinal axis of the right ventricle shortens when spiral muscles pull the tricuspid valve ring toward the apex.
2. The free wall of the right ventricle moves toward the septum in a bellows-like motion.
3. The contraction of the deep circular fibers of the left ventricle forces the septum into a convex shape, so that the septum bulges into the right ventricle. This bulging of the septum stretches the free wall of the right ventricles over the septum.

These three motions are well suited for ejecting a large volume, but not for developing a high pressure. The right ventricle ejects the same blood volume as the left ventricle, but it does so at much lower intraventricular pressure.

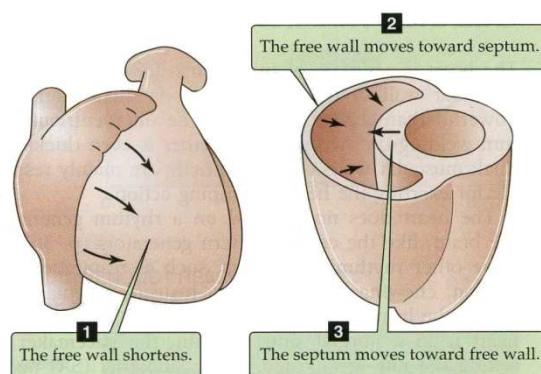


Figure 2.5. Right ventricle contraction.

The mechanical action for the **left ventricle** occurs by a dual motion (Figure 2.6)

1. Constriction of the circular muscle layers reduces the diameter of the chamber, progressing from the apex to the base (akin to squeezing a tub of toothpaste)
2. Contraction of the spiral muscles pulls the mitral valve ring toward the apex, thereby shortening the long axis.

The first mechanism is the more powerful and is responsible for the high pressures reached in the left ventricle. The conical shape of the lumen gives the left ventricle a smaller surface to volume ratio than the right ventricle and contributes to the ability of the left ventricle to generate high pressures.

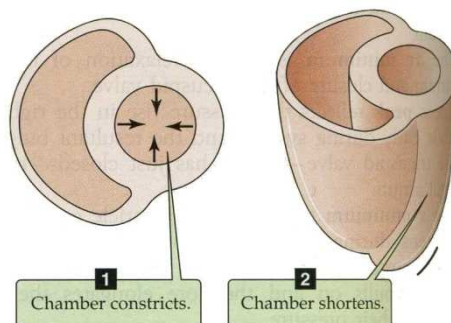


Figure 2.6. Left ventricle contraction

**Atrial** contraction normally makes only a minor contribution to the filling of the two ventricles (about 10% of left ventricular filling) when the subject is at rest because most of ventricular filling occurs prior to atrial contraction as blood passively flows from the pulmonary veins, into the left atrium, then into the left ventricle through the open mitral valve. At high heart rates, however, the atrial contraction may account for up to 40% of ventricular filling. The contraction of the atria is a useful safety factor in at least two circumstances. During tachycardia, when the diastolic interval (and thus the interval for passive filling) is short, the atrial contraction can provide a much needed boost. Atrial contraction also contributes to ventricular filling in certain pathologic conditions.

Events on the right and the left sides do not occur simultaneously. Cardiac rhythm results from electrical impulses that begin in the **sinoatrial (SA)** node. As the SA node is located in the right atrium, atrial contractions occur earlier in the right atrium than in the left. Ventricular contraction starts slightly earlier



on the left atrium, and the mitral valve closes before the tricuspid valve does. The right ventricle has shorter period of isovolumetric contraction because it does not need to build up as much pressure to open its outflow valve and initiate ejection. Thus, the pulmonary valve opens slightly ahead of the aortic valve. Ejection from the right ventricle lasts longer than that from the left. Isovolumetric relaxation is briefer in the right heart than in the left.

### 2.2.2.1 Pressure - Volume cycle

Representing the pressure and volume of the left ventricle throughout a cardiac cycle the different phases of the cardiac cycle can be clearly observed.

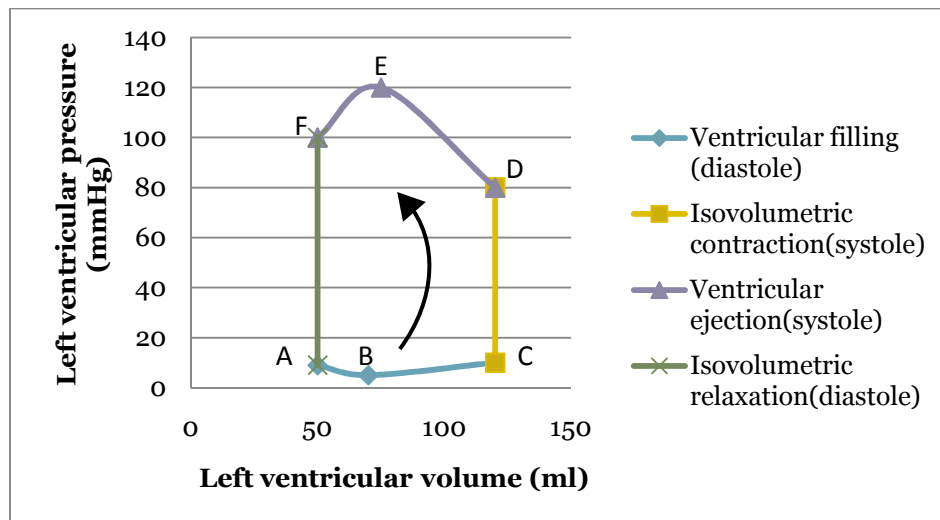


Figure 2.7. Pressure - volume cycle.

#### 2.2.2.1.1 Ventricular filling (ABC)

Point A represents the instant at which the mitral valve opens. As the mitral valve opens, the ventricle begins to fill passively because atrial pressure is higher than ventricular pressure. Despite the rapid entry of blood ventricular pressure falls during the interval AB because the ventricular muscle is continuing to relax. During the segment BC the LV volume is doubled with a modest rise in pressure due to the high compliance of the ventricular wall during the late diastole.

#### 2.2.2.1.2 Isovolumetric contraction (CD)

Point C represents the closure of the mitral valve. The pressure increases at constant volume to a value about equal to the aortic end-diastolic pressure.

#### 2.2.2.1.3 Ventricular ejection (DEF)

Point D represents the opening of the aortic valve, so the ventricle can now begin to shorter and eject blood. Contraction continues during the interval DE increasing the pressure. E represents the instant at which the ventricular muscle starts to relax, decreasing the pressure. Point F represents end-diastolic volume and pressure.

#### 2.2.2.1.4 Isovolumetric relaxation (FA)

Point F represents the closing of the aortic valve. Ejection has ended and the ventricular pressure falls due to the relaxation. At the end of the isovolumetric relaxation, the mitral valve opens and the cardiac cycle starts all over again with the ventricular filling.

### 2.2.2.2 Cardiac muscle

Cardiac muscle makes up the wall of the heart. It is comprised by cells that are called cardiomyocytes. The cardiomyocytes are made up of myofibrils. A sarcomere is the basic unit of a muscle myofibril. Myocytes are joined to one another via intercalated disks that allow communication between the cells such that there is a sequential contraction of the cells from the bottom of the ventricle to the top. This makes possible the maximal ejection of blood from the ventricle during contraction. The functional properties of cardiac muscle (how much tension it can develop, how rapidly it can contract) depend on many factors, but especially on two properties intrinsic to the cardiac myocyte:

1. Initial sarcomere length (a convenient index is the end-diastolic volume).
2. Force that the contraction myocytes must overcome (a convenient index is the arterial pressure that opposes the outflow of blood from the ventricle).

### 2.2.2.3 Factors affecting the performance of the heart

The performance of the heart depends on such factors as the degree of filling (preload), arterial pressure (after-load) and heart rate. Contractility provides an intrinsic measure of heart performance independent of these extrinsic factors. The contractility is the slope of the end-systolic pressure relation. Effects of these parameters on the cardiac cycle are summarized on Table 2.3.

Table 2.3 Factors affecting the heart performance

Factor	Related with...	Change in...	Effect
<b>Contractility</b>	Intrinsic measure	End systolic pressure-volume relation	Stroke volume increases increasing contractility
<b>Preload</b>	Initial sarcomere length	Degree of filling or end of diastolic pressure	Stroke volume increases increasing preload
<b>After-load</b>	Aortic pressure	Arterial pressure	Stroke volume and ejection fraction decrease when increasing after-load

### 2.2.3 Electric system

Every contraction of the heart muscle needs an electric stimulation, so the heart must have a center that generates a periodic electrical signal which is conducted to every muscle cell.

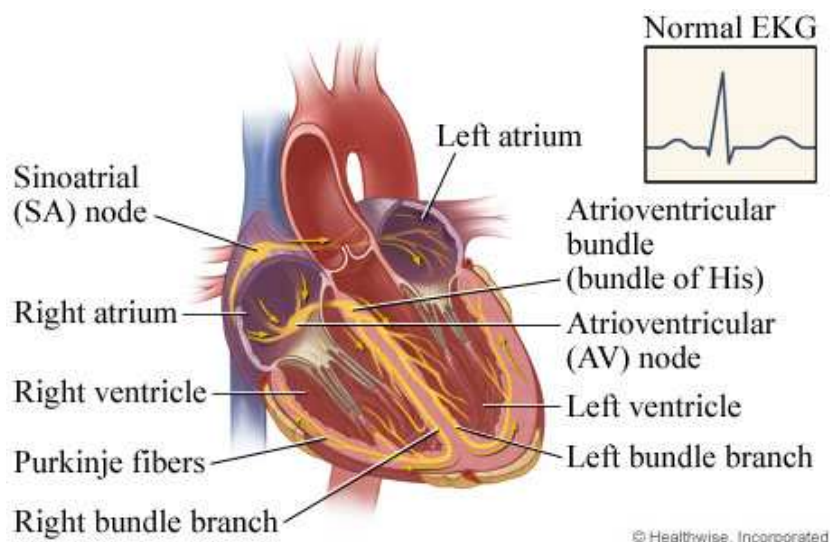


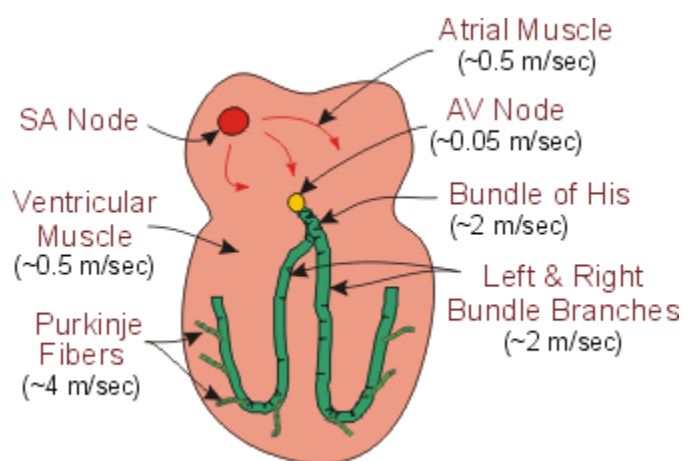
Figure 2.8. Electrical heart system (28)

Normal cardiac rhythm results from electrical impulses that begin in a special group of cells that form the sinoatrial node (SA) (Figure 2.8), also called the sinus node. Located in the right atrium of the heart, the sinoatrial node cells act as the heart's natural pacemaker, being the main electric generating station of the heart. The term pacemaker activity refers to the spontaneous time-dependent depolarization of the cell membrane that leads to an action potential. Any cardiac cell with pacemaker activity can initiate a heartbeat. The pacemaker with the highest frequency will be the one to trigger an action potential that will propagate throughout the heart.

From the SA node, the cardiac electric signal spreads radially throughout the right atrium along ordinary myocardial fibers at a conduction velocity of approximately 1 m/s. In the meantime, a special bundle of fibers carries the signal directly from the SA node to the left atrium and three other bundles conducts the signal directly from the SA node to the left atrioventricular node (AV). The AV node is a substation of the signal transmission. Because the intrinsic pacemaker rate of the AV node is slower (around 40 beats/min) than that of the SA node (60 beats/min), it does not set the heart rate. Its pacemaker activity is considered secondary, but if the SA node fails, the AV node can assume control of the heart and drive it successfully.

When the signal from SA node reaches AV node, it is delayed for a certain period of time that is essentially for allowing the ventricles to finish filling with blood before contraction and ejection occur. From the AV node, the impulses travel through a system of specialized heart tissue, the bundle of His. Located in the wall that separates the two ventricles, this conducting system splits to form the right and left bundle branches that travel to the respective ventricles. Via this conducting pathway, powerful electrical jump-start signals are delivered to the ventricular muscle of the heart. In the healthy heart, these impulses travel at the same speed so that the two ventricles contract at the same time and oxygen-rich blood from the lungs is pumped throughout the body. Left and right bundle branches divide into further branches called Purkinje fibers, spread over both ventricles. Electric signal propagates fast in the Purkinje fibers at speed of 1 to 4 m/s. Purkinje fibers have the slowest intrinsic pacemaker rate (20 beats/min or less), thus, these fibers are very unreliable as pacemakers.

The last stage of electric transmission is done by the cardiac muscle itself thanks to the semblance of syncytium between cardiac muscle cells, transmitting the signal from one cell to the other. The speed of signal transmission in the myocardium is 0.3 to 0.4 m/s. As summary, Figure 2.9 presents the different tissues involved in the generation and transmission of the electric signal.



TISSUE	CONDUCTION VELOCITY (m/s)	PACEMAKER RATE (beats/min)
SA node	0.05	60
Atrial pathways	1	--
AV node	0.05	40
Bundle of His	1	--
Purkinje system	4	20
Ventricular muscle	0.5	--

Figure 2.9. Conduction velocity and pacemaker rate in different cardiac tissues. (23)

The conduction system within the heart is very important because it permits a rapid and organized depolarization of ventricular myocytes that is necessary for the efficient generation of pressure during systole. The time (in seconds) to activate the different regions of the heart are shown in Figure 2.10. Atrial activation is complete within about 0.09 sec following SA nodal firing. After a delay at the AV node, the septum becomes activated. All the ventricular mass is activated by about 0.23 seconds.

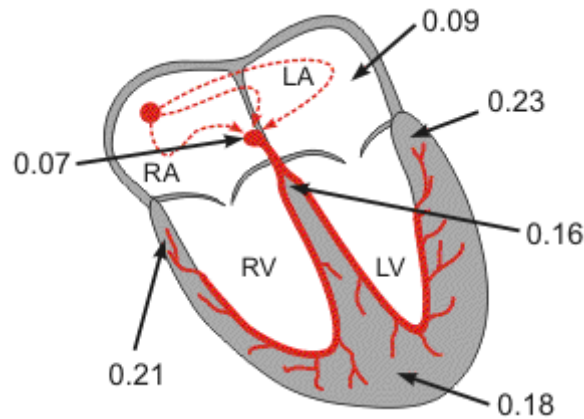


Figure 2.10. Cardiac activation times (seconds) (29)

### 2.2.3.1 Electrocardiogram

The electrocardiogram (ECG or EKG) is the standard clinical tool used to measure the electrical activity of the heart. A typical ECG tracing of the cardiac cycle (heartbeat), as the one presented on Figure 2.11, consists of a set of waves, segments and intervals described in Table 2.4.

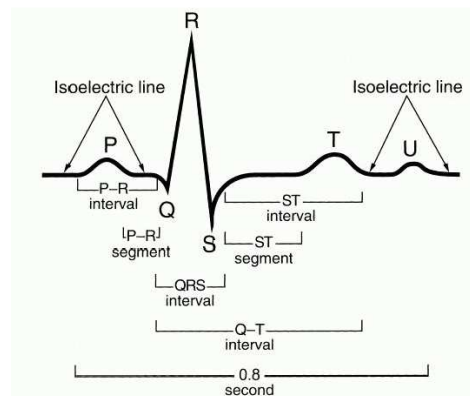


Figure 2.11. Electrocardiogram. (26)

Table 2.4. Electrocardiogram components description

<b>Waves</b>	<b>P wave</b>	Reflects spreading from the right atrium to the left atrium of the main electrical vector during normal atrial depolarization.	80ms
	<b>QRS complex</b>	Reflects the rapid depolarization of the right and left ventricles. They have a large muscle mass compared to the atria and so the QRS complex usually has much larger amplitude than the P-wave.	80 to 120ms
	<b>T wave</b>	Represents the repolarization (or recovery) of the ventricles.	160ms
	<b>U wave</b>	It is normally visible in 50 to 75% of ECGs. It is typically low amplitude, and, by definition, follows the T wave. It represents the repolarization of the papillary muscle.	

<b>Intervals</b>	<b>RR interval</b>	The interval between an R wave and the next R wave is the inverse of the heart rate. Normal resting heart rate is between 50 and 100 beats/min	0.6 to 1.2s
	<b>PR interval</b>	It is measured from the beginning of the P wave to the beginning of the QRS complex. It starts at the beginning of the atrial contraction and ends at the beginning of the ventricular contraction. Reflects the time the electrical impulse takes to travel from the sinus node through the AV node and entering the ventricles. The PR interval is therefore a good estimate of AV node function.	120 to 200ms
	<b>QT interval</b>	It is measured from the beginning of the QRS complex to the end of the T wave. A prolonged QT interval is a risk factor for ventricular tachyarrhythmias and sudden death. The QT interval indicates how fast the ventricles are repolarized, becoming ready for a new cycle.	300 to 430ms
	<b>ST interval</b>	It is measured from the end of the QRS complex to the end of the T wave.	320ms
	<b>QRS interval</b>	It indicates how fast the ventricles depolarize.	<110 ms
<b>Segments</b>	<b>PR segment</b>	Connects the P wave and the QRS complex. This coincides with the electrical conduction from the AV node to the bundle of His to the bundle branches and then to the Purkinje Fibers. This electrical activity does not produce a contraction directly and is merely traveling down towards the ventricles and this shows up flat on the ECG.	50 to 120ms
	<b>ST segment</b>	It connects the QRS complex and the T wave. Represents the period when the ventricles are depolarized.	80 to 120ms

The electrical described before are associated with contraction of the ventricles as Figure 2.12 shows.

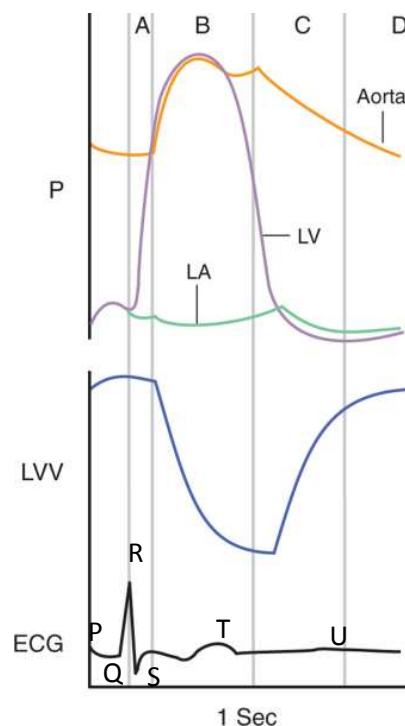


Figure 2.12. Time sequence of events during a single cardiac cycle (27)

When the natural electric system of the heart is not able to develop the pacing activity, the ventricular function has to be restored by applying artificial electrical impulses. Cardiac resynchronization therapy (CRT), a technology that simultaneously paces both the left and right ventricles, has emerged as an important treatment tool for heart failure patients with reduced LV function and ventricular dyssynchrony (uncoordinated beating of the ventricles). CRT requires a proper programming of the atrioventricular (AV delay) and intraventricular delay (VV delay). The AV delay is the time between the atrial beat and the corresponding ventricular paced event, this is, the P-R interval. VV timing refers to the synchronization of RV and LV contractions. It measured from electrical delay between tip of RV lead and LV lead during intrinsic conduction. Further details will be given in section 3.5.

#### **2.2.4 Heart valves**

The human heart has four valves: the tricuspid (T), pulmonic (P), aortic (AO) and mitral (M). They lie essentially in a plane. AO (ejection) and M (filling) valves are going to be analyzed in detail because they are the ones that control the ejection and filling of blood in the left ventricle.

##### **2.2.4.1 Mitral valve**

The mitral valve consists of two thin membranous cusps of roughly trapezoidal shape that originate from the slightly elliptical mitral ring. In the open structure these membranes form a scalloped, cone-like structure. The M valve regulates the entrance of blood in the left ventricle.

When operating, the membranes are pushed open at a stage of diastole when the pressure in the left atrium exceeds that of the left ventricle. Then, a jet of blood rushes in from the left atrium into the left ventricle, impinges on the ventricular wall, and is redirected towards the aortic valve in the LC vortex ring. Thus, the blood stream is decelerated in its path and a positive pressure gradient is created. Towards the end of diastole, the pressure acting on the ventricular side of the mitral valve membranes becomes higher than that acting on the side of the membranes facing the left atrium. The net force acts to close the valve. In a normal heart, closure occurs without any backward flow or regurgitation. The papillary muscles play no role at all in opening and closing the valve.

##### **2.2.4.2 Aortic Valve**

The aortic valve consists of three thin, crescent-shaped cusps, which in the open position are displaced outward and toward the aorta. In the closed position the three cusps come together to seal the aortic orifice. The pulmonary valve has a similar structure. The AO valve regulates the exit of blood from the left ventricle.

The operation of the AO valve can be modeled with the sinus of Valsalva as it is shown in Figure 2.13 (Bellhouse and Bellhouse 1969,1972). The flow issuing from the ventricle immediately upon opening of the valve at the inception of systole is split into two streams at each valve cusp. Part of the flow is directed into the sinus behind the valve cusp, where it forms a vertical flow before re-emerging, out of the plane of the figure, to rejoin the main stream in the ascending aorta.

When the aortic pressure rises sufficiently so that deceleration of the flow occurs, and adverse pressure gradient is produced. The higher pressure causes a greater flow into the sinus, which carries the cusp toward apposition. The peak deceleration occurs just before the valve closure. The vertical motion established earlier upon the opening of the valve has the merit of preventing the valve cusp from bulging outward to

contact the walls of the sinuses. The open sinus chamber thus can be supplied with fluid to fill the increasing volume behind the valve cusps as they move towards closure.

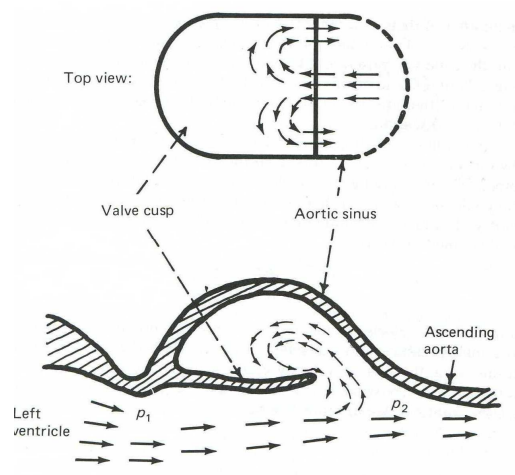


Figure 2.13. Flow pattern within the sinus of Valsalva (26)

## 2.3 Blood

Blood is a complex fluid (its main components are presented in Figure 2.14) whose properties are significantly affected by the arrangement, orientation and deformability of red blood cells. In practice, the effective characteristics of the blood depend on several physiologic factors such as fibrinogen concentration, hematocrit (proportion of blood volume that is occupied by red blood cells), vessel radius, linear velocity and temperature.

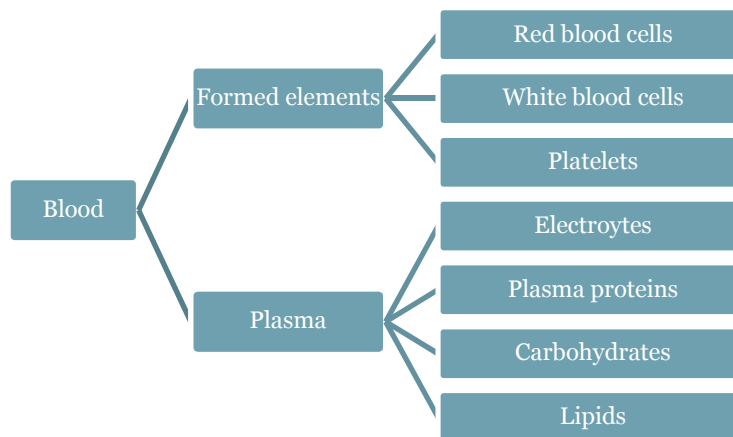


Figure 2.14. Blood composition

The most common method of determining the consistency of a flowing liquid uses the relation between shear stress and time rate of shear strain (or shear rate). If the flow is constant in time, then the ratio of shear stress to shear rate is the viscosity. When flows are changing with time, such as blood flow in some parts of the human circulation, the liquid generally demonstrates both a viscous and an elastic effect, both of which determine the stress-to-strain rate relationship. The parameters that describe the flow properties of complex fluids like blood are the viscosity and the elasticity. The viscosity is related to the energy



dissipated during flow primarily due to sliding and deformation of red blood cells and red blood cell aggregates. The elasticity is related to the energy stored during flow due to orientation and deformation of red blood cells.

Blood viscosity and elasticity depend on the rate of flow or shear rate. The changes in viscosity and elasticity are a result of changes in the arrangement, orientation and stretching of the red blood cells. The viscoelastic profile of normal human blood can be divided into three regions: a region of low shear rates, **Region 1**, where normal red blood cells will aggregate in a space efficient manner. The cells are in large aggregates and as the shear rate increases, the size of the aggregates diminish. A region of mid-shear rates, **Region 2**, where the internal stress due to pressure is sufficient to separate aggregated cells causing breakage of aggregates. Increasing shear rate causes the cells to orient in the direction of flow. And a region of high shear rates, **Region 3**, where the increasing shear rate causes normal red blood cells to stretch or deform and align with the flow.

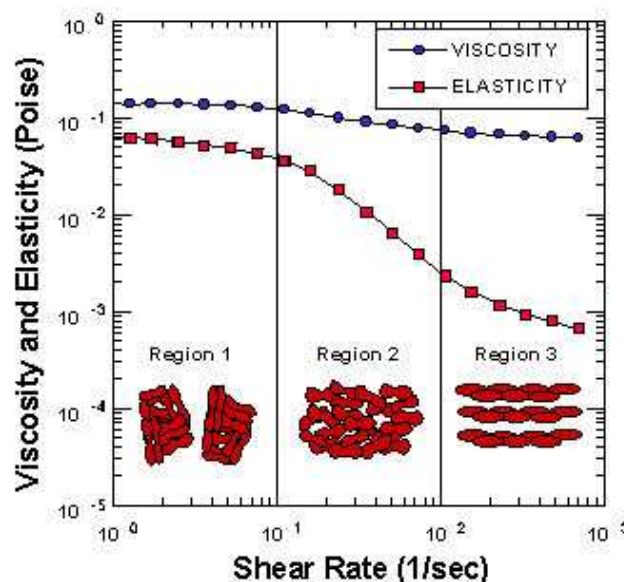


Figure 2.15. Human blood viscosity and elasticity (30)

In the mayor vessels, including the heart, blood behaves as shown in Region 3, so it is approximately a Newtonian fluid with constant viscosity and no elasticity.

## 2.4 Vessels

The vascular system is not a system of rigid tubes. Moreover, the anatomy and functions of the various segments of the vasculature differ greatly from one to another. Three groups can be distinguished:

- Arteries (distribution system)
- Microcirculation through capillaries (diffusion and filtration system)
- Veins (collection system)



### 2.4.1 Vessels flow description

If blood vessels were rigid tubes, so that the resistance ( $R$ ) were constant, and if the driving pressure were also constant throughout the cardiac cycle, we could describe the blood flow ( $F$ ) using a simple Ohm's law-like relationship.

$$\Delta p = R \cdot F$$

However, because blood vessels are compliant (so that  $R$  varies with pressure) and because both aortic pressure and flow vary during the cardiac cycle, arteries cannot be described in this way. As a result, the ratio  $\Delta p/F$  is not longer a resistance, but a complex quantity called the mechanical impedance that depends on the classical resistance, as well as the compliance and the inertial properties. Because of these properties, pressure and flow waves are not the same in different vessels.

The cardiac cycle causes pressure waves in the aorta and peripheral vessels. The mean arterial pressure falls very slightly increasing distance from the heart although the peak pressure increases and an important secondary pressure oscillation appears during diastole. Thus, although the pressure waves are distorted, they are not damped.

In terminal arteries and arterioles, damping predominates over distortion. The damping is produced due to:

- As there are many parallel vessels with a large aggregate wall area, the aggregate compliance increases, damping the pressure wave.
- The smaller arteries have a smaller radius and thus a far greater resistance, which means arterial pressure must fall in proportion to the much higher resistance.

By the time the blood reaches the capillaries, the damping is so severe that pulsations do not normally occur. Nevertheless, blood flow in systemic capillaries can exhibit slow oscillations, unrelated to the cardiac cycle. Pulmonary capillaries are an exception because upstream vessels are short and they have low resistance and high compliance.

Systemic veins also have pressure waves originated through three mechanisms:

- Retrograde action of the heartbeat during the cardiac cycle, synchronized to the cardiac cycle.
- The respiratory cycle. During inspiration, the diaphragm descends, causing intrathoracic pressure to decrease and intra-abdominal pressure to increase. Consequently, the venous return from the head and upper extremities transiently increases, as low-pressure vessels literally suck blood into the thoracic cavity. Simultaneously, the venous flow decreases from the lower extremities because of the relatively high pressure of the abdominal veins during inspiration. Therefore, during inspiration, pressure in the jugular vein falls while pressure in the femoral vein rises.
- The contraction of skeletal muscles.



# Chapter 3

---

## 3 Diastology

Diastolic Heart Failure is recognized as a major health problem. Only with an increased knowledge and understanding of the pathophysiology of diastolic function and diastolic heart failure (DHF) can effective management strategies be developed. This knowledge can be applied to patients with DHF to decrease mortality and morbidity of this important cause of heart failure. In order to achieve this purpose, this chapter focuses on the hemodynamics of LV filling and its relation to diastolic function. We will then proceed to describe how artificial stimuli can help to restore the ventricular function when the normal pacemaker is unreliable. In approximately 30% of patients with heart failure, the two ventricles beat slightly out of phase. That is why the attention is focused in the description of the cardiac resynchronization therapy (CRT) which allows to re-coordinate the beating of the two ventricles by pacing both ventricles simultaneously.

### 3.1 Ventricular diastolic filling and function

#### 3.1.1 Definition of diastole

Cardiac function is critically dependent upon diastolic physiologic mechanisms to provide adequate LV filling (cardiac input) in parallel with LV ejection (cardiac output) both at rest and during exercise. Mechanically, diastole is considered to begin when the pressure within the left ventricle begins to fall—that is, during the **isovolumic relaxation phase**. The left ventricular pressure will continue to fall rapidly, the mitral valve will open when the left ventricular pressure falls below the left atrial pressure. In the normal heart, the active relaxation of the LV wall causes a suction effect after mitral valve opening that causes **rapid early filling**. Left ventricular relaxation will normally end in the first third of filling so that the subsequent filling is dependent

upon the passive tissue properties as well as contributions from ventricular interaction and pericardial restraint. The normal left ventricle is composed of completely relaxed cardiomyocytes and is very compliant and easily distensible, offering minimal resistance to LV filling over a normal volume range. The filling process in this phase is slower and is called **diastasis**. At the end of diastole, **atrial contraction** will restore the full preload of the ventricle before the onset of contraction. Atrial contraction near the end of diastole contributes 20 – 30 % to total LV filling volume and increases diastolic pressures by less than 5 mmHg. As a result, LV filling can be accomplished by very low filling pressures in the left atrium and pulmonary veins, preserving a low pulmonary capillary pressure (< 12mmHg) and a high degree of lung distensibility.

For the practicing physician it is difficult to understand or measure in isolation the contribution of the multiple interrelated components of the cellular and mechanical mechanisms comprising diastole. From a simplistic standpoint, clinical diastole is the process or phase where the heart, as a global operating chamber, relaxes and fills with blood in preparation for the next contraction. The simplified definition of diastole from a clinical point of view is an interrelated sequence of events: relaxation, suction, filling, and atrial contraction.

### 3.1.2 Measurements of diastolic function

Comprehensive assessment of ventricular diastolic function is a complex process. Full elucidation generally requires invasive measurements, such as left ventricular end diastolic pressure, the time constant of isovolumic LV relaxation, the pressure volume relationship of the ventricle at end diastole, and mean left atrial pressure. Such invasive measurements are inappropriate for routine clinical purposes, and thus diastolic function is generally assessed using **Doppler Echocardiography**, largely through the observation of transmitral and pulmonary venous flow, supplemented by myocardial velocity and color M-mode Doppler information.

**Particle Image Velocimetry (PIV)** is other of the methods broadly used for fluid visualization. In this technique, the fluid is seeded with tracer particles which, for the purpose of PIV, are generally assumed to faithfully follow the flow dynamics. It is the motion of these seeding particles that is used to calculate velocity information of the flow being studied. Figure 3.1 shows an example of this technique. In figure A, the Echo freeze frames represent the divergence-free velocity vector on the scan-plane, superimposed to the reconstructed Doppler representation. Figure B shows parametric representations of steady streaming field with superimposed velocity vectors (arrows) and the steady streaming in-plane streamlines along the divergence-free velocity field. C represents the pulsatile strength field with superimposed pulsatile in-plane streamlines.

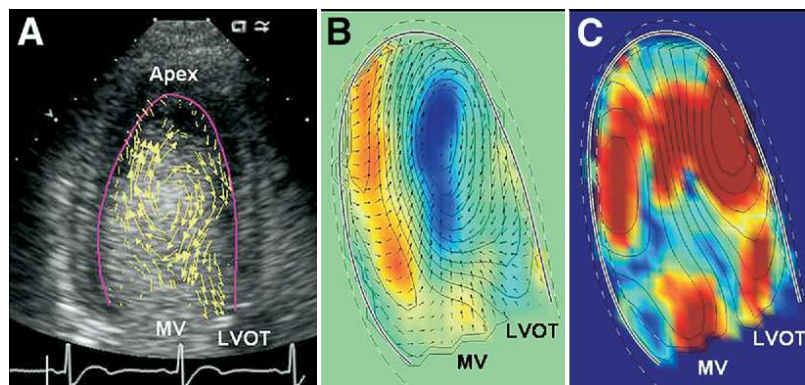


Figure 3.1. Flow data by digital PIV from the apical long axis view. LVOT, left ventricular outflow tract; MV, mitral valve.

Other widely used techniques to measure the diastolic function are **contrast angiographic filling curves** based on frame-by-frame volume calculations or **radionuclide high resolution time activity curves**.

In order for these noninvasive indices to be useful for interfering actual diastolic function of the heart, it is critical to establish a conceptual framework that reflects the physical and physiological determinants of intracardiac blood flow. Clinical experiments in volunteers and patients can be helpful in understanding general trends in the relationships between invasive parameters and noninvasive measurements, but a more comprehensive approach can be potentially obtained with computer simulations that invoke realistic descriptions of chamber and valvular functions and enable to study the effect of different phenomena in a systematic way. The reason for this is that flows of blood through different parts of the circulatory system are interdependent. A change in a single parameter affects flow throughout the system. Section 3.2 will provide a description of this conceptual framework to relate the actual diastolic function of the heart and the indices to modulate its behavior.

## 3.2 Flow propagation inside the ventricle

Since the mid 1980s, researchers have worked to develop models of the heart with increasing complexity, beginning from a very simple isolated model of the mitral valve used to understand the mitral pressure half-time; to models incorporating more realistic diastolic characteristics of the ventricle and atrium; to models that simulated the cardiac chambers and valves, as well as the peripheral and pulmonary vasculature; to most recently a simulation that links knowledge of basis myocyte and fiber function to the gross architecture of the heart.

Three major phenomena develop simultaneously during filling:

1. An intraventricular gradient appears at the beginning of LV filling.
2. The blood column slows after exiting the mitral valve while continuing as laminar flow toward the apex.
3. Finally vortices start appearing due to propagation of the blood column past the tips of the mitral leaflets, while the left ventricle continually changes its size.

During the rapid filling phase (E wave), a jet starts its propagation through the mitral valve into the ventricular chamber. Driven by this jet, a vortex ring is formed around the jet just downstream from the mitral orifice. During filling, the vortex ring travels toward the middle of the expanding ventricle, while a weak vortex is formed within the aortic outflow tract, which dissipates late during diastasis. After the vortex ring reaches the middle of the ventricle, its anterior part becomes stationary, while the posterior part continues forward. During atrial contraction (A wave), a new, weaker vortex ring that encompasses a part of the outflow tract is formed, while the posterior side of the initial vortex ring continues to move into the posterior apical region of the ventricle. At the end of the filling, the posterior part of the second vortex ring merges with the first one, forming a large vortex in the posterior apex. Creation of vortices plays a crucial role in mitral valve closure and in the transfer of blood toward the apex and then into the LV outflow tract.

These vortex can be seen when the heart is imaged by echocardiography with high-frequency transducers, or after the contrast injection, and can be quantified by magnetic resonance and mapping (31). Figure 3.2 presents an example of the use of PIV technique (more details about the technique, section 3.1.2) in the



monitoring of cardiac cycle in the left ventricle. In the early diastolic period (A), an irrotational flow associated with early left ventricular (LV) filling dominated the vector representation of flow. In diastasis, a relatively apically located vortex was seen (B, arrow). This was followed by a late filling phase that was characterized by an irrotational flow obscuring the vortex (C). In the early isovolumic contraction (IVC) period, the vortex was relocated in the proximity of the anterior mitral leaflet in the LVOT region (D, arrow). During the late IVC period, the vortex persisted in the left ventricular outflow tract region and directed flow towards aortic valve (E). With the aortic valve opening and ejection (F), the vortex dissipated with continued flow from apex to left ventricular outflow tract.

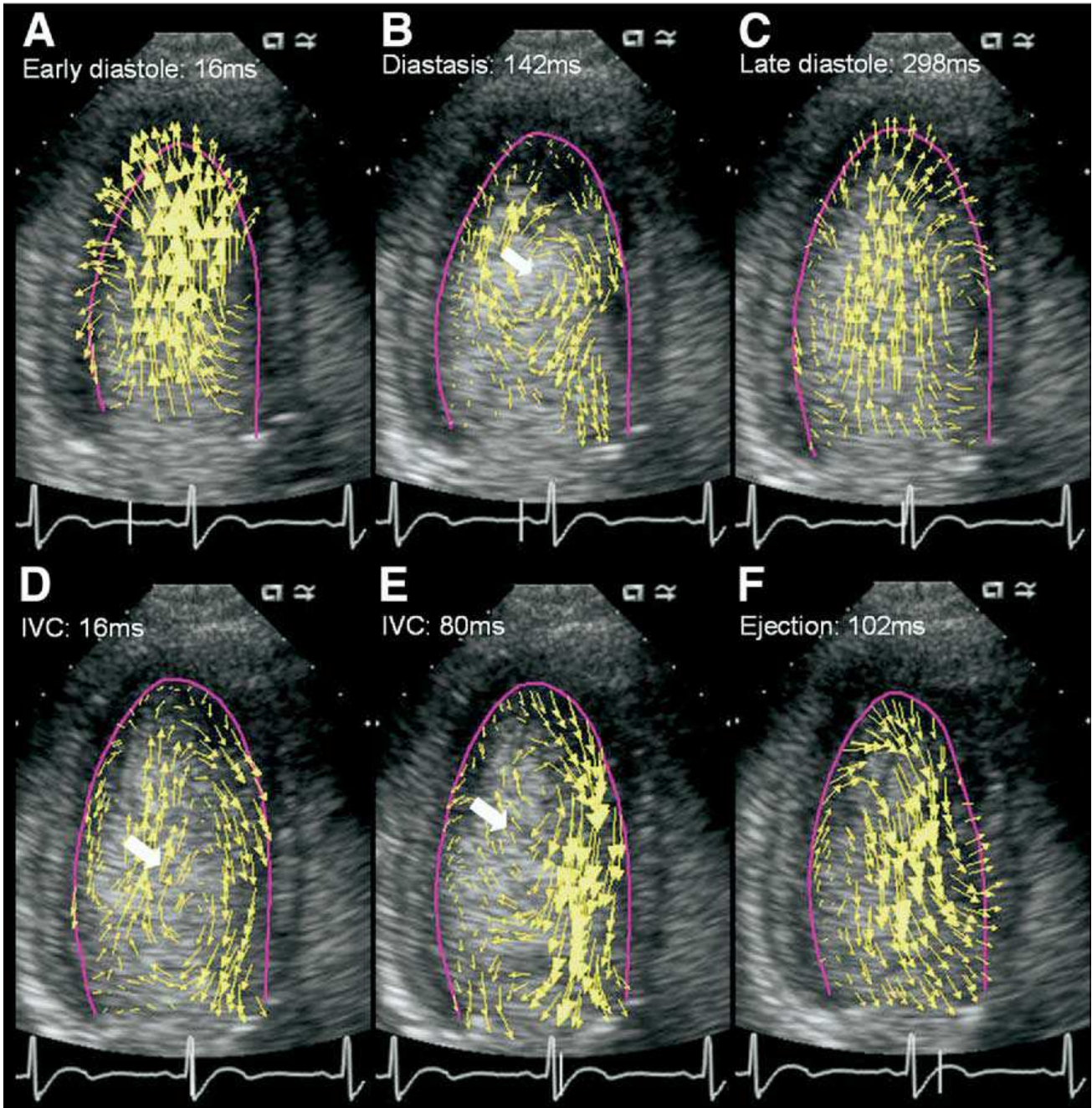


Figure 3.2 Time sequence analysis of LV flow during diastole and IVC period in normal subjects. Early diastole: 16 ms after mitral valve opening (A); diastasis: 142 ms after mitral valve opening (B); late diastole: 298 ms after mitral valve opening (C); IVC-1: 16 ms after mitral valve closure (D); IVC-2: 80 ms after mitral valve closure (E); ejection: 102 ms after mitral valve opening (F) (32)

## 3.3 Doppler assessment of diastolic LV filling

### 3.3.1 Introduction

Because of their noninvasive nature and ease of use, echo-Doppler techniques have become the accepted clinical standard for assessing LV diastolic function. They provide information about a great number of parameters which define diastolic function:

- Mitral inflow velocities
- Pulmonary venous flow
- Flow durations, isovolumic times
- Mitral regurgitation velocity
- Flow propagation (color MM)
- Doppler tissue imaging
- Volume loading and unloading
- Respiratory variations
- Exercise

This section explains the basis of the Doppler Normal Mitral flow and Doppler Tissue Imaging techniques because they are the most widely use to measure the flow through the mitral valve. This velocity profile will be used as input when developing the fluid dynamic model. Color M-mode is also briefly presented because it provides a spatiotemporal distribution of the velocity providing useful information when analyzing patients with different heart diastolic disease, showing the importance of knowing the flow behavior. Finally, the normal pulmonary flow is also explained because it is commonly used when evaluating diastolic dysfunction.

### 3.3.2 Normal transmitral Doppler flow velocity pattern

Doppler echocardiography provides a noninvasive means to study LV diastolic function by recording transmitral blood flow velocities versus time. These velocity waveforms are determined by the complex interplay of hemodynamics (instantaneous pressure differences) and several other factors.

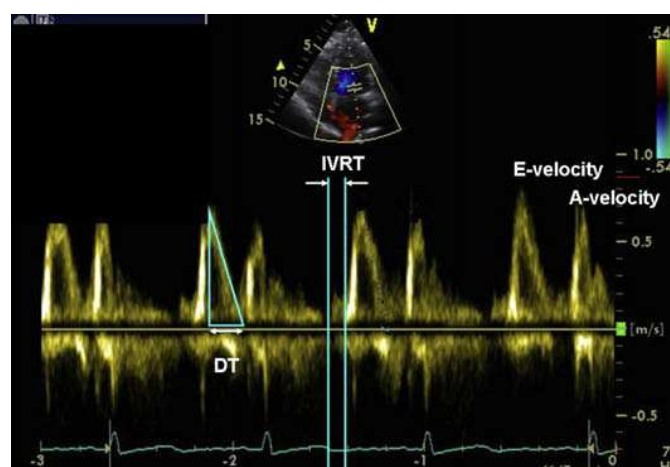


Figure 3.3. Mitral inflow velocities profile on pulse wave Doppler. A-velocity, atrial component of mitral filling; DT, deceleration time; E-velocity, IVRT, early diastolic mitral inflow velocity.(33)

Figure 3.4 diagrammatically shows the normal transmitral Doppler flow velocity pattern and the parameters which can be measured. The isovolumic relaxation period (IRP) is the interval between aortic valve closure (Ac) and the onset of LV filling at mitral valve opening (Mo). The time interval between the end of the outflow tract velocity and the onset of the mitral inflow velocity waveform represents IRP. During relaxation there is a pressure cross-over between left atrial and left ventricular pressure, which causes the mitral valve to open and rapid filling to occur (E wave). E wave acceleration is directly determined by LA pressure and inversely related to myocardial relaxation. In this part of the cardiac cycle LV relaxation is still ongoing causing a continuing drop in LV pressure. The area under the E wave is the time velocity integral (TVI) and reflects the contribution of the rapid filling phase in the LV diastolic filling. The viscoelastic properties and compliance of the myocardium then come into play, raising LV pressure and resulting in a decreased transmitral flow velocity. The deceleration time (DT) is a measure of how rapidly early diastolic filling stops. It is represented by the time-interval between the E peak and a point on the baseline where the descending limb crosses the baseline. There is an inverse relationship between the mean LA pressure and DT. Inertia effects may cause continued forward low velocity flow during mid-diastole. DT becomes shorter when LV compliance decreases. The higher LA pressure during its contraction causes an increase in velocity (A wave) and is an important parameter of diastolic function. The A wave is associated with atrial contraction and is an important index of diastolic function. The area under the A wave is the time velocity integral (TVI) and reflects the contribution of atrial contraction to LV diastolic filling.

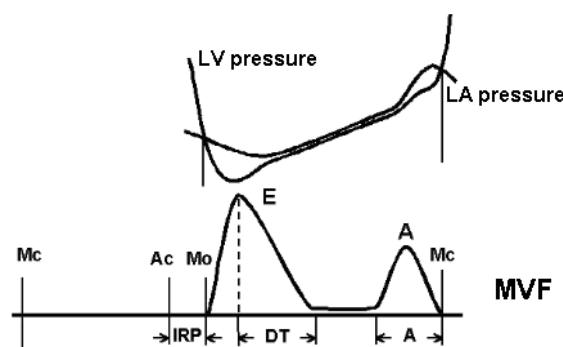


Figure 3.4. Left ventricle and left atrium pressure and mitral valve flow (MVF)

Thus, the quantitative measurements that can be made from the Doppler velocity curve include:

- **Maximum velocities:** The E velocity, the A velocity, and their ratio
- **Velocity-time integrals:** Total, early diastolic, atrial contribution and their ratios
- **Time intervals:** The isovolumic relaxation time (IVRT), the total duration of diastole, the deceleration time, and the atrial filling period. The measure of the IVRT is useful in determining the severity of diastolic dysfunction, particularly in serial studies of patients on medical therapy or with disease progression. Impaired relaxation is associated with a prolonged IVRT whereas decreased compliance and elevated filling pressures are associated with a short IVRT.
- **Measures of acceleration and deceleration:** The time from onset of flow to the E velocity, the maximum rate of rise in velocity and the slope of the early diastolic deceleration.

Combining Doppler left ventricular inflow velocity data with the cross-sectional area of the mitral annulus, additional filling parameters that can be calculated include:

- **Peak filling rates:** Peak rapid filling rate, atrial peak filling rate and their ratio.



- **Stroke volume:** This is, the volume of blood pumped from one ventricle of the heart with each beat
- **Fractional filling rates:** For example, first third filling fraction or the ratio of early to late filling.

### 3.3.3 Doppler tissue velocity imaging.

Tissue Doppler imaging (TDI) is an echocardiographic technique employing the Doppler principle to measure the velocity of myocardial segments and other cardiac structures (34). Alteration of filters and scales permits use of the modality to measure high amplitude, low velocity data from moving muscle - these adjustments permit tissue Doppler imaging (TDI).

TDI allows quantitative assessment of the motion of the myocardium (middle of the three layers forming the wall of the heart) and is particularly helpful in quantifying ventricular long axis function. TDI can be used to assess both regional and global left ventricular function. Measuring myocardial velocities gives information about regional ventricular contractility, while, as a consequence of the relative immobility of the cardiac apex, the measurement of mitral annular velocities provides information on longitudinal left ventricular function. Regardless of the site of the measurement, the normal TDI profile has a characteristic appearance, consisting of systolic and diastolic myocardial motion (Figure 3.5). Systolic motion often has two peaks,  $S'$  and  $S_m$ .  $S'$  reflects isovolumic contraction, while  $S_m$  occurs during ejection. Diastolic velocities, seen as troughs, consist of early and late myocardial movement ( $E_m$  and  $A_m$ ). These correspond to passive ventricular filling and atrial contraction, as do the E and A waves of transmitral flow. Mitral annular velocities are less preload dependent than conventional Doppler indices of mitral inflow although the diastolic waveforms are not entirely preload independent (34).

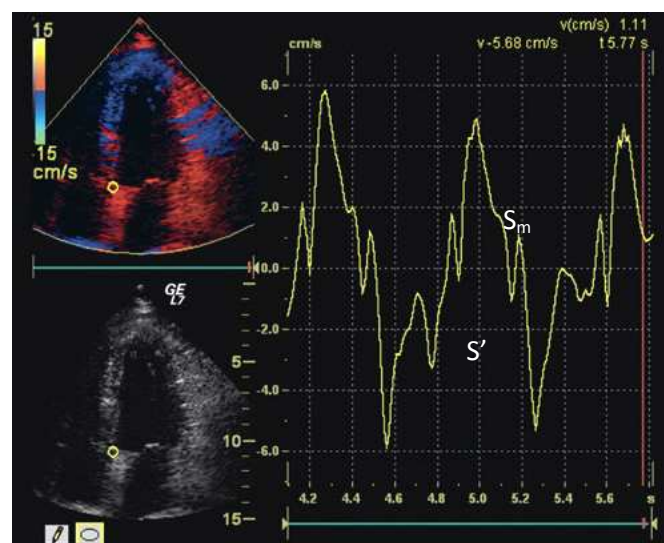


Figure 3.5 TDI trace obtained from the mitral annulus.  $A_m$ , late (atrial) diastolic myocardial motion;  $E_m$ , early diastolic myocardial motion;  $S'$ , early systolic myocardial motion;  $S_m$ , late systolic myocardial motion.

### 3.3.4 Color M-mode transmitral flow

Color Doppler M-mode echocardiography provides a spatiotemporal map of blood distribution ( $v(s,t)$ ) within the heart, with a typical temporal resolution of 5ms, a spatial resolution of 300 microns, and a velocity resolution of 3cm/s. Assessment of diastolic flow propagation has offered novel information about LV filling dynamics and has been applied in a variety of clinical conditions. Since the initial description by Jacobs (35) and later Brun (36), computer simulation (37), in vitro modeling (38) and animal (31, 39) and clinical studies (31, 36, 39-41) have improved the understanding of the determinant of the velocity of flow propagation into

the LV ( $V_p$ ) but also have shown the complexity of this index.  $V_p$  appears to be relatively independent of loading conditions and therefore may overcome one of the main limitations of Doppler-based techniques (31, 36, 41, 42).

Figure 3.6 shows a representative recording of the M-mode color Doppler flow mapping of the mitral inflow and the left ventricular pressure (LVP). The time constant of isovolumic LV pressure decay ( $\tau$ ) was smaller and the minimum value of the first derivative of LV pressure curve ( $dP/dt_{min}$ ) was greater when the early diastolic mitral flow propagation velocity ( $V_p$ ) was greater in each cardiac cycle.

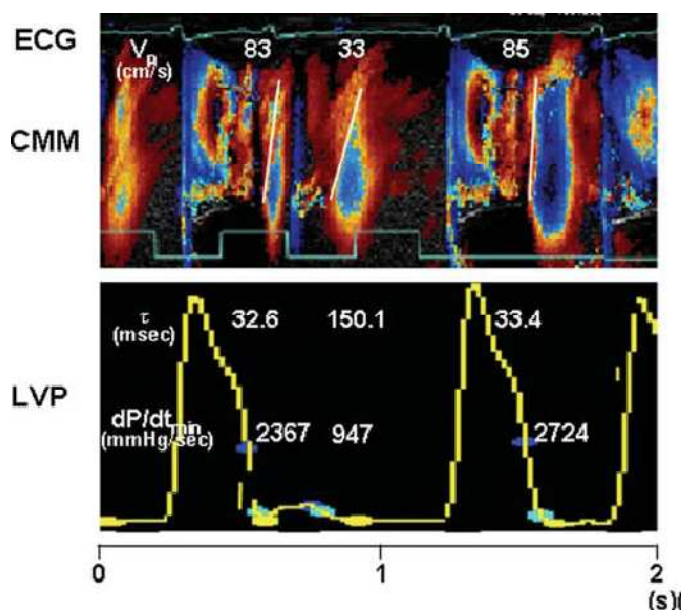


Figure 3.6. M - mode color Doppler for the mitral inflow (43)

### 3.3.5 Normal Pulmonary vein Doppler Flow velocity pattern

The normal pulmonary vein flow pattern is sketched in Figure 3.7. It is usually biphasic with a predominant systolic forward flow (S wave) and a less prominent diastolic forward flow wave (D wave). Occasionally, there may be a triphasic flow pattern with two distinct systolic flow waves of which the initial flow into the left atrium results from atrial relaxation followed by a further inflow due to the increase in pulmonary venous pressure. The D-wave occurs when there is an open conduit between the pulmonary vein, LA and LV and reflects the transmitral E wave. A retrograde flow wave into the pulmonary vein ( $A_R$  wave) occurs during atrial contraction and its amplitude and duration are related to LV diastolic pressure, LA compliance and heart rate. In normal subjects, the amplitude of the  $A_R$  wave is generally less than 25 cm/sec and its duration is shorter than the A wave of the transmitral A wave.

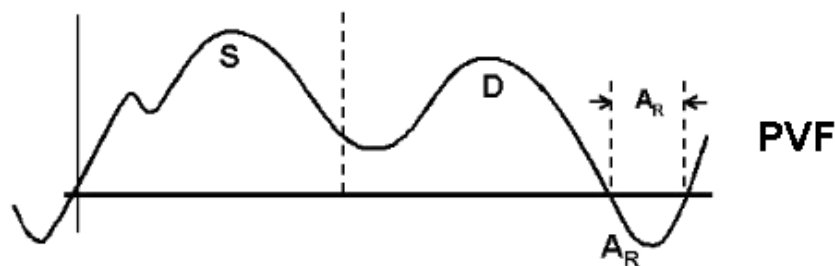


Figure 3.7. Pulmonary vein flow

## 3.4 Diastolic heart failure

### 3.4.1 Introduction

Heart failure can be defined physiologically as an inability of the heart to provide sufficient forward output to meet the perfusion and oxygenation requirements of the tissues while maintaining normal filling pressures (44). Chronic heart failure can be divided into two broad categories: systolic heart failure (SHF) and diastolic heart failure (DHF). In systolic heart failure, there is reduced cardiac contractility, whereas in diastolic heart failure there is impaired cardiac relaxation and abnormal ventricular filling. The Cardiovascular Health Study and the Strong Heart Study, both in the United States, show a greater incidence for DHF at 55% and 53% respectively than SHF. Diastolic heart failure is now recognized as a major national health problem, especially in the elderly, who have a high incidence of LV hypertrophy (LVH).

The main characteristics and clinical manifestations of diastolic and systolic heart failure are summarized in Table 3.1.

Table 3.1. Characteristics and clinical manifestations of SHF and DHF

SHF	DHF
<ul style="list-style-type: none"> <li>•Characteristics</li> <li>•Progressive chamber dilation</li> <li>•Eccentric remodeling</li> <li>•Dominant abnormalities in systolic functions</li> <li>•Clinical manifestations</li> <li>•Decreased cardiac output</li> <li>•Increased heart rate</li> <li>•Peripheral vasoconstriction</li> </ul>	<ul style="list-style-type: none"> <li>•Characteristics</li> <li>•Normal LV volume</li> <li>•Concentric remodeling</li> <li>•Abnormalities in diastolic relaxation, filling and/or distensibility</li> <li>•Clinical manifestations</li> <li>•Shortness of breath at rest or with exertion</li> <li>•Peripheral edema</li> </ul>

There has been increasing recognition that diastolic ventricular function often plays an essential role in the clinical manifestations of disease in patients with a wide range of cardiac disorders. For example, many patients with clinical heart failure have normal systolic function with predominant diastolic dysfunction. Diastolic dysfunction may be an early sign of cardiac diseases (as in hypertension), often antedating clinical or echocardiography evidence of systolic dysfunction. In addition, the degree of diastolic dysfunction may explain the difference in clinical symptoms between patients with similar degrees of systolic dysfunction(45).

Despite this new appreciation of the importance of both systole and diastole in maintaining normal cardiovascular physiology, the role of LV diastolic function in health and disease is not completely understood. Physical examination echocardiography (ECG), chest radiographs and laboratory studies are unreliable in diagnosis diastolic heart failure in most individuals, and invasive measurement of LV diastolic properties and pressures are impractical in clinical practice. Therefore, at present, assessing the type and degree of LV diastolic dysfunction relies on evaluating the pattern of LV filling with the different techniques presented in sections 3.1.2 and 3.3. The development of a model to simulate LV filling will help to understand the dynamics of the process and improve the treatment of patients undergoing cardiac therapy.

### 3.4.2 Definition of diastolic dysfunction

A variety of cardiac diseases can cause the development of abnormal diastolic function, abnormal cardiovascular remodeling, and the development of DHF. The mechanisms by which cardiovascular disease causes these outcomes include hemodynamic alterations, inhomogeneous contraction and relaxation, myocardial ischemia, and LV concentric remodeling and hypertrophy. These mechanisms can act individually to alter diastolic function but often act together to cause the development of DHF (44). The end result of impairment of either relaxation or filling is that intracardiac pressures need to increase inappropriately to achieve adequate left ventricular filling volumes for the next systolic contraction.

In the clinical scheme, diastolic dysfunction is any abnormality that causes impaired relaxation (and decreased ventricular suction), poor filling, or loss of atrial contraction. One or more of these abnormalities results in increased pressures to achieve an adequate filling volume. This translates into “diastolic dysfunction” and results in the signs and symptoms of heart failure.

### 3.4.3 Causes of diastolic dysfunction

The major abnormalities in LV diastolic function that contribute to or occur during the development of DHF include:

- Slowed, delayed and incomplete myocardial relaxation
- Impaired rate and extent of LV filling
- Shift of filling from early to late diastole
- Decreased early diastolic suction/recoil
- Augmented LA pressure during the early filling
- Altered passive elastic properties of the left ventricle, resulting in an increased passive stiffness and decreased diastolic distensibility
- Inability to sufficiently augment cardiac output during exercise
- Inability to sufficiently augment relaxation during exercise
- Inability to utilize the Frank-Starling mechanism during exercise. Frank-Starling mechanism states that the greater the volume of blood entering the heart during diastole, the higher the preload, the more stretched the sarcomeres will be, the higher the force generated by the myocardium and the greater the volume of blood ejected during systole.
- Increased diastolic LV, LA and pulmonary venous pressures at rest or during exercise.

### 3.4.4 Assessment of diastolic dysfunction

Diastolic function can be assessed using the following measurements:

- **Left ventricular pressure decline**, quantified by the rate of isovolumic relaxation. When the isovolumic relaxation is abnormal, LV pressure declines slower
- **Left ventricle filling dynamics** where the three diastolic filling phases can be distinguished: rapid filling of the left ventricle, during which  $dV/dt$  reaches its maximum and the peak filling rate occurs; a slow filling phase (diastasis), during which there is little change in LV volume and atrial systole phase, during which active atrial contraction fills the left ventricle and allows it to attain its end diastolic volume. Important diastolic parameters include the peak filling rate, the time to peak filling rate, the rapid filling fraction (percent of total stroke volume reached during rapid filling) and the percent contribution of atrial systole to LV filling.

- **Passive elastic stiffness properties.** In patients with DHF, the diastolic pressure-volume curve is shifted up and left, indicating an increase in passive stiffness and a decrease in distensibility of the left ventricle.

### 3.4.5 Stages of diastolic dysfunction

The **New York Heart Association (NYHA) Functional Classification** provides a simple way of classifying the extent of heart failure. It places patients in one of four categories based on how much they are limited during physical activity. The stages of diastolic dysfunction are graded from I to IV.

- **Grade I:** It is called abnormal relaxation pattern and it is the mildest form of diastolic dysfunction. This pattern may develop normally with age in some patients and many grade I patients will not have any clinical signs or symptoms of heart failure.
- **Grade II:** It is called pseudonormal filling dynamics. This is considered moderate diastolic dysfunction and is associated with elevated left atrial filling pressures. These patients more commonly have symptoms of heart failure and many have left atrial enlargement due to the elevated pressures in the left heart.
- **Grade III and IV:** They are called diastolic restrictive filling dynamics. These are both severe forms of diastolic dysfunction and patients tend to have advanced heart failure symptoms. The presence of either class III or IV diastolic dysfunction is associated with a significantly worse prognosis. These patients will have left atrial enlargement and many will have a reduced left ventricular ejection fraction indicating a combination of systolic and diastolic dysfunction.

No one single echocardiographic parameter can be used to obtain an accurate diagnosis of diastolic heart failure. Multiple echo parameters have been proposed including mitral inflow velocity patterns, pulmonary vein flow patterns, tissue Doppler measurements, and M-mode echo measurements (see Figure 3.8). Algorithms have been developed which combine multiple echocardiographic parameters to diagnose diastolic heart failure (46).

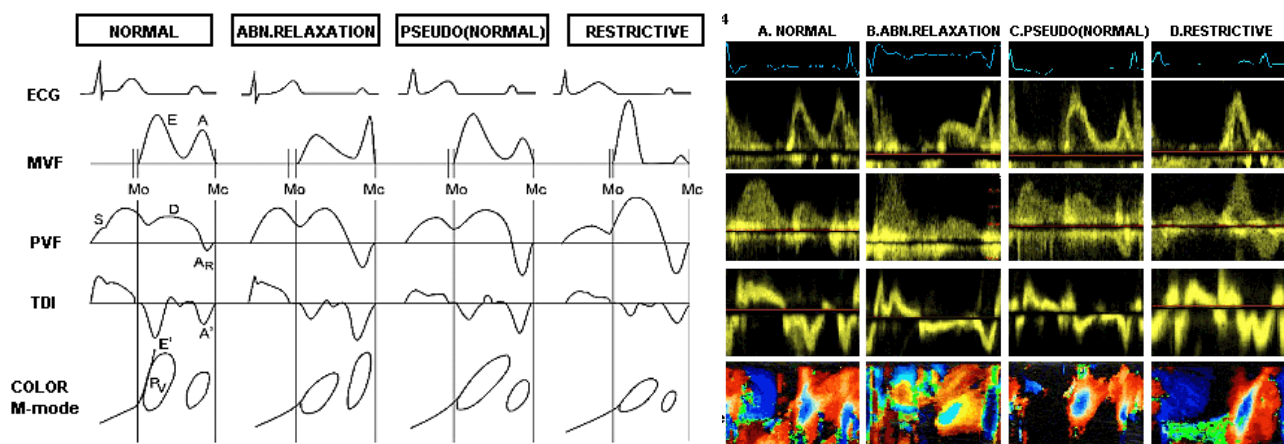


Figure 3.8. Diagrams (left) and recorders (right) showing typical mitral valve flow (MVf), pulmonary vein flow (PVf), tissue Doppler mitral annulus velocity (TDI) and color M-mode patterns of the various stages of diastolic heart failure (46).

## 3.5 Pacing and diastolic heart failure

### 3.5.1 Introduction

When the normal autonomous pacemaking activity is altered, it becomes essential to restore ventricular function. This can be done by applying an artificial stimulus, through the use of a pacemaker, to heart muscle. Pacemakers generate an electrical charge through electrodes that produce action potentials in myocardial cells. These action potentials, stimulate the surrounding myocardium (capture), and a wave of electrical discharge (depolarization) moves from the electrode to energize cardiac chambers (44).

Different types of pacemakers can be distinguished according to the chamber being paced, the chamber being sensed, and the response of the pacemaker to the sensed impulse. Since the advent of pacing therapy in 1958, tremendous improvement in technology has produced more sophisticated, efficient and compact pacemakers. The pacing sites, pacing modes and baseline heart function influence diastolic heart function, and various authors have reported the effects of pacing on one or more diastolic function parameters.

Today, thanks to developments in microelectronics, the devices are smaller, the programming options wider, and the pacing leads thinner but longer lasting than before. All these developments, in both hardware and software, have aimed at the primary goal of appropriate electrical correction of pulse and conduction defects in such a way as to simulate the natural, inherent electrical function of the heart as closely as possible and to satisfy the patient's needs while minimizing side effects. In addition, increased device longevity and the elimination of major and minor complications resulting from treatment have also been the constant aims of both manufacturers and physicians.

### 3.5.2 Cardiac resynchronization therapy

In approximately 30% of patients with heart failure, an abnormality in the heart's electrical conducting system (called an "intraventricular conduction delay" or bundle branch block) causes the two ventricles to beat in an asynchronous fashion. That is, instead of beating simultaneously, the two ventricles beat slightly out of phase. This asynchrony greatly reduces the efficiency of the ventricles in patients with heart failure, whose hearts are already damaged.

Cardiac resynchronization therapy (CRT, which is alternative called biventricular pacing) re-coordinates the beating of the two ventricles by pacing both ventricles simultaneously. A CRT device sends small, undetectable electrical impulses to both ventricles to help them beat together in a more synchronized pattern. This improves the heart's ability to pump blood and oxygen to the body.

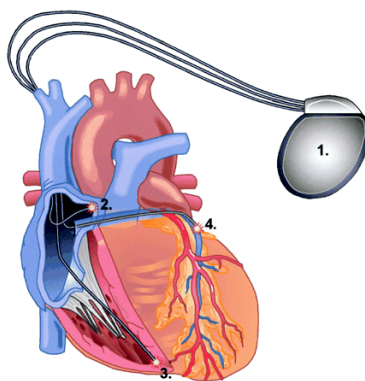


Figure 3.9. CRT. 1. Pacemaker generator; 2. Right atrial pacer wire; 3. Right ventricular pacer wire; 4. Left ventricular pacer wire (47).



Early studies with CRT demonstrated its ability to improve the symptoms, the exercise capacity, and the feeling of well-being of many patients with moderate to severe heart failure. Additional studies showed that CRT can improve over time both the anatomy and function of the heart - tending to reduce the size of the dilated left ventricle, and improving the energy usage of the heart. However, up to 35-40% of patients undergoing CRT does not respond favorably. The reasons for this are not completely known but may be dependent on proper programming, which enable the LV contraction to take place under the most appropriate hemodynamic conditions. An understanding of the positive and negative effects of pacing is imperative in order to appropriately apply pacing modalities and appropriate configurations when treating patients. Although in many instances a predictable result can be anticipated when applying pacing therapy to a given condition, it is important to recognize that interrogation of ventricular function (systolic and diastolic) is necessary to confirm the anticipated results. A better mechanical understanding of how blood is transported in the LV may help in the development of an efficient method for optimization

### 3.5.2.1 Optimization of atrioventricular (AV) delay and diastolic function

The AV delay is the time between the atrial beat and the corresponding ventricular paced event. A long AV delay gives the ventricle a lot of “opportunity” to beat on its own before the ventricular output pulse is delivered. If AV timing is too long, intrinsic and dyssynchronous ventricular activity can break through. When AV timing is too short ventricular filling time may be cut short and hemodynamics can be impaired. The goals of AV optimization are:

- Allow adequate time for passive filling of the ventricles
- Allow adequate time for a complete atrial contraction
- Allow for ventricular contraction

An optimal and appropriate AV delay should result in optimum filling of the left ventricle without interruption of the A wave, thereby allowing complete diastolic filling. To optimize left ventricular filling in these patients, the AV delay must be programmed short enough to avoid premature mitral valve closure with mitral regurgitation, and long enough to avoid left atrial cannon waves. Optimization of AV timing is not only critical to achieve optimal resynchronization therapy, and in turn LV function, but it may enable some of the non-responder patients to improve functionally and hemodynamically.(48, 49)

Rokey et al. found an inverse relation between the effectiveness of atrial contraction and early diastolic filling (E wave). It was postulated that at a short AV delay, atrial contraction is aborted and the left atrium remains with a larger residual volume at end diastole. During systole, LA volume and pressure increase further, resulting in a higher AV pressure gradient after mitral opening and thus an increase in peak inflow rate. The opposite occurs with enhanced atrial emptying and an improved atrial filling fraction brought about by optimizing the AV delay. (50)

Studies have shown that optimization of AV delay results in improved NYHA functional class as well as greater cardiac output (51). An optimum AV delay is programmed when the end of the Doppler A wave (corresponding to LA contraction) occurs just before the onset of aortic systolic Doppler flow. Ritter et al. and others have reported simple and practical AV delay algorithms. Ritter’s method includes setting the AV delay to an inappropriately short then long AV interval and measuring a surrogate of the atrial electrical mechanical delay (QA) interval at each setting. This is accomplished by measuring the interval between the onset of the Q wave and the termination of the mitral A wave (52).

The iterative technique to AV delay optimization also requires the recognition of A wave truncation. Mitral inflow is recorded at programmed long sensed AV delay, such as 150 msec, then AV delay is decreased by intervals of 10-20 msec until the A – wave begins to truncate. Once the A – wave truncation is seen, AV delay is lengthened in 10 msec steps until there is no truncation. This generates an optimized AV delay when ventricular contraction occurs just at the end of the atrial contribution.

### **3.5.2.2 Optimization of intraventricular (VV) delay and diastolic function**

VV timing refers to the synchronization of RV and LV contractions. Intraventricular dyssynchrony contributes to impairment of cardiac function. The goal of VV timing optimization is to get the ventricles to contract as a unified whole.

Current generations of CRT devices also allow for optimization of ventricle to ventricle (VV) timing. In patients with heart failure and LV dyssynchrony, proper timing of the intraventricular pacing interval (VV interval) may further optimize LV function. Although the proper timing of the VV interval is clearly beneficial in select patients, a definite benefit of this feature has not yet been proved. Specific measurements for ventricular dyssynchrony correlate with hemodynamic changes in patients with biV pacing compared with simultaneous biV pacing increases cardiac output and decreases mitral regurgitation in patients with heart failure (53, 54).

Van Gelder et al. studied LV dp/dt in patients with severe LV dysfunction. They were able to elicit additional increase in dp/dt after optimizing the VV interval (3% - 8%). Maximum dp/dt was achieved with pacing “LV first” in 44 patients; simultaneous right and LV” pacing in 6 patients; and “RV pacing first” in 3 patients. Such benefit has attributed to improved LV synchrony, resulting in a change in preload and reduction in mitral regurgitation (55).

It has been suggested to be an intraventricular delay that reduces LV dyssynchrony and/or maximizes LV systolic function. Sogaard et al. evaluated the impact of sequential CRT with individualized intraventricular delay programming. Simultaneous CRT was better than “no CRT” in reducing delayed longitudinal contraction (DLC) (from 45% to 23%,  $p < 0.01$ ) and increasing ejection fraction (EF) (from 22% to 29%,  $p < 0.01$ ). However, optimum sequential CRT (preactivation of the left ventricle in 9 patients and of the right ventricle in 11) caused a further reduction in the extent of DLC from 33% to 23 % and increase EF from 29% to 33%. Without any further optimization of AV delay, the diastolic filling time increased from  $430 \pm 88$  msec during simultaneous CRT to  $460 \pm 80$  msec during optimum sequential CRT (56).

All these approaches neglect the fact that the flow has its own fluid timings. They only think in terms of pressures but nobody has looked at how the fluid is actually transported. LV vortices act as a conduction belt for blood that enters the ventricle. Better knowledge of the dynamics of these vortices may contribute to increase our understanding of the effects of AV and VV delays. The development of a model to simulate LV filling will allow us to modify the delays and check how the efficiency of the filling depends on that. We want to be able to optimize CRT not based on how the signals should be in a healthy heart but on which is the way to optimize a sick heart.



# Chapter 4

---

## 4 Fluid dynamic model

Previous chapters described the great complexity of the cardiac cycle in general and the diastole in particular. This chapter justifies a set of simplifications that will allow the problem to be posed in the form of equations. The development of a numerical code to simulate the blood flow transport in the left ventricle has a great importance because the current protocols for CRT for patients with DHF are not successful. A simplified model can be used as a guideline to identify the values of time delay between pulses that optimize the filling of the LV of a given patient.

### 4.1 Introduction

Modeling the intraventricular flow is demanding because ventricular motion affects blood flow, but blood flow itself affects ventricular motion. McQueen & Peskin (57) model cardiovascular tissue as being elastic, having essentially uniform mass density, and apply a modified form of the Navier-Stokes equations to the four chambered heart and great vessels. Using a supercomputer their solution provides fluid, wall and valve motion as a function of space and time. Their computed results are consistent with flow attributes observed in vivo via cardiac MRI. Kovacs (57) focuses on the physiology of diastole. The suction pump attribute of the filling ventricle is modeled as a damped harmonic oscillator. The model predicts transmitral flow-velocity as a function of time. Full fluid-structure interaction models are being developed in which movement of the blood and muscle is not known a priori but is computed during the simulation. Furthermore, most commercially available software programs allow only small strain deformations (up to 5%) and are

inadequate for cardiac modeling, where strains may exceed 50%. Currently, no model can predict the impact of structural changes of LV shape on flow propagation within the LV.

Some simplification is possible with computational fluid dynamics models, where LV motion is prescribed based on images from echocardiography or magnetic resonance imaging, but these models lack fluid feedback on the myocardium. Using the contour of the clinical Doppler echocardiographic E and A-wave as input, solution of Navier Stokes equations allows calculating intraventricular diastolic flow. The specific aim of this project is to develop a numerical code to evaluate the effect of the AV and VV delays on blood flow transport in the LV, in particular, to understand the effect of these timings on the properties of the vortex that is formed in the LV, under the following working simplifications:

- The flow entering the ventricle is imposed.
- The motion of the left ventricle is prescribed, ignoring fluid-structure interaction.

## 4.2 The inlet flow

Oxygenated flow coming from the pulmonary systems enters into the left ventricle through the mitral valve during diastole at a certain speed that can be measured using non-invasive techniques such as the ones described in section 3.1.2. The most widely used imaging modalities are the ones based on the use of ultrasounds (Doppler techniques, section 3.3). Figure 4.1 shows a typical normal transmitral Doppler flow velocity pattern.

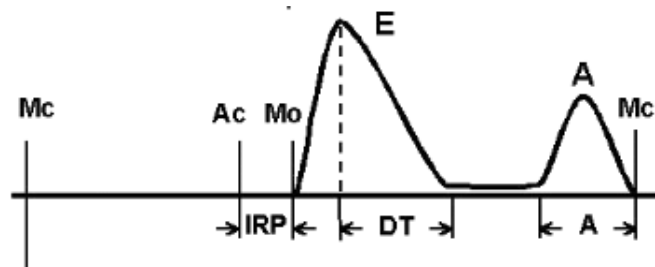


Figure 4.1. Mitral valve velocity profile

The normal E velocity in healthy, young individuals is approximately 1 m/s with an A velocity of 0.4 to 0.2 m/s, reflecting the normally small contribution of atrial contraction to left ventricular diastolic filling. If diastole is long enough, a period of no inflow, or diastasis, between the two flow curves is seen.

Even in normal individuals, the pattern of left ventricular diastolic filling varies with age, loading conditions and heart rate. With age, there is a gradual reduction in E velocity, prolongation in the rate of early diastolic deceleration, and increase in A velocity so that the ratio of E to A velocity changes from greater than 1 in young individuals, to approximately 1 at ages 50 to 60, to less than 1 in older normal individuals.

An increased preload result in an increase in E velocity and decreased preload has the opposite effect. When diastole is short (i.e., with a rapid heart rate), the A velocity becomes superimposed (or summated) on the down-slope of the E velocity, resulting in an apparent higher A velocity. At very high heart rates, only a single E/A peak may be seen. This happens for instance in neonates. These variations in the normal pattern of left ventricular diastolic filling should be recognized to avoid an inappropriate interpretation of an

“abnormality”. Table 4.1 shows how these parameters vary from normal patients to patients with different grade of diastolic heart failure.

Table 4.1. Assessment of diastolic dysfunction through transmitral Doppler velocities (46)

	Normal	Grade I	Grade III and IV
IRP <40 yrs	70±12 ms	>110ms	<60ms
>40 yrs	80±12 ms	>110ms	<60ms
DT	200±32 ms	>240ms	<150ms
E-Wave	0.85±0.15 m/s	<0.50m/s	>1.20m/s
A-Wave	0.55±0.15 m/s	<0.50m/s	<30m/s
E/A ratio	>1	<1	>2

We are seeking for a general knowledge about the influence of AV and VV delays on LV hemodynamics under a whole range of conditions, so transmitral Doppler velocities will be enough to make up the inlet profile. This profile will have a parabolic shape as shows Figure 4.2.

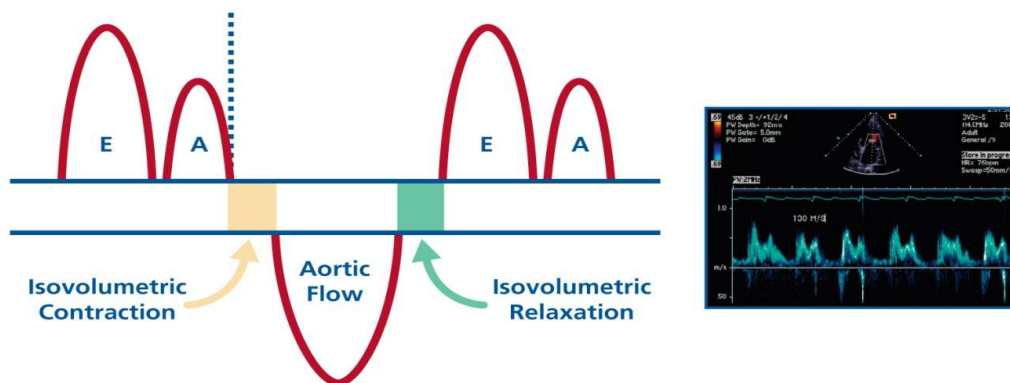


Figure 4.2. Inlet profile

## 4.3 The domain

During diastole, the ventricle relaxes and fills with blood, increasing its volume from about 50 ml at the end of systole to 120 ml at the end of diastole. Parameters such as end-diastolic dimension (EDD), end-systolic dimension (ESD) or interventricular septal end diastolic dimensions (IVSd) are commonly used to describe its shape. Studies show how shape and size of the left ventricle varies from patient to patient and it has a great influence in the performance of the heart (58).

In addition, it should be taken into account that the left ventricle undergoes complex motions. The myocardium (the middle of the three layers forming the wall of the heart) is anatomically and functionally inhomogeneous (59). The left ventricular (LV) wall is composed of both longitudinal and circular myocardial fibers. Normal systolic contraction occurs with the activity of both longitudinal and circular myocardial fibers (61, 62). However, the longitudinal fibers contract earlier than the circular fibers. As a result, early in systole (in the period of isovolumic contraction), the left ventricle undergoes geometric deformation, becoming

more spherical (63). Then, with contraction of the circular fibers, the left ventricle recovers its cylindrical shape.

The model proposed here ignores the complexity of the shape and movement of the ventricle, assuming that the ventricle is a paraboloidic chamber with a movement such that the mass is conserved. This is, when blood is entering into the domain, the volume has to increase in a way which assures that mass is constant, because blood is considered an incompressible fluid.

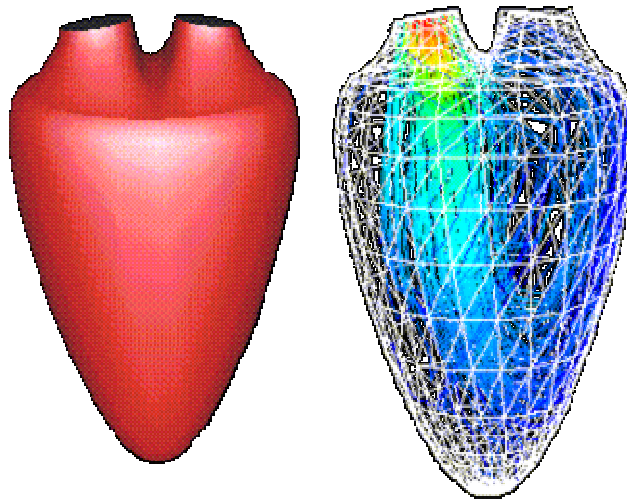


Figure 4.3. Example of a model of the left ventricle of the human heart. University of Leeds. Mathematics Applied to Biology and Medicine.

# Chapter 5

---

## 5 Numerical model

This section presents the numerical approach to the problem described in previous chapters. The problem, reduced to a set of differential equations, is discretized and solved on a staggered grid following a fractional-step method in combination with a low-storage semi-implicit Runge-Kutta method. We also use a computationally efficient method to solve the linear system of equations. At the end of the chapter, some examples validate the performance of the code.

### 5.1 Introduction

Previous chapters have provided the knowledge required to understand and simplify the filling process of the left ventricle of the heart. This is only the first stage when developing a numerical simulation of LV flow. The steps to be followed are summarized in Figure 5.1. First, the problem is formulated as a set of differential equations through the definition of a mathematical model. The discretization of the domain and the continuous governing equations transforms the problem into a discrete set of algebraic relations. Afterwards, a numerical procedure is invoked to solve the obtained linear system and obtain the local solution to the original equations. This set of equations can be solved providing a solution. Validation of this solution is a crucial step to assure its accuracy.

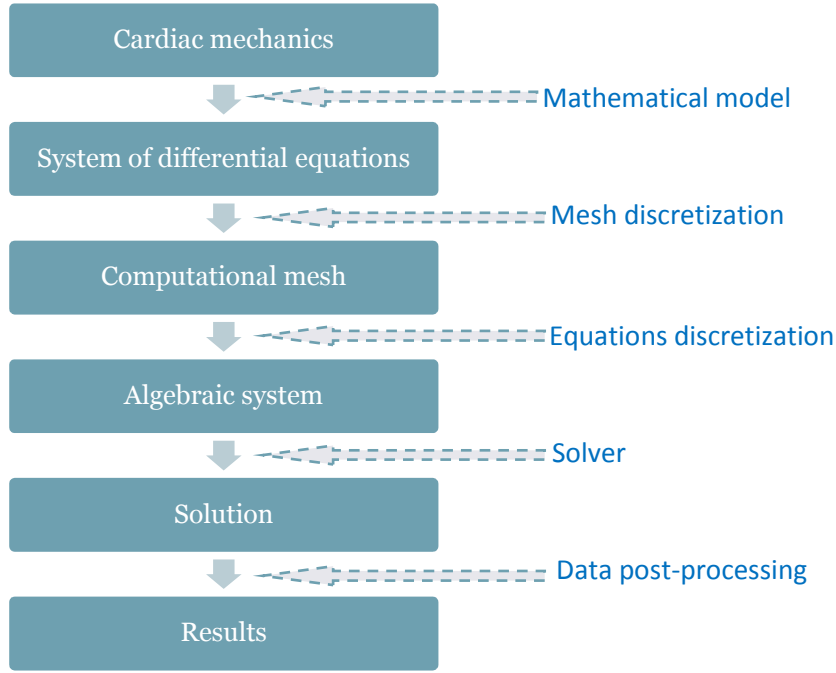


Figure 5.1. Strategy for the development of a numerical model

This chapter will follow the same structure described in Figure 5.1.

## 5.2 Mathematical model

The starting point of any numerical method is the mathematical model, i.e. the set of equations and boundary conditions which define the problem to solve. In this particular case, where blood is considered to be a fluid with constant density and viscosity (see section 2.3), Navier-Stokes (Eq. 5.1 and Eq. 5.2) equations should be solved in order to simulate the filling process of the left ventricle.

$$\nabla \cdot \vec{v} = 0 \quad \text{Eq. 5.1}$$

$$\rho \left( \frac{\partial \vec{v}}{\partial t} + \vec{v} \cdot \nabla \vec{v} \right) = -\nabla p + \mu \Delta \vec{v} \quad \text{Eq. 5.2}$$

Expressing the equations in a conservative two dimensional-Cartesian (x,r) form, the problem becomes,

$$\frac{\partial u_x}{\partial t} + \frac{\partial u_x^2}{\partial x} + \frac{\partial u_x u_r}{\partial r} = -\frac{\partial p}{\partial x} + \frac{1}{Re} \left( \frac{\partial^2 u_x}{\partial x^2} + \frac{\partial^2 u_x}{\partial r^2} \right) \quad \text{Eq. 5.3}$$

$$\frac{\partial u_r}{\partial t} + \frac{\partial u_r^2}{\partial r} + \frac{\partial u_x u_r}{\partial x} = -\frac{\partial p}{\partial r} + \frac{1}{Re} \left( \frac{\partial^2 u_r}{\partial x^2} + \frac{\partial^2 u_r}{\partial r^2} \right) \quad \text{Eq. 5.4}$$

where x and r are two Cartesian coordinates. We have preferred this notation to the standard (x,y) notation because the code will be extended to 3D cylindrical coordinates (x,r,θ) in later stages of the project.

The boundary conditions are determined by the movement of the walls and the flow in the mitral valve. When using conventional techniques, geometric complexity combined with moving boundaries requires

regeneration or deformation of the grid during the simulation, leading to a considerable increased of the computational difficulties. The discretization proposed here is based on the use of the Immersed Boundary method, which is able to handle more effectively the difficulties associated with the existing boundary conditions.

In two-dimensional incompressible flows, the formulation in terms of stream function – vorticity ( $\psi - \omega$ ) is usually favorable. This work adopts a formulation based on velocity – pressure ( $v - p$ ) due to several reasons. First of all, despite of currently having a bidimensional flow, the code will be extended in the future to the third dimension and this can only be performed maintaining a  $v - p$  formulation. In addition, this formulation is more compatible with the use of immersed boundaries (it is hard to impose boundary conditions on the vorticity), which allows an easily implementation of the numerical solution.

## 5.3 Mesh discretization

### 5.3.1 Introduction

In computational fluid dynamics, the primary issues are accuracy, computational efficiency, and, specially, the handling of complex geometry. The appropriate selection of the grid has a great influence over these issues. A grid that is not well suited to the problem can lead to unsatisfactory results, instability or lack of convergence. Thus, it is important to define a numerical grid which will establish the discrete locations at which the variables are to be calculated. Two approaches can be followed when facing this task (64) :

- **Body conformal grids**, which employ structured or unstructured grids that conform the body.
- **Non body conformal grids**, where the body would still be represented through some means such as a surface grid, but the grid would be generated with no regard to this surface grid. The governing equations will then be discretized using a certain discretization technique, for example, finite differences, without resorting to coordinate transformation or complex discretization operators.

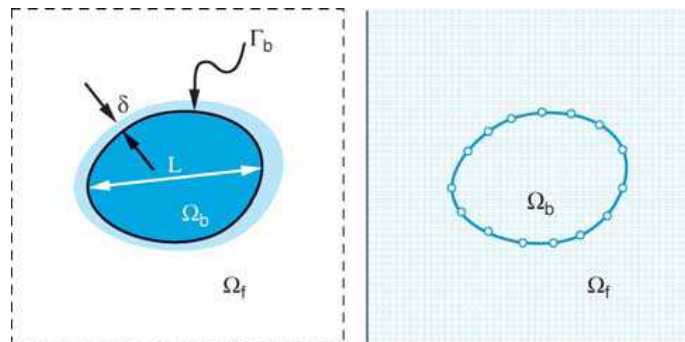


Figure 5.2. Body conformal grid (left) and non body conformal grid (right) (64)

### 5.3.2 Types of grids

In order to select the best way of solving the particular problem studied here, it is important to understand the main features of the available alternatives. This section attempts to summarize its basic characteristics.

#### 5.3.2.1 Body conformal grids

As it has been outlined before, body conformal grids employ structured or unstructured grids which fit their shape to the body. In structured grids, members of a single family do not cross each other and cross each

member of the other families only once. Unstructured grids are much more flexible and can fit an arbitrary solution domain boundary. The selection of one or other type of grids depends on the problem. Table 5.1 compares the basic features of structured and not structured grids.

Table 5.1. Comparison between structured and not structured grids.

	STRUCTURED GRIDS	NON STRUCTURED GRIDS
TYPE OF GEOMETRY	Simple	Complex
GRID GENERATION	Easy	Difficult
CELL COMPUTATIONAL EFFORT	Low	High
NUMBER OF CELLS	High	Low
FLEXIBILITY	Low	High
DATA STRUCTURE	Regular -> higher computing efficiency	Irregular -> lower computing efficiency
NUMERICAL SCHEME	Possible alignment grid/flow -> low order schemes low errors	No Possible alignment grid/flow-> high order schemes always

### 5.3.2.2 Non body conformal grids: Immersed Boundaries

The immersed boundary method allows for the solution of problems with complex geometry in a Cartesian structured grid. It is applicable to complex geometries while requiring significantly less computation than competing methods without sacrificing accuracy. Moreover, as the computational domain is very simple and independent from the geometry very different problems can be solved with minimum variations in the implementation.

The basic idea of this method is to consider the discretization of a simple, fictitious computational domain obtained by eliminating the complex object of interest. In order to obtain a realistic simulation, the effect of the presence of the object on the flow must be included in the problem. Imposition of boundary conditions of the IB is the key factor in developing an IB algorithm. It also distinguishes different methods. In the “continuous forcing approach”, the forcing due to the existence of boundaries is incorporated into the continuous equations before discretization, whereas in the second approach, which can be called the “discrete forcing approach”, the forcing is introduced after the equations are discretized. An attractive feature of the continuous forcing approach is that it is formulated independent of the underlying spatial discretization. On the other hand, the discrete forcing approach very much depends on the discretization method. However, this allows direct control over the numerical accuracy and stability.

The IB method was first developed by Peskin in 1972 to simulate cardiac mechanics and associated blood flow. In Peskin’s formulation, the fluid equations (incompressible Navier-Stokes equations) are solved on uniform Cartesian grids and the elastic fibers of the heart walls are immersed in the flow: fluid and fiber exert time varying forces on one another. A Lagrangian coordinate system moving with the local fluid velocity is attached to the fibers and tracks their location in space; the information about the position of the fibers and their forcing on the fluid is transferred to the Eulerian underlying mesh where the flow solutions is obtained. In this procedure, the resulting forcing consists of delta functions located on the first cells external to the immersed body which, therefore, cannot be adequately represented on a finite size mesh. For this reason, a smooth transition between the external fluid and internal body cells is introduced which is equivalent to spreading the delta functions over a narrow band (typically three or four nodes) across the boundary (57, 65-67).



Since Peskin introduced this method, numerous modifications and refinements have been proposed and a number of variants of this approach now exist. Briscolini and Santangelo (68) used an immersed boundary approach to compute the unsteady 2D flow around circular and square cylinders at Reynolds numbers up to 1000 whereas Goldstein, Handler and Sirovich (69) considered the 2D start up flow around a circular cylinder and 3D plane and ribbed-turbulent channel flow. In these works, the IB approach is used in conjunction with spectral methods and the forcing is applied in a band (consisting of three to four computational nodes) around the interface. All of them fit in what it has been called before continuous forcing approach.

Mohd-Yushof (70) suggested a discrete forcing approach that introduces a body-force  $\vec{f}$  such that the desired velocity distribution is obtained at the boundary. In principle, there are no restrictions on the velocity distribution of the boundary. The method costs no more than the base computational scheme. Fadlun applied this approach to a three dimensional finite-difference method on a staggered grid and showed that the approach was more efficient than the continuous forcing.

Nowadays, the challenge for the IB method lies in the representation of the wall boundaries and in providing an adequate near wall flow field resolution.

### 5.3.3 Choice of the grid

In body conformal grids, the alignment between the grid lines and the body surfaces allows better control of the grid resolution in the vicinity of the body and this has implications for the increase in grid size with increasing Reynolds. On the other hand, for anything but the simplest geometries it is difficult to generate the grid. In addition, in flows with moving boundaries the grid has to be generated each time step as well as the procedure to project the solution onto this new grid.

Using the IB method the grid generation is greatly simplified and the body motion relatively simple due to the use of a stationary, non-deforming Cartesian grid. In addition, the per grid point operation cost is small due to the absence of additional terms associated with grid transformations. On the other hand, imposing boundary conditions is not straightforward and ramification of the boundary treatment on the accuracy and conservation properties of the numerical scheme is not obvious.

Figure 5.3 presents the approaches available when deciding the discretization method. As the left ventricle is moving during its filling process, the use of IB is appropriate. There are possible options to impose the boundary conditions considering a discrete forcing approach:

- **Indirect Boundary Conditions approach**, where the forcing extends into the fluid region due to the use of a distribution function and the details of the implementation depend strongly on the numerical algorithm used to discretize the governing equations.
- **Direct Boundary Conditions approach**, where the computational stencil near the immersed boundary is modified to directly impose the boundary condition on the IB.

Direct Boundary Conditions imposition is the approach to be used because it has been shown to be simpler and more efficient (70).

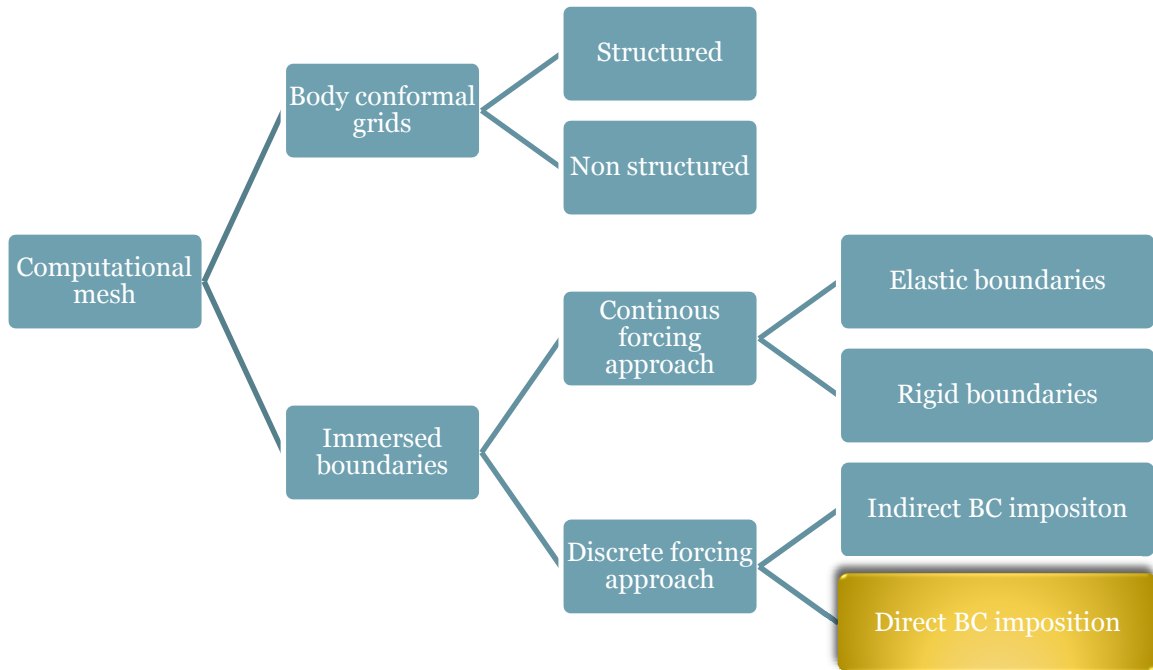


Figure 5.3. Mesh discretization techniques.

#### 5.3.4 Variable arrangement on the grid

Before turning to the discretization, it is important to select the points in the domain at which the values of the unknown dependent variables are to be computed.

The obvious choice is to store all the variables at the same set of grid points and to use the same control volumes for all variables. Such a grid is called **collocated** (Figure 5.4). Since many of the terms in each of the equations are essentially identical, the number of coefficients that must be computed and stored is minimized and the programming is simplified by this choice.

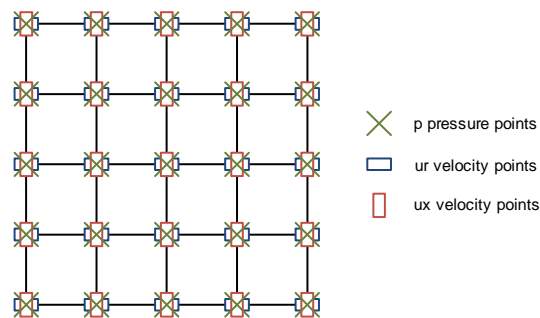


Figure 5.4. Collocated grid

There is no need for all variables to share the same grid and a **staggered arrangement** may turn out to be advantageous. Choosing an arrangement as the one presented in Figure 5.5, several terms that require interpolation with the collocated arrangement, can be calculated to a second order of approximation without interpolation. Both the pressure and diffusion terms are very naturally approximated by central difference approximations without interpolation, since the pressure nodes lie at the face centers and the velocity derivatives needed for the diffusive terms are readily computed at the faces.

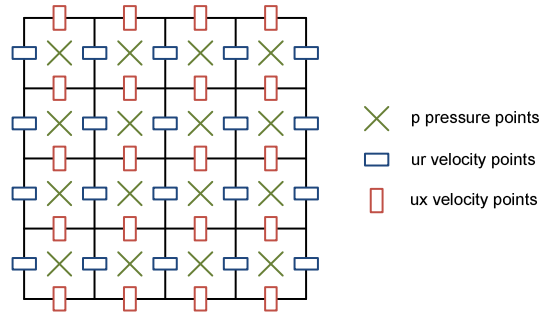


Figure 5.5. Staggered grid

The strong coupling between the velocities and the pressure in this kind of grids helps to avoid some types of convergence problems and oscillations in pressure and velocity fields (71). Furthermore, staggered meshes do not display spurious pressure modes and they have been shown to locally conserve, mass, momentum, kinetic energy, and circulation to machine precision.

In this case, the spatial discretization is performed on a staggered grid with the pressure  $p$  in the cell midpoints, the velocities  $u_x$  placed on the horizontal cell interfaces, and the velocities  $u_r$  placed on the vertical cell interfaces.

When considering the field  $p$ ,  $u_x$  and  $u_r$ , care has to be taken about interior and boundary points. Any point truly inside the domain is an interior point, while points on or outside boundaries are boundary points. The fields have the following sizes:

Table 5.2. Size of the fields.

Field quantity	Interior Resolution	Resolution with boundary points
Pressure $P$	$n_x \times n_r$	$(n_x+2) \times (n_r+2)$
Velocity component $u_x$	$(n_x-1) \times n_r$	$(n_x+1) \times (n_r+2)$
Velocity component $u_r$	$n_x \times (n_r-1)$	$(n_x+2) \times (n_r+1)$

Figure 5.6 shows a sketch of the mesh.

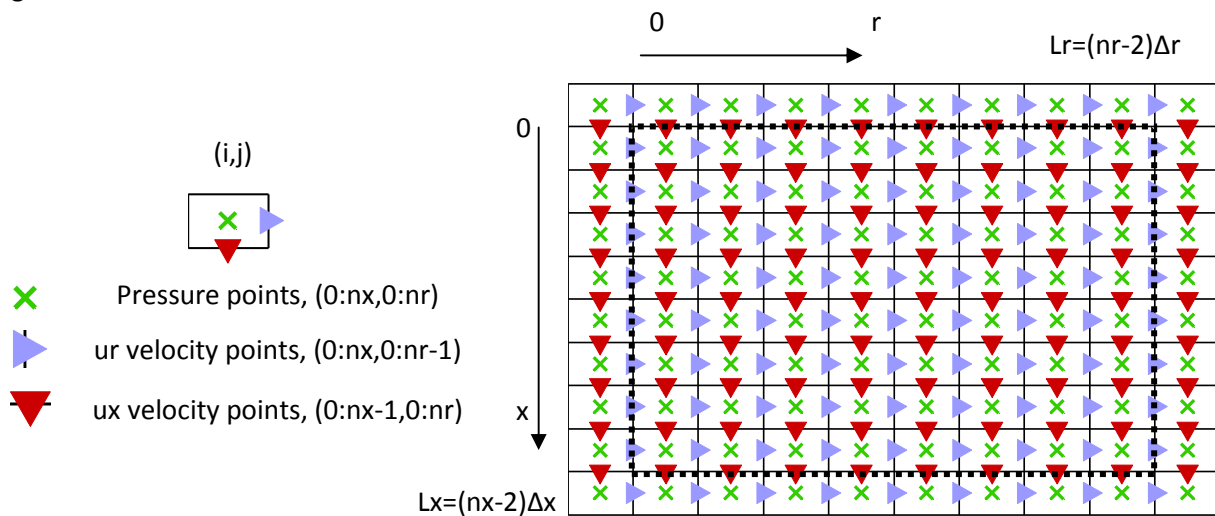


Figure 5.6. Mesh

## 5.4 Discretization of the equations

### 5.4.1 Spatial discretization

One has to select the approximations to be used in the discretization process, i. e. a method of approximating the differential operators by a system of algebraic equations for the variables of interest. There are many approaches, but most compatible with immersed boundary method are:

- **Finite difference** (FD), where approximations for the derivatives at the grid points have to be selected.
- **Finite volume** (FV), where one has to select the methods of approximating surface and volume integrals. Rather than pointwise approximations on a grid, FV approximates the average integral value on a reference.
- **Finite element** (FE), where one has to choose the shape functions (elements) and weighting functions.

The choice influences the accuracy of the approximation. A compromise between simplicity, ease of implementation, accuracy and computational efficiency has to be made. Table 5.3 compares these approximation techniques in terms of speed, cost and versatility.

Table 5.3. Basic features of finite approximation techniques

	Speed	Cost	Versatility
Finite difference	High	High	Low
Finite volume	Medium	Medium	Medium
Finite element	Low	Low	High

Spatial discretization is closely linked to the grid discretization. This work uses a Finite Different method in a staggered matrix as explained in section 5.3.

#### 5.4.1.1 Approximating derivatives

Spatial discretization of Navier-Stokes equations requires the approximation of first and second derivative.

Finite differences can approximate second derivatives on a grid point by a centered stencil.

$$\left(\frac{\partial^2 u}{\partial x^2}\right)_{i,j} = (\partial_{xx}u)_{i,j} \approx \frac{u_{i-1,j} - 2u_{i,j} + u_{i+1,j}}{dx^2} \quad \text{Eq. 5.5}$$

If the flow variable is stored in a large column vector, then the above approximation can be represented as a large sparse block matrix.

The first derivative on a grid point can be approximated by a centered stencil,

$$\left(\frac{\partial u}{\partial x}\right)_{i,j} = (\partial_x u)_{i,j} \approx \frac{u_{i+1,j} - u_{i-1,j}}{2dx} \quad \text{Eq. 5.6}$$

$$\left(\frac{\partial u}{\partial r}\right)_{i,j} = (\partial_r u)_{i,j} \approx \frac{u_{i,j+1} - u_{i,j-1}}{2dr}$$

This, however, can yield spurious oscillations, as shown in many textbooks on numerical analysis. Here the staggered grid comes into play. Assume the point of interest is the value of  $\partial_x u$  in the middle between the points  $u_{i+1,j}$  and  $u_{i,j}$  instead of the value in the position of  $u_{i,j}$ . Then the approximation

$$(\partial_x u)_{i+\frac{1}{2},j} \approx \frac{u_{i+1,j} - u_{i,j}}{dx}$$

Eq. 5.7

$$(\partial_r u)_{i,j+\frac{1}{2}} \approx \frac{u_{i,j+1} - u_{i,j}}{dr}$$

is a stable centered approximation to  $\partial_x u$  and  $\partial_r u$  in the middle between the two points. In the staggered grid this position happens to be the position of  $p_{i,j}$ .

The calculation of the non linear terms requires the use of first derivatives. This calculation is the only case where the discretization on the staggered grid does not work directly. For instance, the product  $u_x u_r$ , which appears in the advection term of the  $u_x$  equation,

$$\partial_x(u_x^2) + \partial_r(u_x u_r)$$

Eq. 5.8

is not directly defined in the grid points. This is solved by using linear interpolation so that

$$\overline{u_x^2}^i = (u_x^2)_{i+\frac{1}{2},j} = \left(\frac{u_{x,i,j} + u_{x,i+1,j}}{2}\right)^2$$

$$\overline{u_x}^j = u_{x,i,j+\frac{1}{2}} = \frac{u_{x,i,j} + u_{x,i,j+1}}{2}$$

Eq. 5.9

$$\overline{u_r}^i = u_{r,i+\frac{1}{2},j} = \frac{u_{r,i,j} + u_{r,i+1,j}}{2}$$

where the over-bar with superscript i indicates a i-direction averaged quantity; and the over-bar with superscript j indicates a j-direction averaged quantity. Non linear terms can be written as

$$\partial_x(\overline{u_x^2}^i) + \partial_r(\overline{u_x}^j \overline{u_r}^i)$$

Eq. 5.10

and discretized as defined by Eq. 5.6. Discretization of the advection terms in the  $u_r$  momentum equation is analogous, yielding to:

$$\partial_x(\overline{u_x}^j \overline{u_r}^i) + \partial_r(\overline{u_r^2}^j)$$

Eq. 5.11

#### 5.4.2 Temporal discretization

The integration procedure consists of a fractional-step method with certain peculiarities that make it suitable for the implementation of the immersed boundary conditions. First, the theoretical basis of the procedure is presented. Then, the details of the fractional step method are described.

#### 5.4.2.1 Theoretical basis

Being  $\vec{v}$  and  $p$  dimensionless velocity and pressure fields which satisfy Navier-Stokes equations in a computational domain  $\Omega$ , representing  $H$  the non linear terms and  $L$  the laplacian linear operator, the equations to be solved are,

$$\nabla \cdot \vec{v} = 0 \quad \vec{x} \in \Omega \quad \text{Eq. 5.12}$$

$$\frac{\partial \vec{v}}{\partial t} = H(\vec{v}) + \frac{1}{Re} L \cdot (\vec{v}) - \nabla p \quad \vec{x} \in \Omega \quad \text{Eq. 5.13}$$

Defining  $\vec{v}^*$  and  $p^*$  as the approximate solutions of the previous equations which satisfy,

$$\frac{\partial \vec{v}}{\partial t} - \frac{\partial \vec{v}^*}{\partial t} = -\nabla \phi \quad \vec{x} \in \Omega \quad \text{Eq. 5.14}$$

$$\frac{\partial \vec{v}^*}{\partial t} = H(\vec{v}^*) + \frac{1}{Re} L \cdot (\vec{v}^*) - \nabla p^* \quad \vec{x} \in \Omega \quad \text{Eq. 5.15}$$

where  $\phi$  is a potential function that enforces continuity of  $\vec{v}$  (Eq. 5.12). Applying the divergence to Eq. 5.14, the following Poisson equation is obtained for  $\phi$

$$\nabla^2 \phi = \frac{\partial(\nabla \cdot \vec{v}^*)}{\partial t}. \quad \text{Eq. 5.16}$$

The boundary conditions for  $\vec{v}^*$  are equal to those for  $\vec{v}$

$$\vec{v}^* = \vec{V}. \quad \vec{x} \in \partial\Omega \quad \text{Eq. 5.17}$$

In addition, the following condition holds,

$$\vec{v}(\vec{x}, n\Delta t) \equiv \vec{v}^*(\vec{x}, n\Delta t) \quad \vec{x} \in \Omega \quad \text{Eq. 5.18}$$

$$p(\vec{x}, n\Delta t) \equiv p^*(\vec{x}, n\Delta t) \quad \vec{x} \in \Omega \quad \text{Eq. 5.19}$$

where  $n$  is a natural number. Eq. 5.13, Eq. 5.15, Eq. 5.18 and Eq. 5.19 lead to

$$\frac{\partial \vec{v}}{\partial t}(\vec{x}, n\Delta t) \equiv \frac{\partial \vec{v}^*}{\partial t}(\vec{x}, n\Delta t) \quad \vec{x} \in \Omega \quad \text{Eq. 5.20}$$

which is equivalent to

$$\nabla \phi(\vec{x}, n\Delta t) \equiv 0. \quad \vec{x} \in \Omega \quad \text{Eq. 5.21}$$

Defining the problem this way, the estimated error on all the points of the domain  $\Omega$  is,

$$\nabla \phi(\vec{x}, n \Delta t) = \mathcal{O}(\Delta t) \quad \vec{x} \in \Omega \quad \text{Eq. 5.22}$$

$$p(\vec{x}, t) \equiv p^*(\vec{x}, t) + \mathcal{O}(\Delta t) \quad \vec{x} \in \Omega \quad \text{Eq. 5.23}$$

$$\vec{v}(\vec{x}, t) \equiv \vec{v}^*(\vec{x}, t) + \mathcal{O}(\Delta t^2) \quad \vec{x} \in \Omega \quad \text{Eq. 5.24}$$

The fundamental difference between this method and classical fractional step methods defined by Spalart or by Kim and Moin (72, 73) is associated with the term  $p^*$  in Eq. 5.15 and the imposition of the restriction Eq. 5.19. This involves:

- The error in the boundary conditions for the velocity is  $\mathcal{O}(\Delta t^2)$ , no matter the boundary conditions for  $\phi$  and  $\vec{v}^*$ .
- The boundary conditions for  $\vec{v}$  are the same as those for  $\vec{v}^*$ , thus the immersed boundary method can be easily applied.
- The velocity correction due to  $\phi$  is  $\mathcal{O}(\Delta t^2)$  in all  $\Omega$  and not only in  $\partial\Omega$ .

#### 5.4.2.2 Integration procedure

The integration procedure is essentially that described in Verzicco and Orlandi (74) and it consists of a fractional-step method in combination with a hybrid third-order Runge–Kutta scheme. The advantage of the third order Runge–Kutta scheme with respect to other time-integration procedures is the improved stability condition. Indeed in this scheme each time step is advanced through three sub-steps thus implying three times more operations than the common second-order schemes; nevertheless the third-order Runge–Kutta is still advantageous since it does not require extra storage and at the same computational cost as other second-order schemes, the present scheme yields an error which is generally smaller. Eq. 5.13 can be temporally discretized through the following three sub-steps scheme.

$$\frac{u_i^{l+1} - u_i^l}{\Delta t} = -\gamma_l H(u_i^l) - \zeta_l H(u_i^{l-1}) + \frac{\alpha_l}{Re} L \cdot (u_i^l) + \frac{\beta_l}{Re} L \cdot (u_i^{l+1}) - (\alpha_l + \beta_l) \partial_i p^{l+1} \quad l = 1, 2, 3 \quad \text{Eq. 5.25}$$

Where the index  $i = 1, 2$  denotes  $x$  and  $r$  respectively, and  $l = 1, 2, 3$  denotes the sub-step. The scheme is fractionated in the following fashion:

Sub-step 1:

$$\frac{\hat{u}_i - u_i^n}{\Delta t} = -\gamma_1 H(u_i^n) + \frac{\alpha_1}{Re} L \cdot (u_i^n) + \frac{\beta_1}{Re} L \cdot (\hat{u}_i) - (\alpha_1 + \beta_1) \partial_i p^n$$

$$\frac{u_i^2 - \hat{u}_i}{\Delta t} = -(\alpha_1 + \beta_1) \partial_i \phi^1$$

$$\partial_i u_i^2 = 0 \rightarrow \partial_i^2 \phi^1 = \frac{\partial_i \hat{u}_i}{(\alpha_1 + \beta_1)}$$

$$p^2 = p^n + \phi^1 - \frac{1}{Re} \frac{\beta_1}{(\alpha_1 + \beta_1)} \partial_i \hat{u}_i$$

Eq. 5.26

Sub-step 2:

$$\frac{\hat{\hat{u}}_i - u_i^2}{\Delta t} = -\gamma_2 H(u_i^2) - \zeta_2 H(u_i^n) + \frac{\alpha_2}{Re} L \cdot (u_i^2) + \frac{\beta_2}{Re} L \cdot (\hat{\hat{u}}_i) - (\alpha_2 + \beta_2) \partial_i p^2$$

$$\frac{u_i^3 - \hat{\hat{u}}_i}{\Delta t} = -(\alpha_2 + \beta_2) \partial_i \phi^2$$

Eq. 5.27

$$\partial_i u_i^3 = 0 \rightarrow \partial_i^2 \phi^2 = \frac{\partial_i \hat{u}_i}{(\alpha_2 + \beta_2)}$$

$$p^3 = p^2 + \phi^2 - \frac{1}{Re} \frac{\beta_2}{(\alpha_2 + \beta_2)} \partial_i \hat{u}_i$$

Sub-step 3:

$$\frac{\hat{u}_i - u_i^{n+1}}{\Delta t} = -\gamma_3 H(u_i^3) - \zeta_3 H(u_i^2) + \frac{\alpha_3}{Re} L \cdot (u_i^{n+1}) + \frac{\beta_3}{Re} L \cdot (\hat{u}_i) - (\alpha_3 + \beta_3) \partial_i p^3$$

$$\frac{u_i^2 - \hat{u}_i}{\Delta t} = -(\alpha_3 + \beta_3) \partial_i \phi^3$$

Eq. 5.28

$$\partial_i u_i^{n+1} = 0 \rightarrow \partial_i^2 \phi^3 = \frac{\partial_i \hat{u}_i}{(\alpha_3 + \beta_3)}$$

$$p^{n+1} = p^3 + \phi^3 - \frac{1}{Re} \frac{\beta_3}{(\alpha_3 + \beta_3)} \partial_i \hat{u}_i$$

The super-indexes 1,2 and 3 denote the value of the variable at the beginning of each time sub-step, the tildes indicate the intermediate values of the velocities at each sub-step and the super-indexes n,n+1 indicate the value of the variables at the beginning of each time step. The velocity field is corrected through the use of the potential function  $\phi$  at the end of each sub-step to impose null divergence. The accuracy of the numerical scheme depends on the selection of the constants  $\gamma_l, \zeta_l, \alpha_l$  and  $\beta_l$ . To achieve a third order accuracy the numerical scheme should match the Taylor expansion of  $\vec{v}$  (Eq. 5.29) to third order.

$$\vec{v}(t + \Delta t) = \vec{v}(t) + (\partial_t \vec{v})_t \Delta t + \frac{1}{2} (\partial_t^2 \vec{v})_t \Delta t^2 + \frac{1}{6} (\partial_t^3 \vec{v})_t \Delta t^3 + O(\Delta t^4)$$

Eq. 5.29

This gives a system of 43 equations and 11 unknowns. 26 of this equations are dependent, thus, we have to solve a system of 17 equations and 11 unknowns. If we force the length of the sub-steps to be the same for the convective and viscous terms(72),

$$\alpha_1 + \beta_1 = \gamma_1 \quad \alpha_2 + \beta_2 = \gamma_2 + \zeta_2 \quad \alpha_3 + \beta_3 = \gamma_3 + \zeta_3$$

Eq. 5.30

This reduces the system to a system with 8 unknowns and 8 equations. The equations are (72):

First order

$$\gamma_1 + \gamma_2 + \gamma_3 + \zeta_2 + \zeta_3 = 1$$

Eq. 5.31

Second order

$$\gamma_3(\gamma_1 + \gamma_2 + \zeta_2) + \gamma_1(\zeta_3 + \gamma_2) = \frac{1}{2}$$

Eq. 5.32

$$\gamma_1 \beta_1 + \gamma_1(\gamma_2 + \zeta_2) + \beta_2(\gamma_2 + \zeta_2) + (\gamma_3 + \zeta_3)(\gamma_1 + \gamma_2 + \zeta_2) + \beta_3(\gamma_3 + \zeta_3) = \frac{1}{2}$$

Eq. 5.33



Third order

$$\gamma_1 \gamma_2 \gamma_3 = \frac{1}{6} \quad \text{Eq. 5.34}$$

$$\gamma_1^2 (\gamma_2 + \zeta_3) + \gamma_3 (\gamma_1 + \zeta_1 + \gamma_2)^2 = \frac{1}{3} \quad \text{Eq. 5.35}$$

$$\beta_3 [(\gamma_3 (\gamma_1 + \gamma_2 + \zeta_2) + \gamma_1 \zeta_3) + \gamma_1 \gamma_2 (\gamma_3 + \zeta_3) + \gamma_1 \gamma_2 (\gamma_3 + \zeta_3) + \gamma_1 \gamma_2 \beta_2] = \frac{1}{6} \quad \text{Eq. 5.36}$$

$$\gamma_3 [\gamma_1 \beta_1 + (\gamma_2 + \zeta_2) (\gamma_1 + \beta_2)] + \gamma_1 \beta_1 (\gamma_2 + \zeta_3) = \frac{1}{6} \quad \text{Eq. 5.37}$$

$$\begin{aligned} & [(\gamma_1 + \beta_2 + \beta_3) (\gamma_2 + \zeta_2) + (\beta_1 + \beta_3) \gamma_1 + \beta_3^2] \zeta_3 \\ & + [(\gamma_1 + \beta_2 + \beta_3) \gamma_3 + (\beta_1 + \beta_2) \gamma_1 + \beta_2^2] \zeta_2 \\ & + [(\gamma_1 + \beta_3 + \beta_2) \gamma_2 + (\beta_1 + \beta_3) \gamma_1 + \beta_3^2] \gamma_3 \\ & + [(\beta_1 + \beta_2) \gamma_1 + \beta_2^2] \gamma_2 + \beta_1^2 \gamma_1 = \frac{1}{6} \end{aligned} \quad \text{Eq. 5.38}$$

Unfortunately this nonlinear system of equations (Eq. 5.31-Eq. 5.38) apparently does not have solution. If we sacrifice the last equation (Eq. 5.38) the scheme is still third-order on the non-linear terms and second order on the viscous term. There is then a one-parameter family of such schemes. A good compromise between a low residual for Eq. 5.38 and the desire to have fairly even sub-steps is (72),

$$\begin{aligned} \alpha_1 &= \frac{29}{96} & \alpha_2 &= -\frac{3}{40} & \alpha_3 &= \frac{29}{96} \\ \beta_1 &= \frac{37}{160} & \beta_2 &= \frac{5}{24} & \beta_3 &= \frac{1}{60} \\ \gamma_1 &= \frac{8}{15} & \gamma_2 &= \frac{5}{12} & \gamma_3 &= \frac{3}{4} \\ \zeta_2 &= -\frac{17}{60} & \zeta_3 &= -\frac{5}{12} \end{aligned} \quad \text{Eq. 5.39}$$

### 5.4.3 Immersed boundaries

#### 5.4.3.1 Description of the method

The discrete forcing method, suggested by Mohd – Yusof (70), introduces a body force  $\vec{f}$  such that the desired velocity distribution  $\vec{V}$  is obtained at the boundary  $\Omega$ . In principle, there are no restrictions on the velocity distribution on the motion of  $\Omega$ .

$$\frac{u_i^{n+1} - u_i^n}{\Delta t} = RHS_i + f_i \quad \text{Eq. 5.40}$$

Where  $RHS_i$  contains convective and viscous terms and the pressure gradient. The forcing  $f_i$  is zero inside the fluid and is non-zero in the ghost cell zone which is used to represent the presence of complex boundary. Ghost cells are defined as cells inside the solid that have at least one neighbor inside the fluid.

The velocity ( $V_i^{n+1}$ ) and pressure fields can be extrapolated to the ghost cells using nearby fluid points and associated boundary information. Thus, the boundary condition at the IB is enforced through the use of ghost cells. As example, if the forcing  $f_i$  must yield to  $u_i^{n+1} = V_i^{n+1}$ , where  $V_i$  is the velocity at the boundary.

$$f_i = -RHS_i + \frac{V_i^{n+1} - u_i^n}{\Delta t} \quad \text{Eq. 5.41}$$

#### 5.4.3.2 Numerical procedure

The numerical procedure has the following steps:

- Detect the boundary and determine the adjacent ghost cells.
- Extrapolate to find the value of the fluid at the ghost cell value required to impose the boundary condition implicitly.
- Obtain the predicted field (intermediate velocity  $\vec{u}^*$ ) of the fractional step procedure.
- Solve the potential correction ( $\phi$ ) Poisson equation to satisfy the continuity equation
- Update the velocity field to the next time sub-step.

The computational domain is divided into three regions: the physical domain, body domain and the ghost cell domain. They are illustrated in Figure 5.7. The physical domain is the flow region. The ghost cells lie just inside the body adjacent to computational nodes in the flow domain and they are the points where the boundary conditions will be imposed

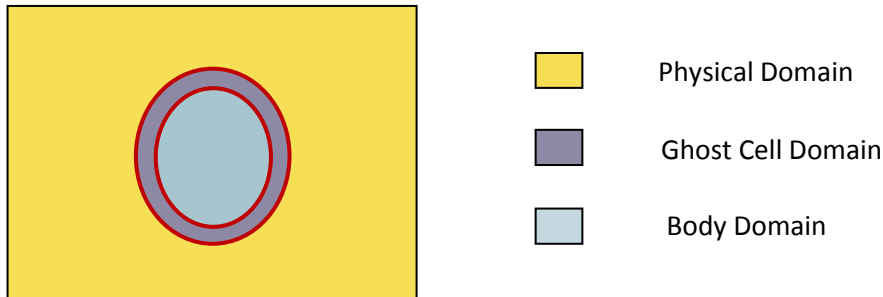


Figure 5.7. Physical domain, ghost cell domain and body domain.

#### 5.4.3.3 Interpolation techniques

The expressions given for the forcing would be correct if the position of the flow variables on the grid coincided with the immersed boundary. This in general is not for complex curvilinear geometries. In particular, in the present case, where a staggered grid is used, even if the boundary coincided with the position where one velocity component was defined, this would not be the case for the other components. Therefore, an interpolation procedure would be needed anyway. For each ghost cell, an interpolation scheme that introduces the boundary condition of the IB is then devised.

A number of options are available for constructing the interpolation scheme (75). The simplest possibility is to select the grid points closest to the immersed boundary and to apply the forcing as if the position of the unknown and the boundary were coincident. In fact, in this case there is no interpolation and the geometry is described in a stepwise way. Note also that the surface is somewhat diffused since the 2 velocity boundary

conditions are applied at different locations. This section studies two of the available interpolation techniques: the Inverse Distance Weighted Method and Linear Interpolation.

#### 5.4.3.3.1 Inverse Distance Weighted Method

The original inverse distance weighted interpolation method is due to Shepard (76). The basic Shepard's method is:

$$f(x, r) = \frac{\sum_{k=1}^N \omega_k(x, r) f_k}{\sum_{k=1}^N \omega_k(x, r)} \quad \text{Eq. 5.42}$$

Where  $\omega_k(x, r) = d_k^\mu = ((x - x_k)^2 + (r - r_k)^2)^\mu$  and  $\mu$  is typically  $-2$ , although other values may be used.  $\mu$  can be also replaced by  $\mu_k$  and could be different for each  $k$ , where  $k$  goes from one to the number of points used to interpolate.

Franke and Little (77, 78) suggested a method which is used extensively in this work where the weighting coefficients are defined as:

$$\omega_k(x, r) = \left( \frac{R - d_k}{R d_k} \right)^\mu \quad \text{Eq. 5.43}$$

where  $R$  represents the maximum  $d_k$ . Eq. 5.43 can be re-written using a dimensionless weighting coefficient

$\hat{\omega}_i = \frac{\omega_i(x, r)}{\sum_{k=1}^N \omega_k(x, r)}$ , so that

$$f(x, r) = \sum_{i=1}^N \hat{\omega}_i(x, r) f_i \quad \text{Eq. 5.44}$$

#### Dirichlet boundary conditions

The boundary condition for the velocity is,

$$\vec{v}^* = \vec{V} \quad \vec{x} \in \partial\Omega \quad \text{Eq. 5.45}$$

Because the sparse structure of the matrix needs to be conserved in order to allow for the efficient numerical solution of the resulting algebraic problem, only the immediate neighbors to the ghost points can be used when interpolating.

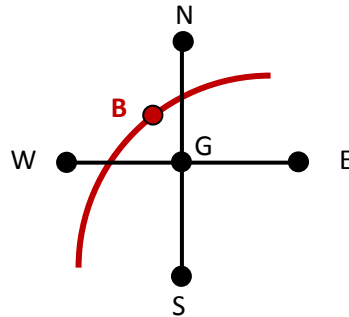


Figure 5.8. Stencil

$$\vec{v}_G^*(x_G, r_G) = \hat{\omega}_w \vec{v}_w^* + \hat{\omega}_N \vec{v}_N^* + \hat{\omega}_B \vec{v}_B + \hat{\omega}_S \vec{v}_S^* + \hat{\omega}_E \vec{v}_E^* \quad \text{Eq. 5.46}$$

At most, two out of four original boundary points lay in the physical domain for the particular case of a circle, thus, Eq. 5.46 is simplified to,

$$\vec{v}_G^*(x_G, r_G) = \hat{\omega}_1 \vec{v}_1^* + \hat{\omega}_2 \vec{v}_2^* + \hat{\omega}_B \vec{V} \quad \text{Eq. 5.47}$$

where 1 represents the node in the  $r$  direction (east or west, depending on the location in the circle) and 2 represents the node in the  $x$  direction (north or south).

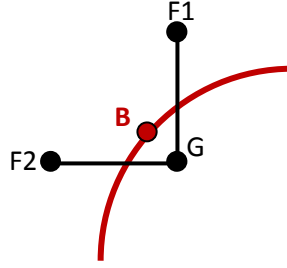


Figure 5.9. Three points interpolation.

This condition can be simply imposed when the viscous terms are calculated implicitly, by substituting in every ghost point the original equation with the boundary equation (Eq. 5.48).

$$-\hat{\omega}_1 \vec{v}_1^* - \hat{\omega}_2 \vec{v}_2^* + \vec{v}_G^*(x_G, r_G) = \hat{\omega}_B \vec{V} \quad \text{Eq. 5.48}$$

### Neumann boundary conditions

To enforce mass conservation, we impose that the normal derivative of the velocity correction is null, this is:

$$\partial_n \phi = 0 \quad \vec{x} \in \partial\Omega \quad \text{Eq. 5.49}$$

This is equivalent to imposing  $\phi_G = \phi_{G^*}$ , where  $G^*$  is the symmetric point in the direction normal to the boundary and it does not have to belong to the mesh. (See Figure 5.10).

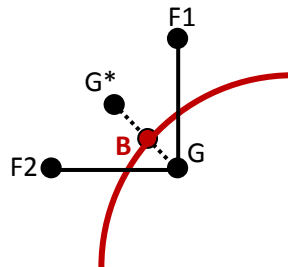


Figure 5.10. Neumann boundary conditions

Following the same procedure that the one described for Dirichlet boundary conditions,

$$\phi_G = \hat{\omega}_1 \phi_1 + \hat{\omega}_2 \phi_2 + \hat{\omega}_{G^*} \phi_{G^*} \quad \text{Eq. 5.50}$$

The boundary equation that is going to replace the Poisson equation in the ghost cells is:

$$-\hat{\omega}_1\phi_1 - \hat{\omega}_2\phi_2 + \phi_G(1 - \hat{\omega}_{G^*}) = 0. \quad \text{Eq. 5.51}$$

This way of imposing the boundary condition for  $\phi$  presents problems at some particular points. When the ghost cell is on the boundary,  $\hat{\omega}_{G^*} \sim 1$ ,  $\hat{\omega}_1 \sim 0$ ,  $\hat{\omega}_2 \sim 0$ , and thus, the boundary condition is  $0=0$  and the matrix becomes singular. By simply forcing  $G^*$  to be separated a certain distance from  $G$ , this problem disappears while keeping the numerical scheme second order. Mathematically, this procedure is expressed as:

$$\begin{aligned} \phi_{G^*} &= \phi_B + (\partial_n \phi)_B d_{BG^*} + \frac{(\partial_n^2 \phi)_B}{2} d_{BG^*}^2 + \dots \\ \phi_G &= \phi_B + (\partial_n \phi)_B d_{BG} + \frac{(\partial_n^2 \phi)_B}{2} d_{BG}^2 + \dots \end{aligned} \quad \text{Eq. 5.52}$$

Thus,

$$\phi_{G^*} - \phi_G = \frac{(\partial_n^2 \phi)_B}{2} (d_{BG^*}^2 - d_{BG}^2) + \dots \quad \text{Eq. 5.53}$$

Since the coefficients introduced in the ghost cell positions are generally much smaller than the ones coming from the discretization of Navier-Stokes equations in the physical domain, it is advisable to multiply the boundary condition equation by  $1/dx^2$  or  $1/dr^2$ , to make sure that all the coefficients in the matrix have the same order of magnitude. If all the terms of the matrix are of the same order of magnitude, we avoid errors due to finite floating point accuracy.

#### 5.4.3.3.2 Linear interpolation

One simple option is bilinear interpolation where a generic flow variable can be expressed with reference to

Figure 5.11 as

$$f(x, r) = C_B + C_1 x + C_2 r + C_3 r x \quad \text{Eq. 5.54}$$

The coefficients  $C_i$  can be expressed in terms of the nodal values

$$C = M^{-1}f \quad \text{Eq. 5.55}$$

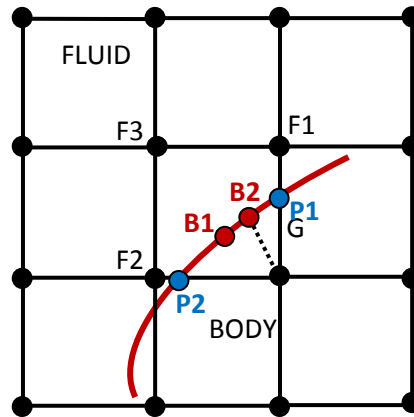


Figure 5.11. Linear interpolation.

The four coefficients in the above equation can be evaluated in terms the values of  $f$  at fluid nodes  $F_1$ ,  $F_2$  and  $F_3$ , and at the boundary point  $B_1$ , which is the half way between points  $P_1$  and  $P_2$ . Alternatively,  $B_2$  can

also be used instead of  $B_1$ . Note that  $P_1$  and  $P_2$  are the intercepts with the  $r$ - and  $x$ - lines passing through the ghost point, respectively.

A less accurate, linear interpolation scheme (i.e.,  $C_3 = 0$ ) would not employ the fluid in node  $F_3$  and therefore would retain sparse form of the matrix, which is well suited for line-solution techniques (71, 79). Linear interpolation preserves the second-order accuracy of the overall numerical scheme. Although polynomials of higher degree are expected to be more accurate, they often lead to boundedness problems and numerical instabilities.

As a staggered grid is being used, different weighted coefficients at the boundary for each velocity component and pressure have to be found. Thus, it is required to solve a different linear system for each variable. The staggered grid arrangement increases the required storage. However, the increase is not significant since the boundary has one less dimension than the domain.

### Dirichlet boundary conditions

A certain velocity needs to be specified at the boundary using a three points linear interpolator, so

$$v(x, r) = C_B + C_1 r + C_2 x \quad \text{Eq. 5.56}$$

Following the notation specified in 5.4.3.3.2,  $M$  can be defined as a 3x3 matrix whose elements can be computed from the coordinates of the three points.

$$M = \begin{bmatrix} 1 & r_B & x_B \\ 1 & r_1 & x_1 \\ 1 & r_2 & x_2 \end{bmatrix} \quad \text{Eq. 5.57}$$

The coefficients  $C_i$  can then be calculated as  $C = M^{-1}f$ . It is convenient to evaluate the matrices  $M$  at each point initially and store them for its usage during the solution procedure if the boundaries are not moving. If the boundaries are moving,  $M$  needs to be recalculated at every time step. The value of  $f$  in the ghost points can now be interpolated as function of  $C_i$  and the location of the ghost point.

$$\vec{v}_G^*(x_G, r_G) = \hat{\omega}_1(C_i, x, r) \vec{v}_1^* + \hat{\omega}_2(C_i, x, r) \vec{v}_2^* + \hat{\omega}_B(C_i, x, r) \vec{V} \quad \text{Eq. 5.58}$$

The major drawback with this interpolation is that large negative weighting coefficients are encountered when the boundary point is close to one of the fluid nodes. Although algebraically correct, this can lead to numerical instability, i.e., the absolute value at the ghost point may be greater than the nearby fluid point values and the solution may not converge. A way to remedy this difficulty is to use the image of the ghost node inside the flow domain to ensure positive weighting coefficients. The point  $G^*$  is the image of the ghost node  $G$  through the boundary as shown in Figure 5.10. The variable is evaluated at the image point using the interpolation scheme. The value at the ghost node is then  $f_G = 2f_B - f_{G^*}$ . (79)

### Neumann boundary conditions

The pressure correction boundary condition requires the wall normal derivative to be zero at the boundary. The normal derivative on the boundary can be decomposed as:

$$\partial_n \phi = \partial_x \phi \hat{n}_x + \partial_r \phi \hat{n}_r = 0 \quad \vec{x} \in \partial\Omega \quad \text{Eq. 5.59}$$

where  $\hat{n}_{x,r}$  are the components of the unit vector normal to the boundary. Since they are known, the computation of the normal gradient at any point is straightforward, using the matrix  $M$  is defined as:

$$M = \begin{bmatrix} 0 & \sin(\theta_B) & \cos(\theta_B) \\ 1 & r_1 & x_1 \\ 1 & r_2 & x_2 \end{bmatrix} \quad \text{Eq. 5.60}$$

So the linear system that provides the coefficients  $C_i$  is,

$$\begin{bmatrix} C_B \\ C_1 \\ C_2 \end{bmatrix} = \begin{bmatrix} 0 & \sin(\theta_B) & \cos(\theta_B) \\ 1 & r_1 & x_1 \\ 1 & r_2 & x_2 \end{bmatrix}^{-1} \begin{bmatrix} \partial_n \phi_B \\ \phi_1 \\ \phi_2 \end{bmatrix} \quad \text{Eq. 5.61}$$

The pressure correction can be now imposed at the boundary points as a function of geometrical parameters.

$$\phi_G(x, r) = \hat{\omega}_1(C_i, x, r)\phi_1 + \hat{\omega}_2(C_i, x, r)\phi_2 + \hat{\omega}_B(C_i, x, r)\partial_n \phi_B; \quad i = 1, 2, B \quad \text{Eq. 5.62}$$

#### 5.4.3.3 Internal treatment of the body

For the internal treatment of the body there are several possibilities but the external flow is essentially independent of the internal conditions. A first possibility is to apply the forcing inside the body without any smoothing. This is equivalent to imposing the velocity distribution inside the body with the pressure that adjusts accordingly. An alternate approach consists of leaving the interior of the body free to develop a flow without imposing any condition. In this case the flow pattern inside the body will be different from the previous case, but this internal flow pattern is irrelevant and the external flow is unchanged.

#### 5.4.4 Properties of the numerical scheme

The solution method should have certain properties. The most important ones are summarized below.

##### 5.4.4.1 Consistency

The discretization should become exact as the grid spacing tends to zero. The difference between the discretized equation and the exact one is called the truncation error. For a method to be consistent, the truncation error must become zero when the mesh spacing  $\Delta t \rightarrow 0$  and/or  $\Delta x, \Delta r \rightarrow 0$ . Even if the approximations are consistent, it does not necessarily mean that the solution will become the exact solution of the differential equation.

##### 5.4.4.2 Stability

A numerical solution method is said to be stable if it does not magnify the errors that appear in the course of the numerical solution process.

##### 5.4.4.3 Convergence

A numerical method is said to be convergent if the solution of the discretized equations tends to the exact solutions of the differential equations as the grid spacing tends to zero.

For non-linear problems stability and convergence are difficult to demonstrate. Therefore convergence is usually checked using numerical experiments. Section 5.6 presents some examples that validate the code and demonstrate its convergence.

## 5.5 Solution of the algebraic system of equations

### 5.5.1 Introduction

The potential correction and the implicit discretization of the viscosity terms require linear systems to be solved every time step. If the immersed boundaries are neglected and the time step is constant, neither the geometry nor discretization change with time and, thus, the corresponding system matrices remains the same throughout the whole time course of the simulation. This means that all matrices can be constructed in an initialization step. However, since the time step is different at each step, to improve convergence, certain terms of the matrices need to be changed. In addition, the presence of moving immersed boundaries involves changes every step. The current code computes matrices and modifications due to immersed boundaries at each time step, although an improvement is possible if the portion of the problem that does not experience any change is defined at the beginning instead of every step.

As outlined before, the result of the discretization process is a system of linear algebraic equations. An efficient method for solving linear systems of algebraic equations is thus needed. The matrices derived from partial differential equations are always sparse, i.e. most of their elements are zero. All of the non-zero elements of the matrices are on a small number of well defined diagonals (Figure 5.12). Taking advantage of this property, one can greatly simplify the task of solving the system. The matrix that defines the system to solve has the structure presented in Figure 5.12, where the brown and orange diagonals, which correspond to the derivatives in the  $r$  direction, are separated  $nx$  positions from the main diagonal (yellow).

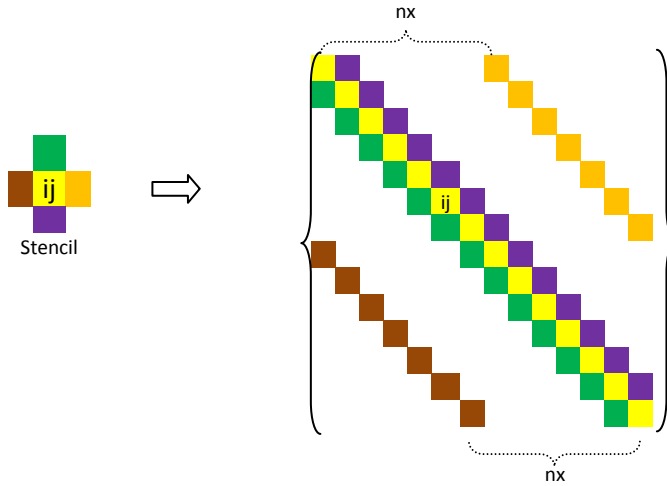


Figure 5.12. Matrix structure

The matrices act on the corresponding field quantities  $u_x$ ,  $u_r$  and the correction  $\phi$ . Pressure by itself is not defined. What affect the fluid are the pressure gradients. Thus, the matrix operator action on  $\phi$  has to be modified so that it becomes regular, while still yielding a correct solution for the pressure. This is achieved by adding 1 to the last entry. The proof is as follows.

Let  $\vec{\omega} = (0, \dots, 0, 1)^T$ . Thus  $\vec{\omega}\vec{\omega}^T$  is a matrix with its only nonzero entry being a 1 in the last position. Let  $A$  be the Neumann-Poisson matrix, i.e.  $A\vec{e} = 0$ . The new modified Poisson matrix is  $B = A + \vec{\omega}\vec{\omega}^T$ . Let  $\vec{u}$  be an arbitrary vector. Then,



$$B\vec{u} = \underbrace{A\vec{u}}_{\perp \vec{e}} + (\vec{\omega}^T \vec{u}) \underbrace{\vec{\omega}}_{\text{no } \perp \vec{e}}. \quad \text{Eq. 5.63}$$

This sum can only equal 0 if  $\vec{u} = 0$ . Hence B has full rank. It remains to show that for any right hand side  $\vec{b}$ , which is admissible (i.e.  $\vec{b} \perp \vec{e}$ ), the solution to  $B\vec{u} = \vec{b}$  satisfies  $A\vec{u} = \vec{b}$ . First note that due to Eq. 5.63,  $B^{-1}\vec{\omega} = \vec{e}$ . Hence,

$$AB^{-1} = (B - \vec{\omega}\vec{\omega}^T)B^{-1} = I - \vec{\omega}\vec{\omega}^TB^{-1} = I - \vec{\omega}\vec{e}^T \quad \text{Eq. 5.64}$$

And consequently  $AB^{-1}\vec{b} = \vec{b}$ .

A system of equations can be solved following two possible families of techniques:

- **Direct methods:** attempt to solve the problem by a finite sequence of operations, and, in the absence of rounding errors, would deliver an exact solution
- **Iterative methods:** attempt to solve a problem by finding successive approximations to the solution starting from an initial guess.

Iterative methods are usually the only choice for nonlinear equations. However, iterative methods are often useful even for linear problems involving a large number of variables, where direct methods would be prohibitively expensive. The long term objective is the implementation of a multigrid method that will be based on the iterative methods here analyzed. The development of such method is quite involved, specially in conjunction with immersed boundaries, and will not be done here. The scope of this project is not developing a multigrid method but defining and evaluating the iterative methods that will be implemented in the future in this multigrid scheme.

The aim of this section is to present how different solvers behave when trying to find the solution of the discretized equations set out in section 5.4. First of all, the basic characteristics of the most commonly used direct solvers are described. Then, a set of iterative solvers based on Gauss Seidel methods are presented and evaluated. Furthermore, the possibility of taking advantage in terms of storage of the sparse structure of the matrix and the possibility of using more complex iterative methods (Krylov subspace methods) will be analyzed. A brief introduction of what a multigrid method is will finish with the descriptive part to start a quantitative evaluation of the implemented solvers.

## 5.5.2 Direct methods

### 5.5.2.1 Gauss elimination

Gauss elimination is the basic method for solving linear systems of algebraic equations. Two steps can be clearly distinguished. First of all, the original matrix should be transformed into an upper triangular matrix by forward elimination. Then, the upper triangular system of equations resulting from forward elimination can be easily solved.

The number of operations required to solve a linear system of n equations by Gauss elimination is proportional to  $n^3/3$ . The bulk of this effort is in the forward elimination phase. The back substitution requires only  $n^2/2$  arithmetic operations and is much less costly than the forward eliminations. The extremely high cost of this method warrants the search for more efficient special solver for matrices, such as the sparse ones arising from the discretization of differential equations. In addition, Gauss elimination does not vectorize or parallelize well, which constitutes a strong limitation.

### 5.5.2.2 Lu decomposition

LU decomposition has its fundamentals in Gauss elimination. Any matrix  $A$ , subject to some generic limitations that can be ignored here, can be factored into the product of lower ( $L$ ) and upper ( $U$ ) triangular matrix ( $A=LU$ ). The existence of this factorization allows the solution of the system of equations in two stages:

$$Ax = b \rightarrow Ux = y \quad Ly = b \quad \text{Eq. 5.65}$$

The advantage of LU factorization over Gauss elimination is that the factorization can be performed without knowing the forced terms. As a result, if many systems involving the same matrix are to be solved, considerable savings can be obtained by performing the factorization first.

### 5.5.3 Iterative methods

The high accuracy provided by direct methods in exchange for their cost is normally not needed because the discretization error is usually much larger than the accuracy of computer arithmetic. A numerical just somewhat more accurate than the discretization suffices.

In an iterative method, one guesses a solution, and uses the equation to systematically improve it. If each iteration is cheap and the number of iterations is small, an iterative solver will cost less than a direct method.

A set of splitting methods are going to be implemented, where the matrix  $A$  is split in two parts such that  $A=M+N$ . Rewriting  $Ax=b$  as  $Mx=-Nx+b$ , the following iterative algorithm is proposed:

$$Mx^{k+1} = -Nx^k + b \quad \text{Eq. 5.66}$$

The task at hand is thus to select the splitting  $A=M+N$  such that converges to the desired tolerance in a small number of iterations  $k$  while the matrix  $M$  is such that is relatively easy to solve. Various choices for this splitting are discussed below, based on the simple partitioning of  $A$  defined such that  $A=L+D+U$ , where  $L$  is strictly lower triangular,  $D$  is diagonal, and  $U$  is strictly upper triangular.

#### 5.5.3.1 Methods analyzed in this study

##### 5.5.3.1.1 Jacobi

The Jacobi method takes  $M_J=D$  and  $N_J=U+L$ , resulting in:

$$x^{k+1} = D^{-1}[-(L + U)x^k + b] \quad \text{Eq. 5.67}$$

As  $D$  is a diagonal matrix,  $D^{-1}$  is trivial to compute. The convergence is guaranteed if  $A$  is diagonally dominant. However, for the typical high dimensional linear equations of interest for splitting methods, convergence of Jacobi method is unacceptably slow so this method is not going to be implemented.

##### 5.5.3.1.2 Gauss Seidel

The Gauss-Seidel method (GS) takes  $M_{GS}=D+L$  and  $N_{GS}=U$  resulting in Eq. 5.68 which may be solved at each iteration by back substitution.

$$x^{k+1} = (D + L)^{-1}[-Ux^k + b] \quad \text{Eq. 5.68}$$

Again, if  $A$  is diagonally dominant convergence is guaranteed. Since larger portion of the system is included into the implicit part ( $M_{GS}$ ) convergence is generally faster following the GS approach than the Jacobi approach.

Convergence of the plain GS method described here is still, in general, unacceptably slow for it to be of practical use as is. Nonetheless, when implemented properly it forms the foundation for the most efficient techniques available for solving large linear systems derived from elliptic PDEs, as it will be studied later (Sections 5.5.4.1).

#### 5.5.3.1.3 Successive Overrelaxation (SOR)

The SOR method is an iterative method based on the GS approach with  $M_{SOR}=D+L$  and  $N_{SOR}=U$ , written in the form:

$$\mathbf{x}^{k+1} = \mathbf{x}^k + w(\mathbf{x}^{k+1} - \mathbf{x}^k) \quad \text{Eq. 5.69}$$

Thus,

$$(D + L)\mathbf{x}^{k+1} = ((1 - w)D + (1 - w)L - wU)\mathbf{x}^k + wb \quad \text{Eq. 5.70}$$

for some relaxation parameter  $w \in (0,2)$ . Doing that, the convergence can be accelerated significantly. Generally, the larger the grid the larger the optimum over-relaxation factor. For values of  $w$  less than the optimum, the convergence is monotonic and the rate of convergence increases as  $w$  increases. When  $w$  is exceeded, the convergence rate deteriorates and the convergence is oscillatory. When the optimal over-relaxation factor is used, the number of iterations is proportional to the number of grid points in one direction, reaching a substantial improvement.

#### 5.5.3.1.4 Red/Black Gauss Seidel

As it has been outlined before, as the origin of the system to solve comes from a cell centered finite differences discretization, all of the non-zero elements of the matrices then lie on a small number of well defined diagonals (See Figure 5.12). Choosing the appropriate mesh size,  $A$  is checkerboard (thus,  $a_{ij}=0$  when  $i+j=\text{even}$  and  $i \neq j$ ) and the problem can be reordered in a particularly attractive structure for the application of Gauss-Seidel iterations shown in Figure 5.13.

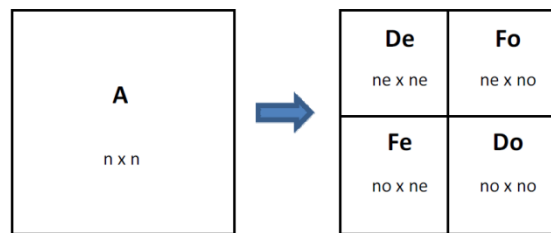


Figure 5.13. Re-ordered matrix

Where  $n$  is the dimension of the linear system,  $ne$  the number of even elements and  $no$  the number of odd elements.  $De$  and  $Do$  are diagonal matrices that contain the elements of the main diagonal of  $A$ .  $Fe$  and  $Fo$  contain the rest of the terms of  $A$ . The problem to solve now can be presented as it is shown in Eq. 5.71.

$$\begin{bmatrix} De & Fo \\ Fe & Do \end{bmatrix} \begin{bmatrix} xe \\ xo \end{bmatrix} = \begin{bmatrix} be \\ bo \end{bmatrix} \quad \text{Eq. 5.71}$$

Application of the Gauss Seidel method to this permuted checkerboard system, taking

$$M_{RB} = \begin{bmatrix} D_e & 0 \\ F_e & D_o \end{bmatrix} \text{ and } N_{RB} = \begin{bmatrix} 0 & F_o \\ 0 & 0 \end{bmatrix} \quad \text{Eq. 5.72}$$

yields to an iterative method that can be written as the repeated application of two distinct sub-steps that are symmetric in the even and odd variables.

$$D_e \mathbf{x}_e^{k+1} = -F_o \mathbf{x}_o^k + b_e \rightarrow \text{Sub-step 1: } \mathbf{x}_e^{k+1} = D_e^{-1}(-F_o \mathbf{x}_o^k + b_e) \quad \text{Eq. 5.73}$$

$$D_o \mathbf{x}_o^{k+1} = -F_e \mathbf{x}_e^k + b_o \rightarrow \text{Sub-step 2: } \mathbf{x}_o^{k+1} = D_o^{-1}(-F_e \mathbf{x}_e^k + b_o) \quad \text{Eq. 5.74}$$

The alternate application of the Jacobi method to the two sets of nodes gives an overall method with the same convergence properties as the Gauss Seidel. The nice feature of the Red-Black Gauss-Seidel solver is that it vectorizes and parallelizes well, since there are interdependencies in either sub-step. Thus, unlike the Gauss-Seidel method, as during each of its two sub-steps the calculations are decoupled, they may be performed in any order.

The solver to implement will be used in three different cases during the calculation process:

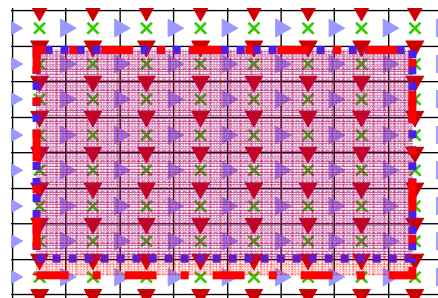
- Calculation of the viscous terms in the x direction.
- Calculation of the viscous terms in the r direction.
- Calculation of the potential correction.

Because a staggered matrix is being used, in each of these sections the dimension of the system to solve is slightly different.

Table 5.4. Dimensions

Step	Mesh dimension	System dimension	n	nx*	nr*
Viscous terms x	nx - 1, nr	(nx - 1)nr, (nx - 1)nr	(nx - 1)nr	nx-1	nr
Viscous terms r	nx, nr-1	nx(nr-1), nx(nr-1)	nx(nr-1)	nx	nr-1
Potential correction	nx,nr	nxnr,nxnr	nxnr	nx	nr

In order to apply this method,  $a_{ij}=0$  when  $i+j=\text{even}$  and  $i \neq j$ . As it can be seen in Figure 5.12, for each row  $i$ , only the elements  $a_{i,j-nx^*}$ ,  $a_{i-1,j}$ ,  $a_{i,j}$ ,  $a_{i+1,j}$  and  $a_{i+nx^*,j}$  are different from zero. Thus, the checkerboard structure of the matrix will be guaranteed if  $nx^*$  is an odd number. This purpose can be easily achieved if a new row is added to the original staggered structure when defining the velocities in the x direction imposing the appropriate boundary conditions (see Figure 5.14).



Former mesh limits

New mesh limits

Figure 5.14. Mesh re-definition

The new dimensions of the computational domains are the ones defined Table 5.5. In order to achieve a checkerboard structure is enough with assuring that the main dimension ( $nx$ ) is an odd number.

Table 5.5. New dimensions compatible with checkerboard structure

Step	Mesh dimension	System dimension	$n$	$nx^*$	$nr^*$
<b>viscux</b>	$nx, nr$	$nxnr, nxnr$	$nxnr$	$nx$	$nr$
<b>viscur</b>	$nx, nr-1$	$nx(nr-1), nx(nr-1)$	$nx(nr-1)$	$nx$	$nr-1$
<b>press</b>	$nx, nr$	$nxnr, nxnr$	$nxnr$	$nx$	$nr$

Figure 5.15 shows the matrix structure before and after ordering it. As the matrix is sparse, it is important to take into account that many of the elements of  $Fe$  and  $Fo$  are zero, and special care should be taken when defining the code to achieve an efficient computation.

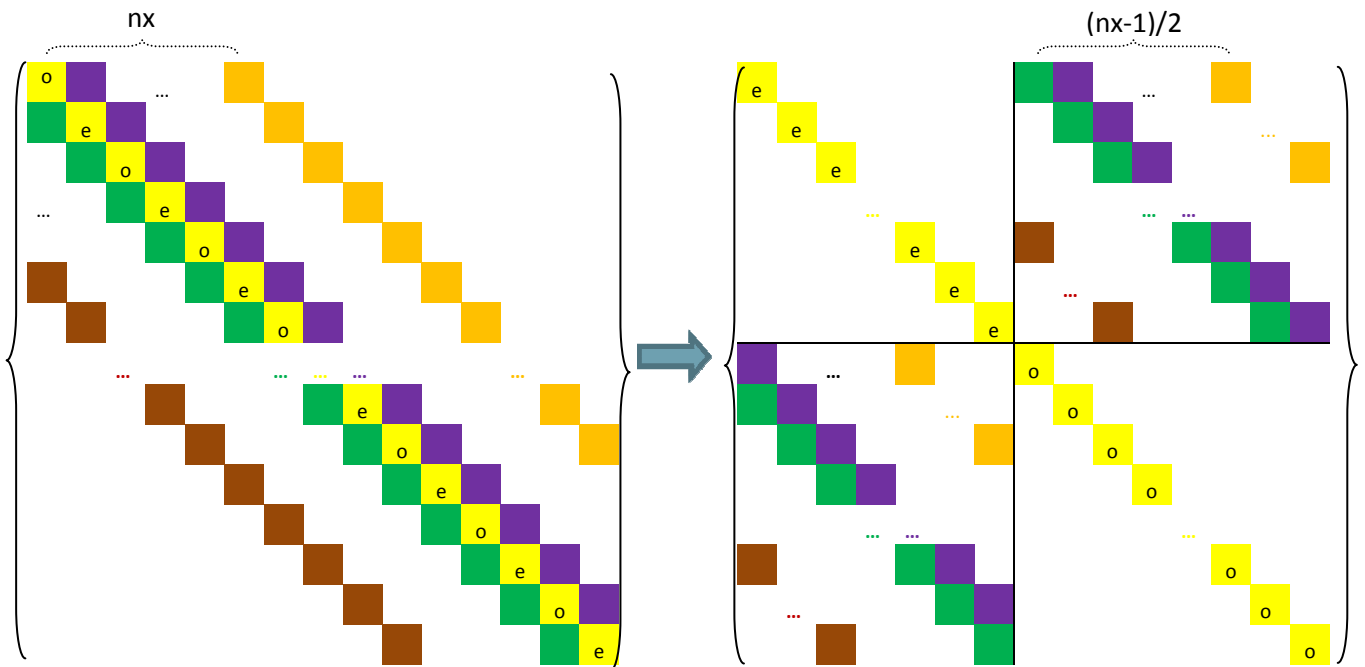


Figure 5.15. Matrix re-order

Note that it is also possible to implement the algorithm without performing this redefinition in the original operators. Though the system is considered in a reordered form in the conceptualization of the scheme, the system does not actually need to be reordered to apply the two step procedure that implements it reducing considerably the computational cost.

#### 5.5.3.1.5 Convergence criteria and iteration errors

When using iterative solvers, it is important to know when to quit. The most common procedure is based on the difference between two successive iterations. The procedure is stopped when the difference, measured by some norm, is less than a pre-selected value. This difference may be small when the error is not small so that a proper normalization is essential.

The convergence criteria presented here is based on the residual defined as,

$$r = b - Ax$$

Eq. 5.75

One termination criterion (being  $\tau$  the accepted tolerance) is,

$$\frac{\|r_k\|}{\|r_0\|} \leq \tau \quad \text{Eq. 5.76}$$

which can be related to the error (Eq. 5.77),

$$e = x - x^* \quad \text{Eq. 5.77}$$

in terms of the condition number  $k(A)$  :

$$\frac{\|e\|}{\|e_0\|} \leq k(A) \frac{\|r\|}{\|r_0\|}. \quad \text{Eq. 5.78}$$

It could be possible to establish a convergence criterion based on the error instead of the residual. As the condition number of the matrices to deal with can be small, a criteria based on the residual will provide a more realistic measure of solver accuracy.

The termination criterion (Eq. 5.76) depends on the initial value and may result in unnecessary work when the initial guess is good and a poor result when the initial iterate is far from the solution. For this reason, the following iteration criterion can be redefined as:

$$\frac{\|r_k\|}{\|b\|} \leq \tau \quad \text{Eq. 5.79}$$

Eq. 5.76 and Eq. 5.79 are the same when  $x_0=0$ , which is a common choice.

The problem arises when the solution ( $x$ ) is a small value compared to the forcing term  $b$ . Then, the criterion defined in Eq. 5.79 could be not good enough to determine the level of accuracy, replacing the previous expression by the one presented in Eq. 5.80. This criterion involves additional computation that will be deeply studied in section 5.5.4.1.

$$\frac{\|r_k\|}{\|x_k\|} = \tau \quad \text{Eq. 5.80}$$

#### 5.5.3.1.6 Comparative analysis of iterative methods

This section shows the convergence features of the proposed iterative methods (Gauss Seidel (GS), Successive Over-relaxation (SOR) and Red/Black Gauss Seidel (RB) as function of the number of iterations. Further analysis will be performed in section 5.5.4.1, comparing the performance of direct and iterative methods as a function of multiple variables. Table 5.6 presents predictions for the order of magnitude of the number of iterations corresponding to each method.

Table 5.6. Estimated number of iterations as function of the mesh dimension

Method	Number of iterations
GS	$nx^2/2$
SOR	$nx$
RB	$nx^2/2$

Evaluating the iterative solvers for different mesh sizes and defining the error as:

$$err = \frac{\|Ax - b\|_2}{\|x\|_2} \quad \text{Eq. 5.81}$$

The number of iterations required to achieve an error of  $10^{-2}$  are the ones presented on Table 5.7.

Table 5.7. Number of iterations required to achieve  $err < 10^{-2}$

Mesh size	Iterative Method		
	RB	GS	SOR
7x7	425	386	55
27x27	8580	7766	1600
47x47	28844	25459	4927
67x67	40155	29936	3658

Figure 5.16 shows how the actual number of iterations is much higher than the predictions (dotted lines) because the system to be solved is bad conditioned. Even though, it can be appreciated how GS and RB have similar convergence features while SOR requires a considerable lower amount of iterations to achieve the solution and these convergence features are proportional to the expected ones.

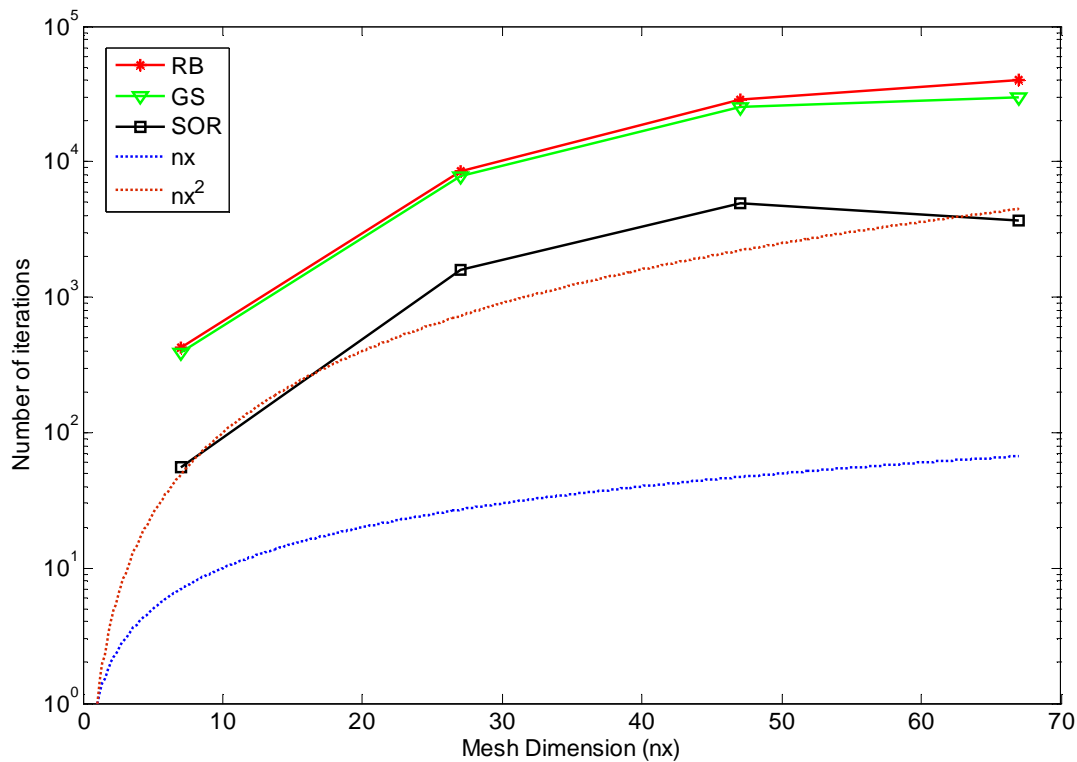


Figure 5.16. Number of iterations as function of the mesh dimension (Simulation6)

It is also interesting to point out how the SOR requires less iteration for a 73x73 mesh than for a 43x43. This effect can be explained by considering the dependence of the optimum over-relaxation factor with the mesh size. The simulations here have been performed for a fixed over-relaxation factor of  $w=1.7$  which leads in a more efficient way the solution for higher mesh sizes. Finally, Figure 5.17 shows the evolution of the error for a fixed mesh of dimension 73x73 for the three analyzed methods.

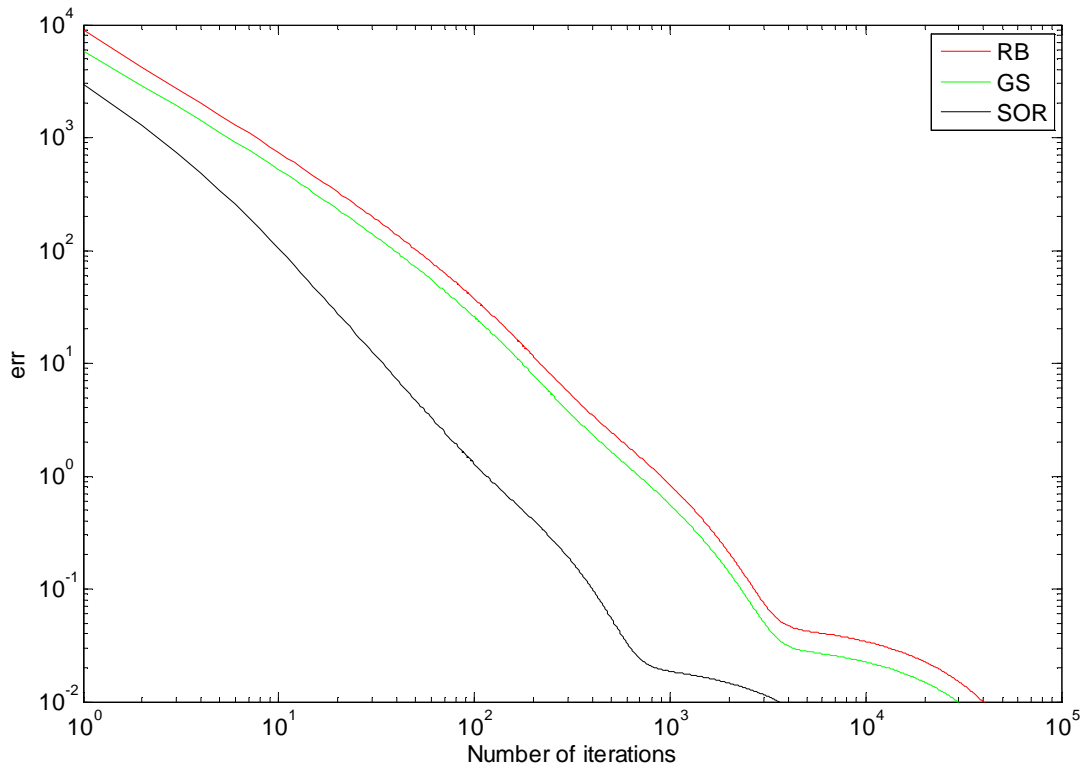


Figure 5.17. Variation of error with the iterations for a 73x73 mesh

### 5.5.3.2 Sparse Iterative Methods

When storing and manipulating sparse matrices on a computer, it is convenient and often necessary to use specialized algorithms and data structures that take advantage of the sparse structure of the matrix. Data is easily compressed, and this compression results in significantly less computer data storage usage and lower times required to access the data in the memory of the computer.

FORTTRAN provides a library for working with sparse matrices which is called SPARSEKIT. It includes general sparse matrix manipulation routines as well as a few iterative solvers. It allows the use of preconditioners base on LU factorization, which will solve the problem shown in Figure 5.16 of requiring a huge number of iterations to achieve the solution. It provides basic iterative solver such as CG (Conjugate Gradient Method), FOM (Full Orthogonalization method) or GMRES (Generalized Minimum Residual Method). Most of these iterative methods are Krylov subspace methods and they are among the most successful methods currently available in numerical linear algebra.

Krylov subspace methods work by forming an orthogonal basis of the sequence of successive matrix powers times the initial residual. The Krylov sequence generated by an  $n$ -by- $n$  matrix  $A$  and a vector  $b$  of dimension  $n$  is the linear subspace spanned by the images of  $b$  under the first  $r$  powers of  $A$  (starting from  $A^0 = I$ ),

$$\mathcal{K}_r(A, b) = \text{span}\{b, Ab, A^2b, \dots, A^{r-1}b\} \quad \text{Eq. 5.82}$$

Starting with a vector,  $b$ , one computes  $Ab$ , then one multiplies that vector by  $A$  to find  $A^2b$  and so on. Thus, these algorithms avoid matrix-matrix operations, but rather multiply vectors by the matrix and work with the resulting vectors.



Because the vectors tend very quickly to become almost linearly dependent, methods relying on Krylov subspace frequently involve some orthogonalization scheme, such as Lanczos iteration for Hermitian matrices or Arnoldi iteration for more general matrices.

### 5.5.3.3 Multigrid

The basis for the multigrid method is the convergence behavior of iterative methods. Some of these methods produce errors that are smooth functions of the spatial coordinates. After a few iterations, the rapidly varying components of the error have been removed and the error becomes a smooth function of the spatial coordinates. If the error is smooth, the update can be computed on a coarser grid, which means lower computing cost and faster convergence. This suggests that much of the work can be done on coarser grids. Thus, multigrid is a solution method for linear systems based on restricting and extrapolating solutions between a series of nested grids as the ones presented in Figure 5.18.

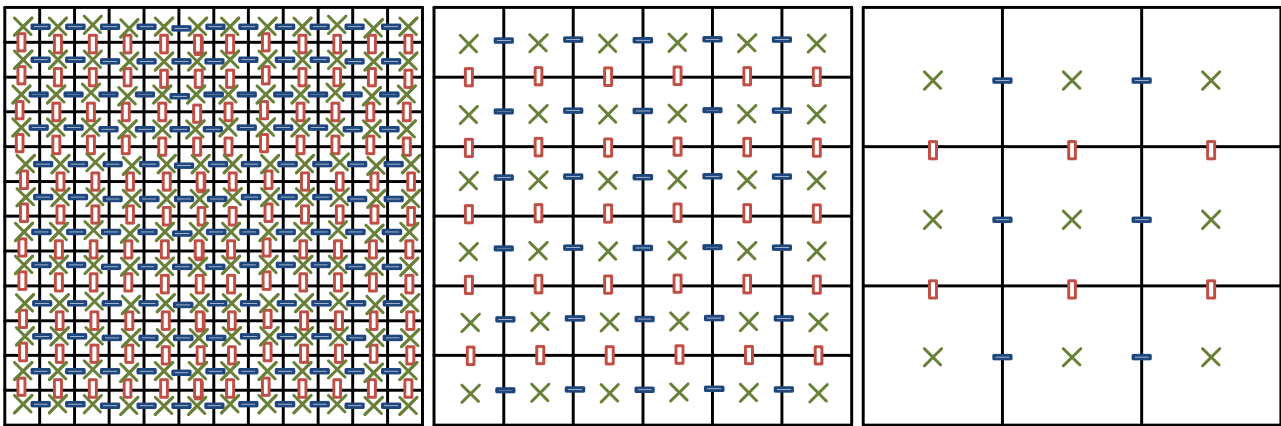


Figure 5.18. Series of nested grids to apply multigrid method

There are many variations of multigrid algorithms, but the important steps to perform among the levels of the multigrid scheme are:

- **Smoothing.** Performs a few iterations with a method that gives a smooth error on the fine grid, reducing high frequency errors.
- **Restriction.** Restricts the residual to a coarser grid and performs iterations of the correction equation on the coarser grid.
- **Interpolation or Prolongation.** Interpolates a correction computed on a coarser grid into a finer grid.

When designing a multigrid method there are many parameters that can be selected more or less arbitrarily: the number of successively coarser grids, the smoothing kernel, the number of iterations on each grid, the order in which the various grids are visited, and the restriction and interpolation schemes are the most important of these. The rate of convergence does, of course, depend on the choices made but the range of performance between the worst and the best methods is probably less than a factor of two (71).

The iterative methods proposed in section 5.5.3 are completely compatible with this multigrid philosophy achieving a much better performance. Other methods such as Strongly Implicit Procedure (SIP), Alternating Direction Implicit method (ADI) or Conjugate Gradient methods can be also implemented in a multigrid scheme(80, 81). Although these methods usually reach the solution with lower amount of iterations they

require more complex and costly operations. For example, SIP requires computing an incomplete LU factorization which is an expensive operation. Conjugate Gradient methods are originally thought to solve symmetric systems of equations so the implementation of the problem studied here could involve some problems. In addition, it is important to keep in mind that the solver should be compatible with the existence of immersed boundaries which makes the problem more complex.

#### 5.5.4 Quantitative analysis

After describing the differences, advantages and disadvantages of direct and indirect methods, it is possible to perform a proper comparative evaluation of the methods. First, the direct method provided by LAPACK package will be tested against the iterative methods described in section 5.5.3. It will be shown that these methods are not a valid alternative without further improvements. That is why a set of Sparse Iterative Methods provided by SPARSEKIT package are tested and shown to be the best alternative to solve the system of algebraic equations.

Table 5.8. Methods compared in the quantitative analysis

DIRECT METHODS	ITERATIVE METHODS
<p style="text-align: center;"><b>LAPACK</b></p>	<p style="text-align: center;"><b>TRADITIONAL ITERATIVE METHODS</b></p> <ul style="list-style-type: none"> <li>- Gauss Seidel (GS)</li> <li>- Red Black (RB)</li> <li>- Successive Over Relaxation (SOR)</li> </ul> <p style="text-align: center;"><b>SPARSE ITERATIVE METHODS. SPARSEKIT</b></p> <ul style="list-style-type: none"> <li>- GMRES (Krylov subspace method)</li> </ul>

##### 5.5.4.1 Direct Methods versus Traditional Iterative Methods

###### 5.5.4.1.1 Introduction

This section compares the solution and the computational cost of the direct solution achieved by the LAPACK package and the solution achieved by traditional iterative methods, when those methods are applied to solve the Poisson equation that calculates the potential function which corrects the velocities to assure continuity.

LAPACK is a set of routines for solving linear equations systems written in Fortran90. The same package includes routines to solve least-squares solutions of linear systems of equations, eigenvalue problems, and singular value problems. Dense and banded matrices are handled by this package, but not general sparse matrices. In all areas, similar functionality is provided for real and complex matrices, in both single and double precision. There are multiple on-line resources which allow an easy management and outstanding of LAPACK routines as the one provided by the University of Colorado, Department of Computers Science (82). Although these routines have been implemented in a highly efficient way, they are not designed to solve a sparse problem such as the present one so further improvement is required.

**Linear Equation Driver Routines**

**Precision**

☐ Real, Single

☐ Complex, Single

☒ Real, Double

☐ Complex, Double

Precision Help

**Dependencies**

☒ With Dependencies

☐ Without Dependencies

Dependencies Help

**Driver Type**

☒ Simple

☐ Expert

Driver Type Help

**Matrix & Storage Type**

☒ General

☐ Band

☐ Tridiagonal

☐ Symmetric/Hermitian Positive Definite

☐ Packed

☐ Band

☐ Tridiagonal

☐ Symmetric/Hermitian Indefinite

☐ Packed

☐ Complex Symmetric

☐ Packed

Storage Type Help

**Selected Routine**

DGESV

See Code

Problem Definition

Reset Back

Figure 5.19. Searching engine for LAPACK subroutines,(82)

Gauss Seidel, Successive Over-Relaxation and Red/Black Gauss Seidel are the chosen iterative methods to be compared with the LAPACK solver. When programming these iterative methods, the sparse structure of the matrix is taken into account in order to avoid unnecessary operations but it is not taken into account in terms of storage. In other words, all the elements of the matrices have been stored but only the non-zero operations have been performed. It is important to keep in mind that the long term aim is to establish a multigrid method based on the presented iterative methods. Thus, although in the current state LAPACK seems to be a competitive alternative, the implementation of multigrid will involve a great improvement of the iterative methods.

#### 5.5.4.1.2 Comparison

The elapsed time is the time required by the CPU to perform the operations and it is the parameter that will be compared to evaluate the solvers. The results presented on Table 5.9 are obtained performing simulations for different mesh sizes.

Table 5.9. Elapsed time in seconds required by each solver for different mesh dimensions

Mesh size	System dimension	LP (s)	RB (s)	GS (s)	SOR (s)
17x17	289x289	0	0,54	0,47	0,37
27x27	729x729	0.05	4,61	4,14	1,13
37x37	1369x1369	0.22	40,99	37,62	7,30
47x47	2209x2209	0.78	168,77	149,38	29,27
57x57	3249x3249	2.35	265,08	156,77	7,81
67x67	4489x4489	5.46	993,26	735,30	90,67

Looking at these data, the iterative methods have an unacceptably slow behavior.

The operations performed by the iterative methods can be divided in two groups:

- Actual iteration, following the method that correspond to each solver, this is, Gauss Seidel, SOR or Red/Black Gauss Seidel.
- Computation of the error, defined as  $\frac{\|Ax^k - b\|_2}{\|x^k\|_2}$ .

Thus, the total time required by the iterative solver can be expressed as:

$$\text{Total Time} = \text{Iteration time} + \text{Error computation time} \quad \text{Eq. 5.83}$$

As shown in Table 5.9, most of the computational time is actually invested on the error calculation (see Table 5.10)

Table 5.10. Elapsed time and error calculation time for different system dimension (n)

n	RB		GS		SOR	
	Total time	Error time	Total time	Error time	Total time	Error time
289	0,54	0,19	0,47	0,13	0,37	0,03
729	4,61	4,14	4,14	3,75	1,13	0,77
1369	40,99	39,89	37,62	36,68	7,30	6,85
2209	168,77	167,37	149,38	147,08	29,27	28,48
3249	265,08	261,32	156,77	154,90	7,81	7,38
4489	993,26	985,77	735,30	729,37	90,67	89,48

Thus, the convergence criteria for the iterative method should be improved in order to obtain a criterion which consumes fewer resources. In addition, it is not required to calculate the error every single iteration. It could be done every certain amount of iterations reaching a substantial acceleration of the code.

Plotting the time that the solver is solving the linear system, this is, subtracting the time to calculate the error (Figure 5.20), it is easy to appreciate how when increasing the dimensions of the mesh, the difference between using an iterative method and a direct method start to decrease. In fact, for larger mesh sizes the iterative method will provide the solution faster with an acceptable level of accuracy. When introducing these iterative methods in a multigrid structure the problem will converge even faster, rendering the option of a direct method complete senseless. Remind that only the iteration time is taken into account here, so developing an efficient convergence criteria is a key point to reach significant results.

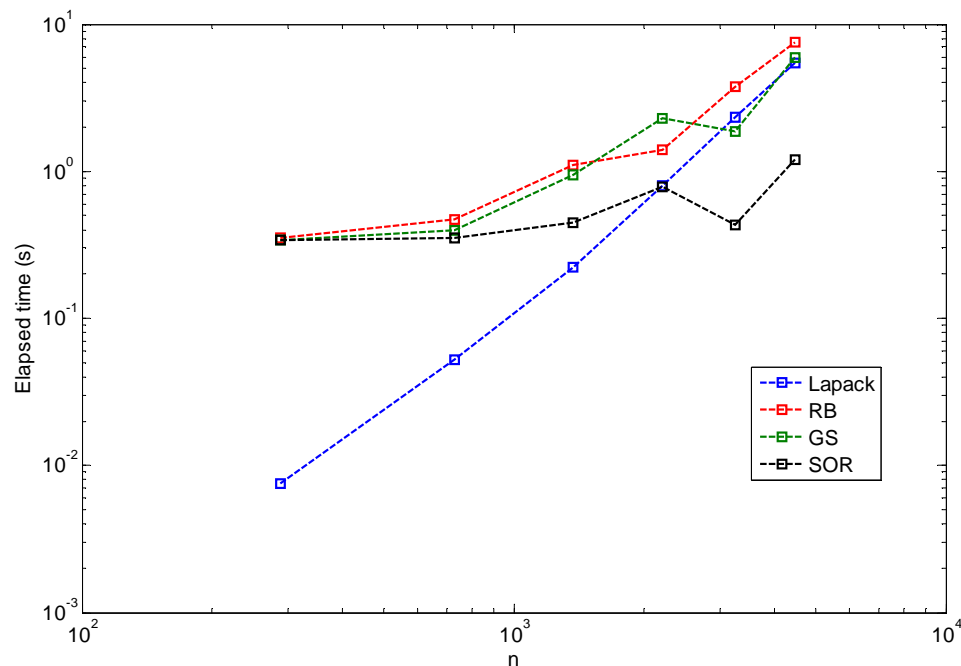


Figure 5.20. Total time for LP and iteration time for iterative solvers in seconds required for different mesh dimensions

### 5.5.4.1.3 Conclusions

Analyzing the results, the following conclusions can be obtained:

- The **LAPACK** subroutines are too slow when dealing with the large meshes that we anticipate will be required in later stages of this project.
- Although **SOR** seems to be faster than the other iterative methods, its implementation is not efficient because the optimum over-relaxation parameter depends on the mesh size. When  $w$  differs from its optimal, the convergence rate deteriorates and the convergence is oscillatory.
- **RB** has approximately the same convergence features than GS. The nice feature of the Red-Black Gauss-Seidel solver is that it both vectorizes and parallelizes well, since there are no data dependencies in either step.
- All the iterative methods that were implemented take advantage of the **sparse structure** of the matrix and do not perform the operations on elements which are zero. Because of this feature, care should be taken when introducing immersed boundaries to make sure that the structure of the matrix is conserved. Further improvement is possible if the sparse structure is also taken into account in terms of storage, i.e., only the non-zero elements are stored.
- The establishment of an **efficient convergence criterion** is a key aspect to develop in order to achieve competitive iterative methods.
- A **multigrid** scheme will potentially introduce a great improvement in the current iterative methods.

### 5.5.4.2 Full Direct Methods versus Sparse Iterative Methods

The difference between sparse and full methods is the way they deal with the data. As it has been explained in section 5.5.1, the matrix to deal with has a sparse structure. While the whole matrix to solve has a size of  $(n_x \cdot n_r, n_x \cdot n_r)$ , the number of non-zero elements is slightly lower than  $5 \cdot n_x \cdot n_r$ . This means that the maximum mesh size that can be solved increases as,

$$(n_x \cdot n_r)_{\max, \text{full}} = \sqrt{5 \cdot (n_x \cdot n_r)_{\max, \text{sparse}}} \quad \text{Eq. 5.84}$$

Considering a memory of 2GB and a mesh where  $n_x=n_r$ , the maximum size that a full solver can handle is  $n_x=n_r=128$ . Using sparse methods the maximum size increases up to  $n_x=n_r=6553$ . More important than the storage requirements, the computational time required to reach the solution is also dependent in which method we use. Section 5.5.4.1 shows that traditional iterative methods are not a competitive alternative because the system is badly conditioned and the solver requires too many iterations to converge, which motivates the usage of modern iterative methods known as Krylov subspace methods (Section 5.5.3.2).

Combinations of preconditioners and iterative solvers have been tested. The best results have been achieved by using a MILU0 preconditioned and GMRES solver, obtaining a substantial improvement with respect to the use of a full direct method.

Table 5.11. Time comparison between iterative sparse solver and direct full solver

Mesh	Solver Sparse – Iterative method	Solver Full – Direct Method
64x64	0.1 s	4.9 s
128x128	0.7 s	260 s
256x256	4 s	(Out of memory)
320x320	9.6 s	(Out of memory)

## 5.6 Validation of the code

### 5.6.1 Introduction

This section attempts to evaluate the code performance under different conditions presented on Table 5.12. First, we study a cavity flow in a square domain where the upper boundary is moving on the horizontal direction. This validates our approach for the stationary state. In order to analyze the time evolution, the second case compares the analytical solution of a well-known problem with the one provided by our numerical model. Last case studies the response of the code to the existence of immersed boundaries analyzing what happens when a circle is introduced in the domain under different conditions.

Table 5.12. Cases

	Case	Boundary Conditions	Mesh size	Re	CFL
CASE 1	Cavity flow	$u_r(x=0,r)=1$	128x128	100	0.1
CASE 2	Vortex	Oseen vortex at $(x,r)=(0.5,0.5)$	256x256	5	0.1
CASE 3	Immersed circle	3.a) $u_r(x=0,r)=1$	253x253	1	0.1
		3.b) Oseen vortex at $(x,r)=(0.5,0.5)$	253x253	1	0.1
		3.c) Translation circle. $u_{r\text{circle}}=0.05$	253x253	12	0.1
		3.d) Rotation circle. $\omega_{\text{circle}}=0.1$	253x253	20	0.1

Numerical solutions of the fluid flow are only approximate solutions. In addition to the errors that might be introduced by the assumptions made in the mathematical formulation of the problem, in programming or setting the boundary conditions. Before starting the validation of the code, it is important to estimate the value of the error. Numerical solutions always include three kinds of systematic errors:

- **Modeling errors**, which are defined as the difference between the actual flow and the exact solution of the mathematical model. These errors depend on the assumptions made in deriving the transport equations for the variables. Since the Navier-Stokes equations represent a sufficiently accurate model of the flow here investigated these errors are considered negligible.
- **Discretization errors**, defined as the difference between the exact solution of the conservation equations and the exact solution of the algebraic system of equations obtained by discretizing these equations. Discretization errors depend on the mesh size ( $\Delta x, \Delta r$ ) and the length of the time step  $\Delta t$ . There are three sources for discretization errors:
  - o Time stepping: The Runge-Kutta integration scheme gives an error of  $O(\Delta t^3)$
  - o Spatial discretization: Second order finite differences give an error  $O(\Delta x^2, \Delta r^2)$
  - o Boundary conditions: IB gives an error that goes as  $O(\Delta x^2, \Delta r^2)$
 The global error is the maximum of these errors. If  $\Delta x \sim \Delta r$  and  $CFL \sim 1$ ,  $\Delta t \sim \Delta x/u \sim \Delta x$ , the global discretization error is  $O(\Delta x^2) \sim O(\Delta r^2) \sim O(\Delta t^2)$ .
- **Iteration errors**, defined as the difference between the iterative and exact solutions of the algebraic equations system. The solver has been implemented to guarantee that iteration error is lower than discretization error, so they can be neglected.

### 5.6.2 CASE 1: Cavity flow.

A classical test problem is numerical simulation of a laminar or turbulent flow of an incompressible viscous fluid in a square cavity with the upper moving boundary (see Figure 5.21). It has long since been a testing area for approbation of approximation schemes for terms in initial equations as well as of computational models and methods. A large number of calculation data concerning this problem have been accumulated. We are going to compare here the results provided by our code with the ones given by a code from the Applied Mathematics Massachusetts Institute of Technology (MIT) and some available experimental data.

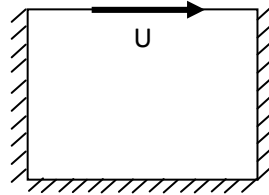


Figure 5.21. Cavity flow.

Figure 5.22 presents pressure and velocity distribution for a cavity flow at  $Re=100$ . Black lines represent our solution and the contours correspond to MIT solution. It can be seen how both solutions agree well.

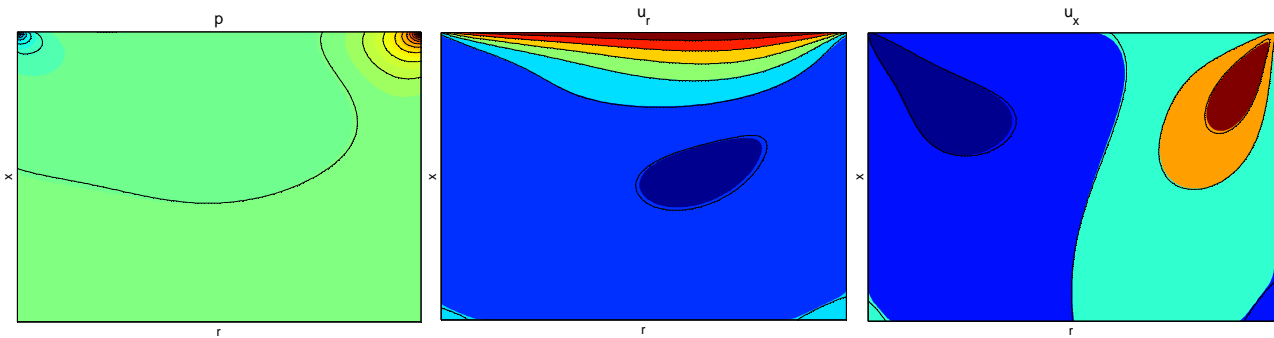


Figure 5.22. Pressure and velocity fields.

Figure 5.23 shows the evolution of  $u_r$  along a vertical axis that cuts the cavity at  $r=0.5$ . Numerical solutions and experimental data fit.

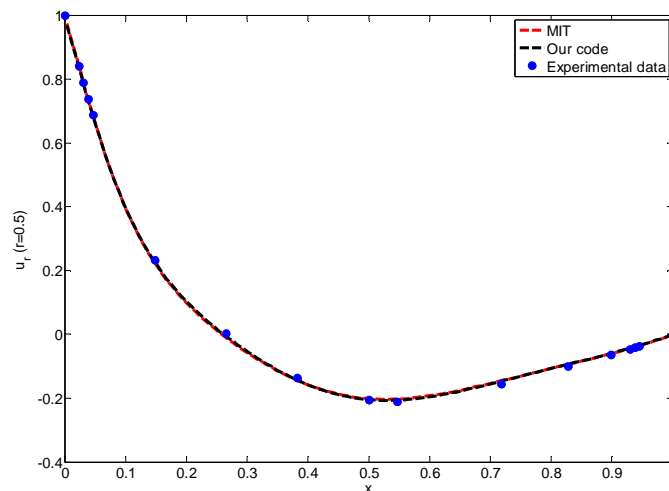


Figure 5.23. Velocity profile (r direction) at  $r=0.5$ .

### 5.6.3 CASE 2: Lamb-Oseen vortex

#### 5.6.3.1 Introduction

The goal of this research is to understand the dependence of the time evolution of the LV vortex ring on the duration of the LV filling phases, and to determine how this dependence affects blood flow transport in the LV and global ventricular function. Thus it is interesting to test how the code behaves in the presence of a vortex. In order to reach this purpose, the evolution a simple vortex where the analytical solution is well known is going to be studied. Valuable information about the code performance can be obtained when comparing the analytical solution with the numerical one. The vortex is introduced in a square cavity with a size  $L$  much larger than the radius of the vortex.

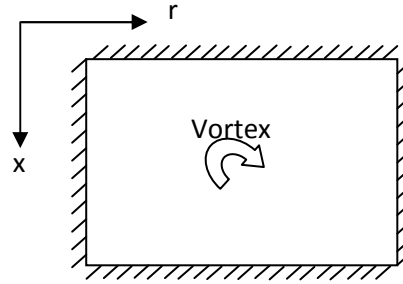


Figure 5.24. Vortex.

#### 5.6.3.2 Lamb-Oseen vortex

The simplest viscous vortex, this is, the Lamb-Oseen vortex will be the flow initial condition. The code should be able to reproduce the evolution of the vortex that is predicted by the analytical solution. This section briefly summarizes how to solve the Navier-Stokes equations to achieve the analytical expressions that governs the vortex behavior.

##### 5.6.3.2.1 Velocity and pressure

The Lamb-Oseen vortex is a two dimensional flow with circular symmetry, the radial velocity is null while the azimuthal velocity is perpendicular to the radial direction and independent of the angle. Thus, the Navier-Stokes mass conservation equation does not provide any valuable information. Applying conservation of momentum in the azimuthal direction a differential equation for  $v_\theta$  is obtained (Eq. 5.85).

$$\frac{\partial v_\theta}{\partial t} = \nu \frac{\partial}{\partial r} \left( \frac{1}{r} \frac{\partial}{\partial r} (r v_\theta) \right) \quad \text{Eq. 5.85}$$

The solutions will be sought in the form  $v_\theta \sim \beta / r^n$  as  $\frac{r}{\sqrt{\nu t}} \rightarrow \infty$ , and  $v_\theta$  analytic at  $r=0$ . The singular behavior is then smoothed out in a boundary layer core of radius  $(\sqrt{\nu t})$ . One of the exact solutions for this equation that satisfies the requirements is,

$$v_\theta = \frac{\Gamma_0}{2\pi r} (1 - e^{-r^2/4\nu t}) \quad \text{Eq. 5.86}$$

Where  $\Gamma_0$  is the circulation contained in the vortex and  $\sqrt{4\nu t}$  can be redefined as  $r_c$ , the core radius of the vortex. Thus, angular velocity can be expressed as,



$$v_\theta = \frac{\Gamma_0}{2\pi r} (1 - e^{-r^2/r_c^2}) \quad \text{Eq. 5.87}$$

The integration of the conservation of momentum in the radial direction provides an analytical expression of the pressure:

$$-\frac{v_\theta^2}{r} + \frac{1}{\rho} \frac{\partial p}{\partial r} = 0 \rightarrow p = \int \frac{\rho v_\theta^2}{r} dr \quad \text{Eq. 5.88}$$

$$p = \frac{1}{4} \frac{\Gamma_0^2}{\pi^2} \left( -\frac{1}{2r^2} + \frac{e^{-\frac{r^2}{r_c^2}}}{r^2} - \frac{e^{-\frac{2r^2}{r_c^2}}}{2r^2} + \frac{Ei\left(1, \frac{2r^2}{r_c^2}\right)}{r_c^2} - \frac{Ei\left(1, \frac{r^2}{r_c^2}\right)}{r_c^2} \right) \quad \text{Eq. 5.89}$$

Where Ei is the exponential integral function, defined as

$$Ei(a, x) = \int_1^\infty e^{-tx} t^{-a} dt. \quad \text{Eq. 5.90}$$

By simply projecting the velocity in Cartesian coordinates, the analytical velocity and pressure can be introduced as initial flow conditions.

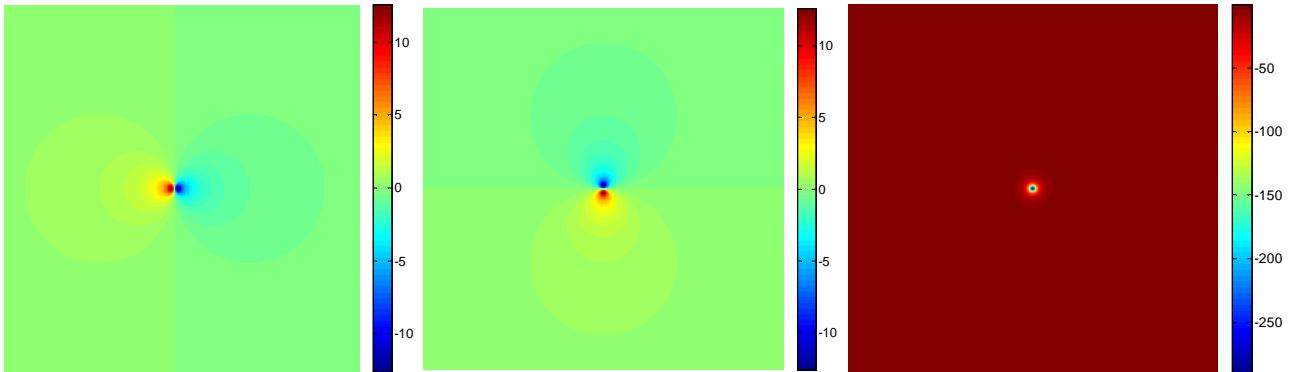


Figure 5.25. Initial flow conditions (from left to right,  $u_x, u_r, p$ )

Introducing the initial condition for pressure is not strictly required. Part of the pressure is computed explicitly and then it is corrected. However, if the pressure is introduced in the initial condition the error in the first steps is expected to be smaller because the pressure correction is smaller.

Equations for pressure and velocity require two parameters in order to define the vortex: the circulation contained in the vortex ( $\Gamma_0$ ) and the core radius of the vortex ( $r_c$ ). They should be selected on a way that assures that the vortex is small compared with the cavity dimensions to be able to compare numerical and analytical solutions due to the fact that the analytical expressions are valid for an unbounded domain.

#### 5.6.3.2.2 Vorticity and circulation

The motion of a fluid is described by the velocity field. The curl of the velocity is called the vorticity,  $\vec{\omega}(\vec{x}, t)$ . It has a great significance and importance for the description and understanding of fluid flows and allows a more economical description of the structure and the evolution of the fluid flow (83).

$$\vec{\omega} = \nabla \times \vec{v} \quad \text{Eq. 5.91}$$

Considering the Lamb-Oseen vortex, the vorticity is a function of radial distance  $r$  and time  $t$  in the plane defined by  $x$ - $r$  coordinates,

$$\omega = \frac{\Gamma_0}{4\pi\nu t} (e^{-r^2/4\nu t}) \quad \text{Eq. 5.92}$$

A scalar function of considerable importance in the description of vortex flows is the circulation  $\Gamma$  around a simple closed curve, defined as the line integral of the velocity.

$$\Gamma = \oint \vec{v} \cdot d\vec{l} \quad \text{Eq. 5.93}$$

It follows from Stokes theorem that the circulation around a reducible curve is equal to the flux of vorticity through an open surface bounded by the curve, that is,

$$\Gamma = \oint \vec{v} \cdot d\vec{l} = \iint \vec{\omega} \cdot \vec{n} dS \quad \text{Eq. 5.94}$$

Applying this definition to the flow here considered, the analytical expression of the circulation is,

$$\Gamma = \oint \vec{v} \cdot d\vec{l} = \int_0^{2\pi} v_\theta r d\theta = \Gamma_0 (1 - e^{-r^2/4\nu t}) \quad \text{Eq. 5.95}$$

#### 5.6.3.2.3 Non-dimensional parameters

The analysis in the pressing sections suggests a set of parameters to be established when defining a vortex: the core radius, the viscosity of the flow, the circulation contained in the vortex, the time origin... The performance of a non-dimensional study of the equations is the base of a proper analysis of these parameters. If the initial circulation and initial core of the vortex are the fundamental variables, the non-dimensional variables and parameters are the ones presented in Eq. 5.96.

$$\widehat{v}_\theta = \frac{v_\theta r_{c0}}{\Gamma_0}; \widehat{p} = \frac{pr_{c0}^2}{\Gamma_0^2}; \widehat{\omega} = \frac{\omega r_{c0}^2}{\Gamma_0}; \widehat{\Gamma} = \frac{\Gamma}{\Gamma_0}; \widehat{r} = \frac{r}{r_{c0}}; \widehat{t} = \frac{(t + t_0)\Gamma_0}{r_{c0}^2}; Re = \frac{\Gamma_0}{\nu} \widehat{r}_c = \frac{r_c}{r_{c0}} = \sqrt{\frac{4\widehat{t}}{Re}}; \quad \text{Eq. 5.96}$$

The initial core of the vortex ( $r_{c0}$ ) is determined by selecting the time origin  $t_0$ . This time origin is just a tool to define the initial size of the vortex. If  $t_0 = 0$ , the initial core of the vortex is zero and the problem is singular, thus,  $t_0 > 0$ . The initial core of the ratio is then defined as,

$$r_c(t) = \sqrt{4\nu(t + t_0)} \quad r_{c0} = r_c(t = 0) = \sqrt{4\nu t_0} \quad \text{Eq. 5.97}$$

Taking this into account, the non-dimensional equations for the velocity, pressure vorticity and circulation are,

$$\widehat{v}_\theta = \frac{1}{2\pi\widehat{r}} \left( 1 - e^{-\frac{Re\widehat{r}^2}{4\widehat{t}}} \right) \quad \text{Eq. 5.98}$$

$$\hat{p} = \frac{1}{4\pi^2} \left( -\frac{1}{2\hat{r}^2} - \frac{e^{-\frac{Re\hat{r}^2}{4\hat{t}}}}{\hat{r}^2} - \frac{e^{-\frac{Re\hat{r}^2}{2\hat{t}}}}{2\hat{r}^2} + \frac{Re}{4\hat{t}} \left( Ei\left(1, \frac{Re\hat{r}^2}{2\hat{t}}\right) - Ei\left(1, \frac{Re\hat{r}^2}{4\hat{t}}\right) \right) \right) \quad \text{Eq. 5.99}$$

$$\hat{\omega} = \frac{Re}{4\hat{t}\pi} \left( e^{-\frac{Re\hat{r}^2}{4\hat{t}}} \right) \quad \text{Eq. 5.100}$$

$$\hat{\Gamma} = \left( 1 - e^{-\frac{Re\hat{r}^2}{4\hat{t}}} \right) \quad \text{Eq. 5.101}$$

### 5.6.3.3 Code evolution

In order to validate the code, it is important not only to obtain the appropriate response in terms of the fluid dynamics variables, but also to assess the performance in terms of resolution: how does the error decrease when the grid is refined or the CFL condition reduced. In this section, the fluid dynamic response of the code is going to be analyzed first. Once it is clear that the behavior is appropriate, the resolution will be studied. Figure 5.1 presents the non-dimensional parameters used for the simulations of all the cases studied.

Table 5.13. Non-dimensional parameters.

		$\Gamma_0$	$r_{c0}$	$t_0$	CFL
Fluid dynamics analysis	Pressure	1	$23 \cdot 10^{-3}$	$68.1 \cdot 10^{-5}$	0.1
	Vorticity	1	$8 \cdot 10^{-3}$	$7.6 \cdot 10^{-5}$	0.1
	Circulation	1	$16 \cdot 10^{-3}$	$30.3 \cdot 10^{-5}$	0.1
Resolution analysis		1	$[2 \cdot 10^{-3}, 23 \cdot 10^{-3}]$	$[0.5 \cdot 10^{-5}, 68.1 \cdot 10^{-5}]$	0.1
Temporal analysis		1	$16 \cdot 10^{-3}$	$30.3 \cdot 10^{-5}$	[0.05,5]

#### 5.6.3.3.1 Fluid dynamics analysis

##### Pressure

In order to assess the accuracy of the numerical solution, the evolution of pressure in one particular point is monitored over time. In principle, any point could be selected. If the point is far enough from the walls and the vortex is small compared with the dimension of the cavity, the numerical and analytical solution fit well as shown in Figure 5.26. It is interesting to see how the code initially needs some time to converge to the analytical solution. Afterwards, numerical and analytical solution fit until the effect of the walls is felt at the point in which the pressure is measured, in this case, the center of the grid. The difference in the absolute value of pressure is not worrying because what matters is the pressure gradients and not its absolute value.

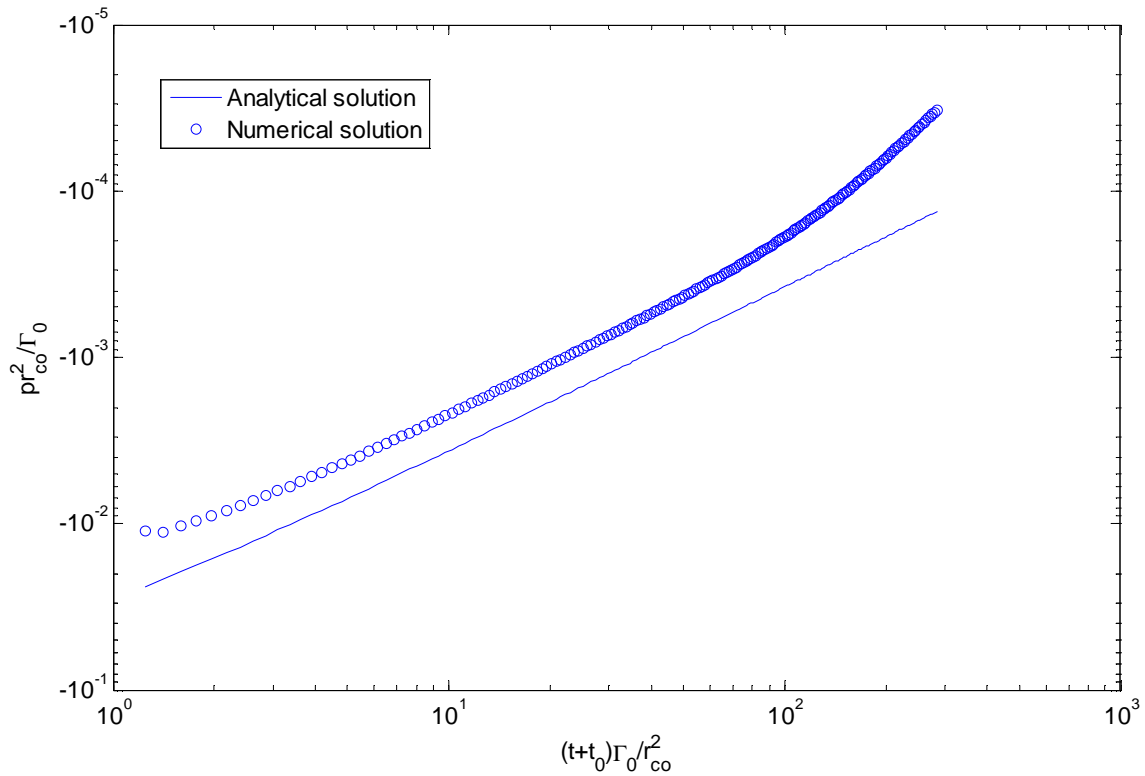
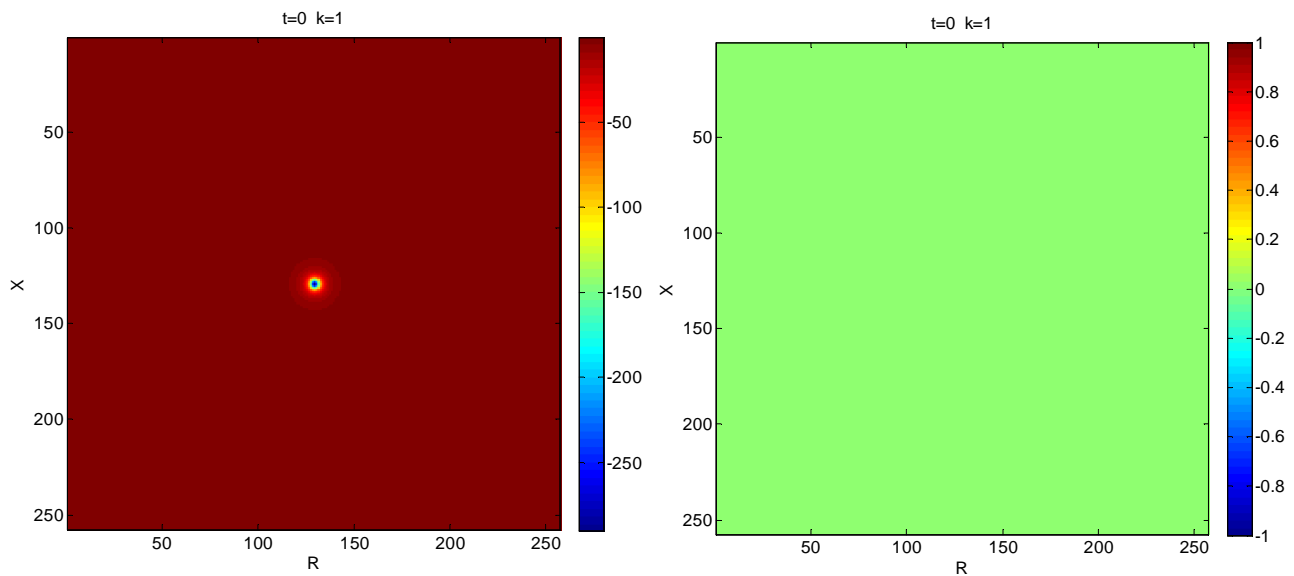


Figure 5.26. Time evolution for the numerical and analytical pressure at the center of the vortex.

As it has been outlined before, it is not strictly required to impose an initial condition in pressure, but it should provide faster convergence. However, in this particular case, as in the first time step the flow suffers a great disturbance due the presence of walls, imposing initial conditions does not lead to any improvement as it can be appreciated in Figure 5.27. The left panel represents the pressure distribution in the three first steps when the initial condition is the pressure determined by the analytical expression. The right panel considers a uniform initial condition for pressure.



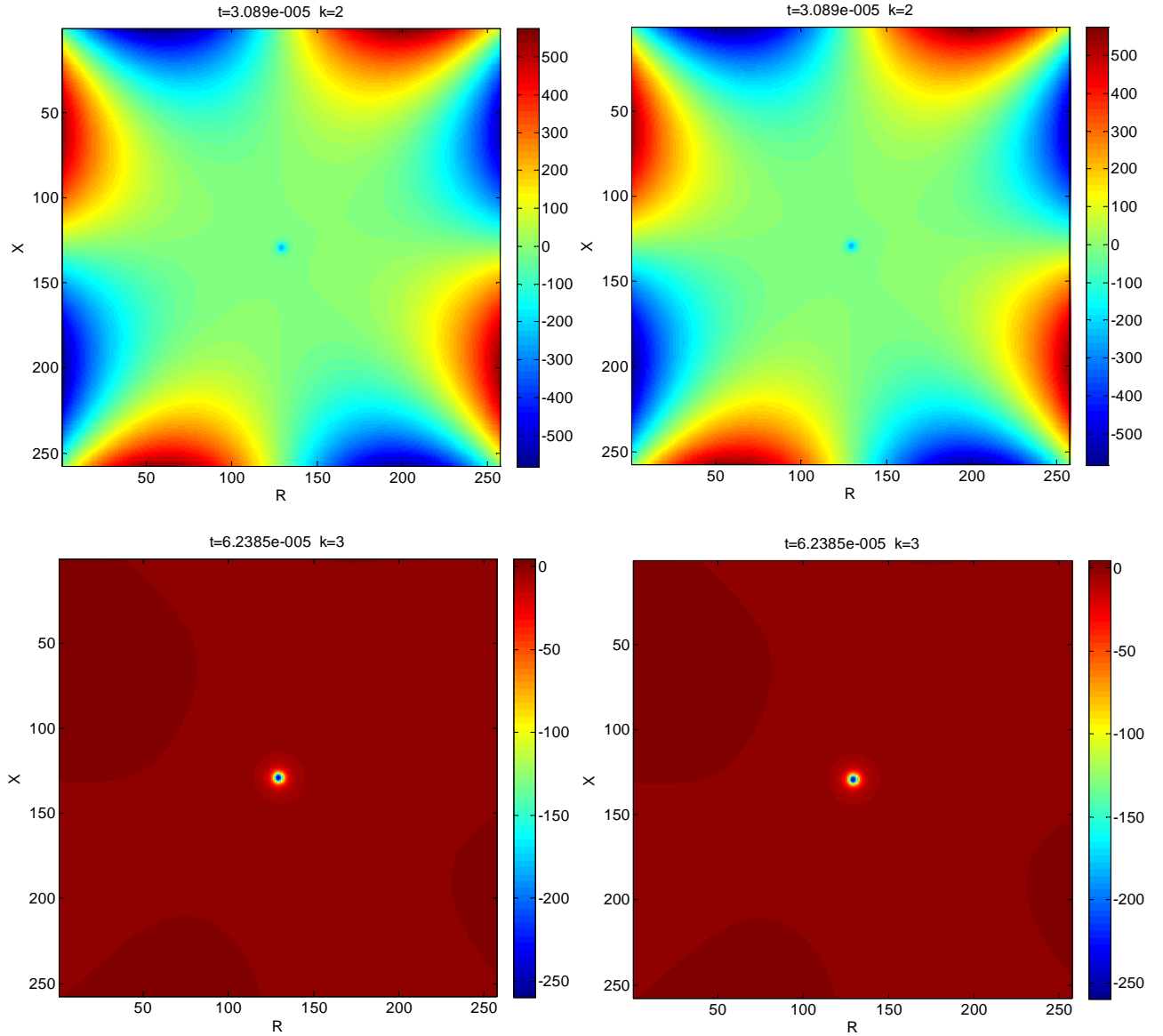


Figure 5.27. Pressure distribution for the three first time steps. Left:  $p(t=0)=p_{\text{analytical}}$ ; Right:  $p(t=0)=0$ .

### Vorticity

As described before, vorticity has a great significance and importance for the description and understanding of fluid flows. A very stable vortex is inserted in the fluid as initial condition. In absence of walls, the vorticity will decrease as predicted by Eq. 5.100.

The walls will behave as source of vorticity and will disturb the solution. As the velocity at the walls has to be zero, the vorticity generated at the walls has to have opposite sign to the flow vorticity. Eq. 5.28 shows the vorticity distribution for three different times.  $\omega(r, t)/\omega(r = 0, t)$  as function of  $r/r_c$  clearly show that the solution matches with the analytical one at  $t=0$ , but as time advances, the boundary layer formed in the walls introduces negative vorticity in the flow.

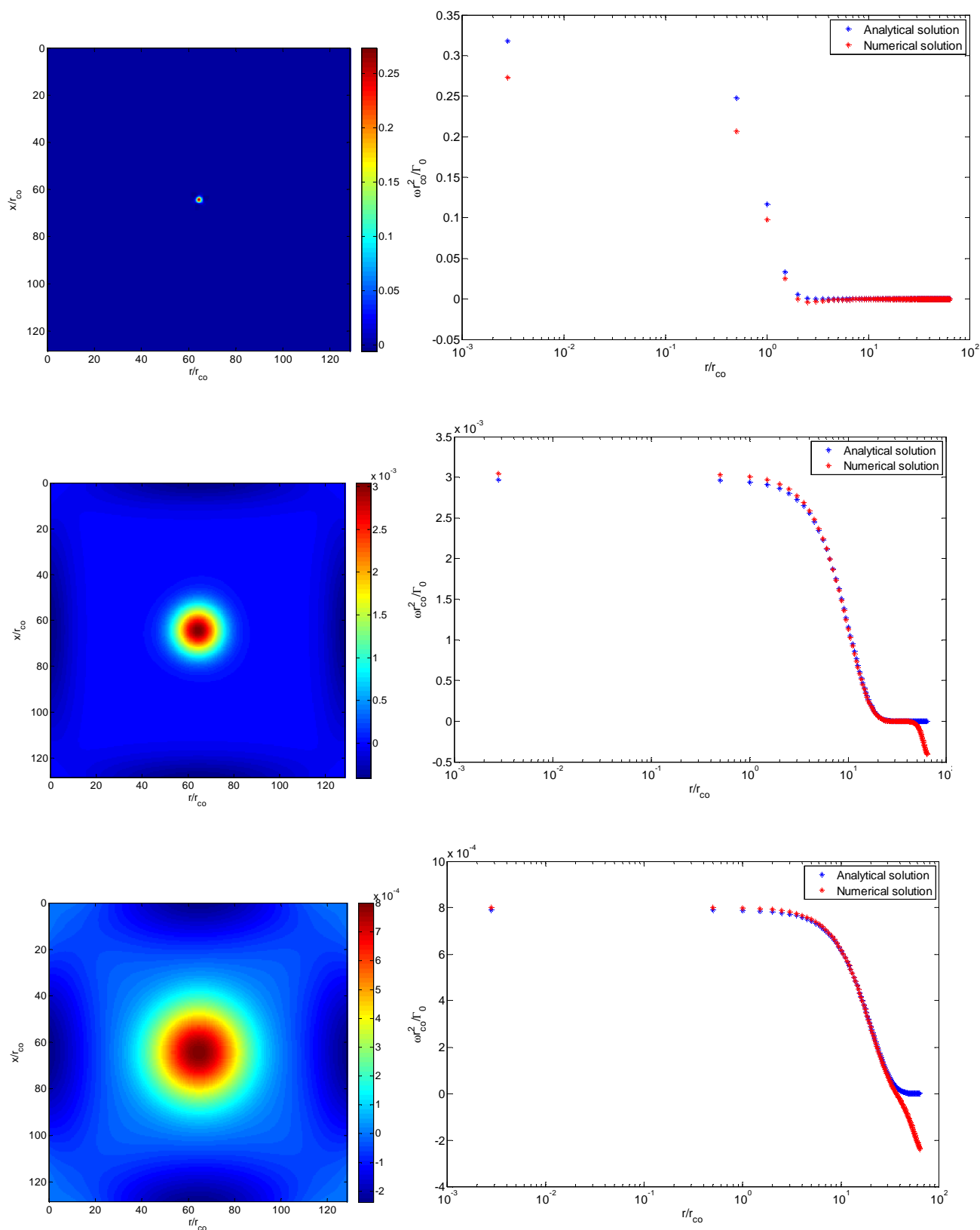


Figure 5.28. Vorticity distribution for iteration 1, 50 and 100 (from top to bottom).

When the time increases over a certain value, the distortion of the walls is spread over the full domain and analytical and numerical solution differ. Eq. 5.29 shows the time evolution of the vorticity in the core of the vortex, this is, for  $r=0$ .

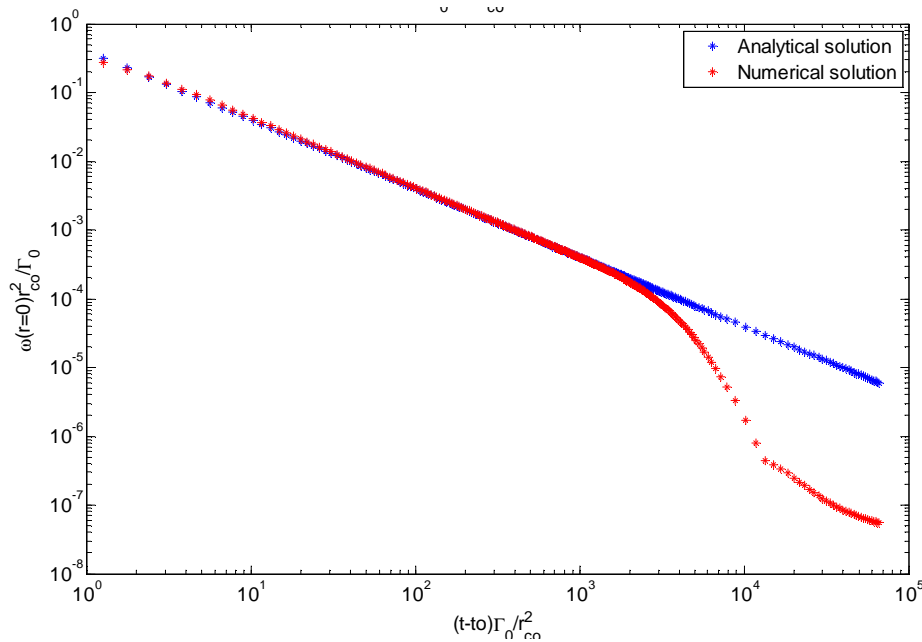


Figure 5.29. Time evolution of the vorticity for  $r=0$ .

### Circulation

The circulation along any closed line in the flow field is an integral magnitude which is useful to describe and determine if the code is providing coherent results. The line selected to evaluate this circulation is the line at which the velocity is maximum. As expected, the circulation has fluctuating values at the beginning, while the stroke of the first is corrected. Then, it follows the analytical solution until the effect of the walls becomes predominant and its dissipation leads to zero circulation. This behavior is presented in Figure 5.30.

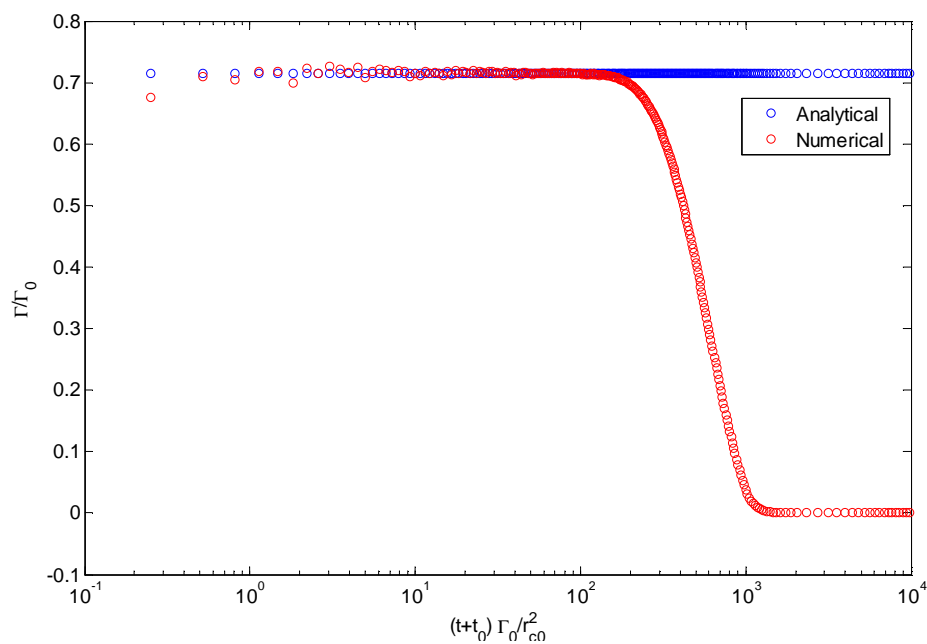


Figure 5.30. Evolution of the circulation along the line of maximum velocity.

### 5.6.3.3.2 Resolution analysis

Once it is clear that the code is providing coherent results from the fluid dynamics point of view, it is important to evaluate the influence of the resolution in time and space.

#### Spatial resolution

Spatial resolution is defined as function of the grid size:

$$dx = \frac{1}{nx} \quad dr = \frac{1}{nr} \quad \text{Eq. 5.102}$$

The initial ratio of the core is defined as function of the mesh size as follows:

$$r_{co} = \frac{k}{\text{sqrt}(nx \cdot nr)} \quad \text{Eq. 5.103}$$

Thus, compromise between  $k$  big enough to describe accurately the vortex and small enough to be able to ignore the effect of the walls for a certain period of time is to be achieved for a certain mesh dimension.

As it has been described in section 5.6.3.2 different magnitudes can be analyzed to determine the code performance. Circulation is the one selected here because it provides an integral measure of the flow. Figure 5.31 represents the evolution of circulation with time in dimensionless variables for different values of  $k$ .  $k$  lower than 2 yields to inaccurate solutions at short times because at  $t=0$  the resolution is insufficient to properly describe the vortex. It is important to notice how even for low values of  $k$ , the solution converges to the analytical in a reasonable period of time because the effective  $k$  increases when increasing the vortex size. The effect from the walls travels fast through the flow until the circulation drops to zero.

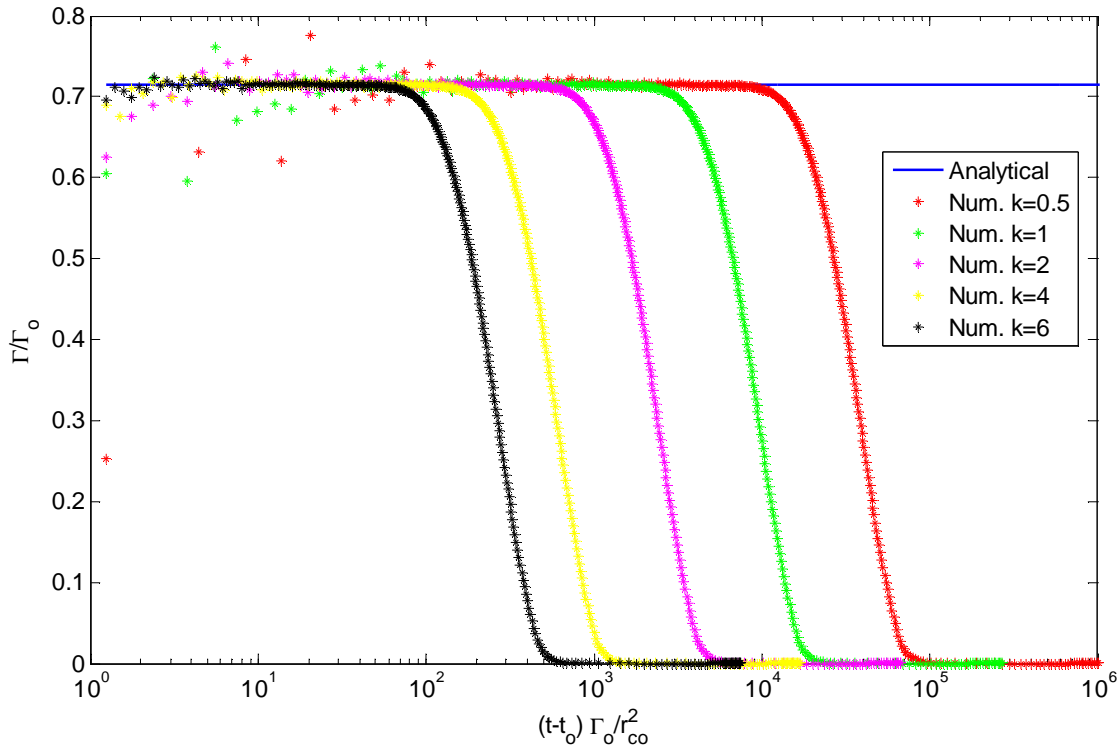


Figure 5.31. Circulation evolution with time for different initial core radius.



### Temporal resolution

Time step is defined as function of the CFL, grid size and velocities as:

$$dt = CFL \cdot \min\left(\frac{dx}{\max(|u_x|)}, \frac{dr}{\max(|u_r|)}\right) \quad \text{Eq. 5.104}$$

Increasing the CFL, the time step increases and the solution converges faster. The problem arises when CFL is too high so the problem does not converge. Thus, the stability of the numerical scheme will limit the temporal resolution. In addition, the error is proportional to  $(CFL)^n$ , where  $n$  is the order of the scheme. That is why CFL should remain small even if the code is stable.

### Euler

In the original integration scheme non linear terms were discretized following Explicit Euler and viscous terms with Implicit Euler. Figure 5.32 and Figure 5.33 show how when CFL decreases the temporal resolution increase and analytical and numerical solution fit better.

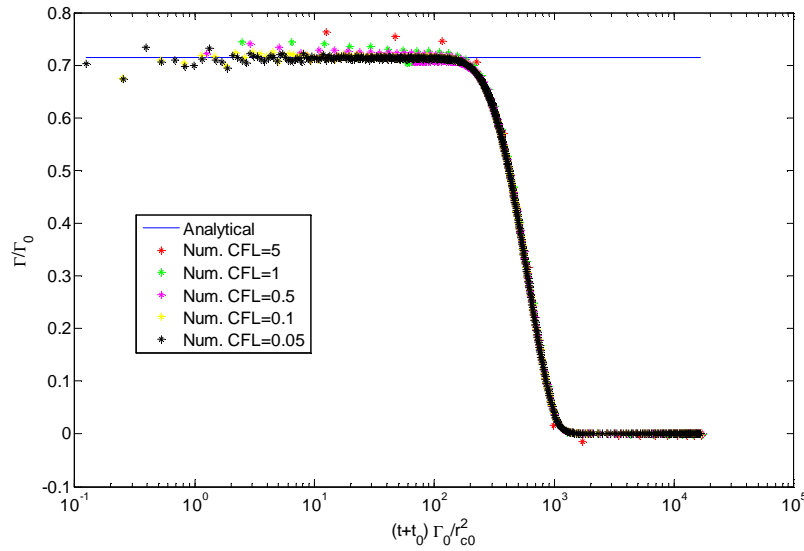


Figure 5.32. Circulation evolution with time for different CFL.Euler.

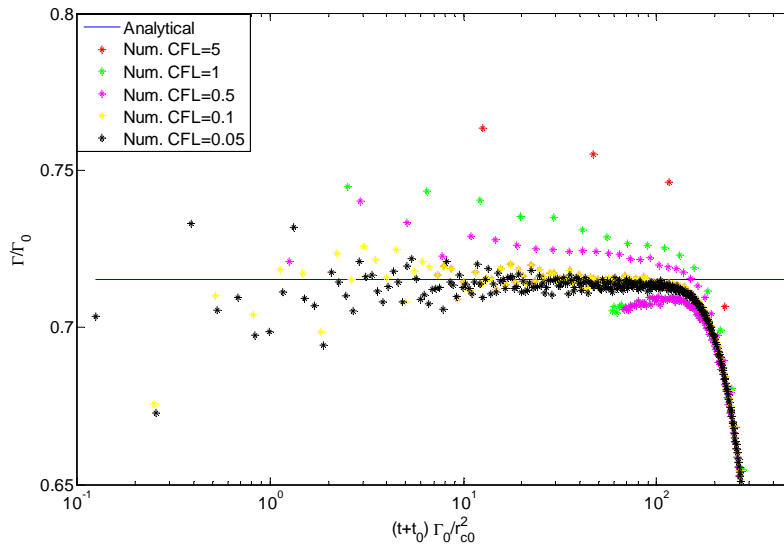


Figure 5.33. Circulation evolution with time for different CFL.Euler. (zoom)

### Runge-Kutta (RKWT)

The integration scheme described in section 5.4.2 allows the usage of higher CFL. Figure 5.34 and Figure 5.35 are the analogous to Figure 5.32 and Figure 5.33 using Runge-Kutta integration procedure instead of Euler.

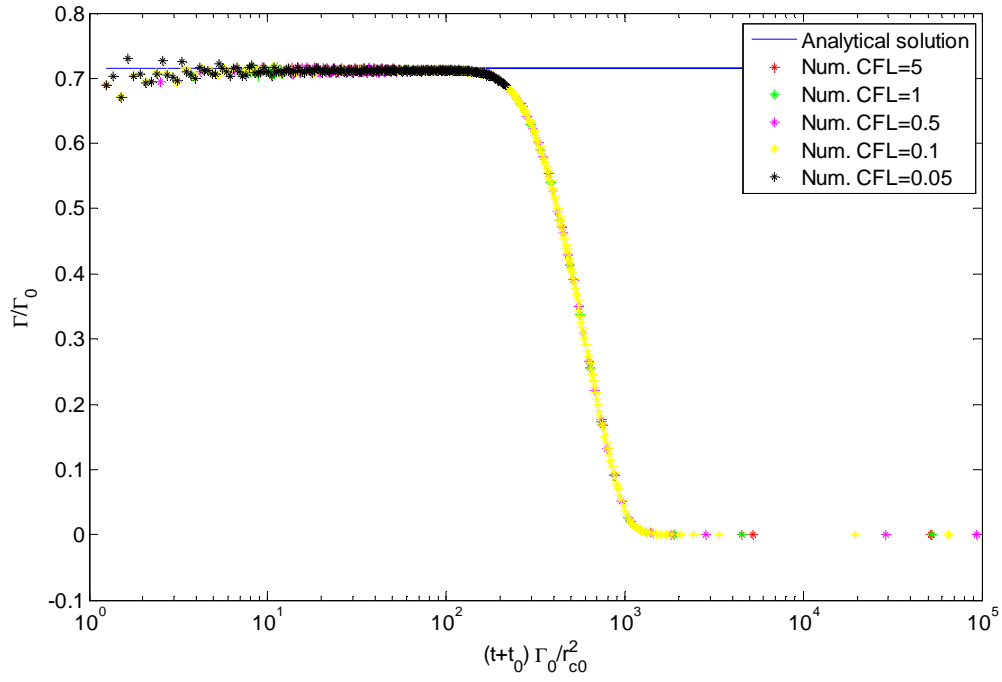


Figure 5.34. Circulation evolution with time for different CFL. Runge-Kutta.

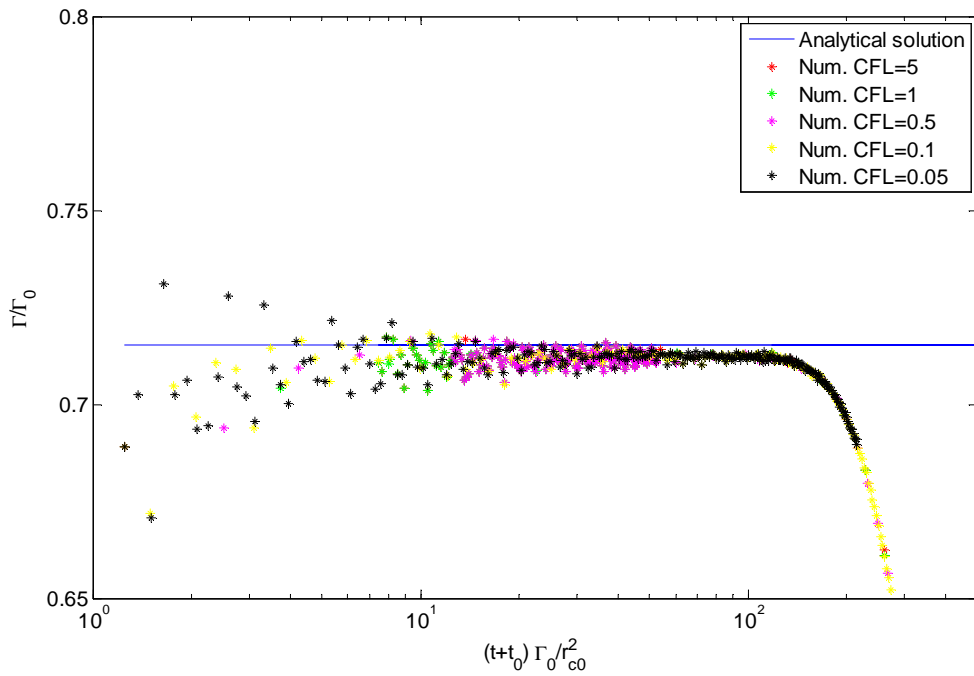


Figure 5.35. Circulation evolution with time for different CFL. Runge-Kutta. (zoom)

### 5.6.4 CASE 3: Immersed circle

#### 5.6.4.1 Introduction

The aim now is the evaluation of the immersed boundaries analyzing the solution when a circle is introduced into the domain. The capabilities and limitations of the interpolation technique implemented on the boundaries are shown and some conclusions about how to define the boundary and the interior points are reached. The circle is evaluated under four conditions:

- Circle in presence of a cavity flow. This example will help us to achieve some conclusions about how to impose the conditions on the boundary and on the interior point of the body.
- Circle in presence of a vortex. This example shows how the code is able to identify and to be adapted to a body introduced on the domain.
- Moving circle. This example evaluates the code performance when the immersed body is moving. Translational and rotational movements have been analyzed.

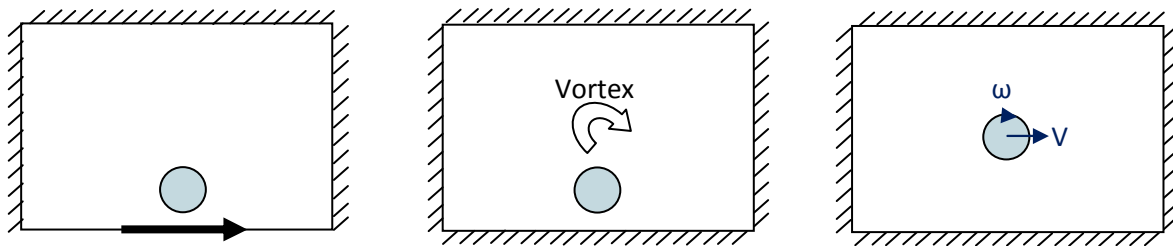


Figure 5.36. Immersed circle. Case 3a (Circle + moving boundary), Case 3b (Circle + vortex) and Case 3c (Moving circle)

#### 5.6.4.2 Case 3a. Circle in presence of a cavity flow

This section analyses one more time the flow that appears on a fluid in a square cavity with the upper moving boundary. This flow is used a tool to identify the best way of imposing the boundary conditions and treating the internal points of the body.

##### 5.6.4.2.1 Boundary definition

Ghost points (these are, nodes in which the conditions of the immersed boundary are imposed) need to be identified. Two approaches are available:

- **First approach:** Ghost points belong to the Fluid Domain. Thus, it is guaranteed that points inside the boundary satisfy the boundary conditions but there is a set of points in the fluid domain close to the boundary where we impose the boundary conditions instead of solving the Navier-Stokes equations.
- **Second approach:** Ghost points belong to the Body Domain. Thus, the Navier-Stokes equations are solved in the entire fluid domain. These points have a value such that the conditions on the boundary are satisfied.

The following sketch clarifies both approaches.

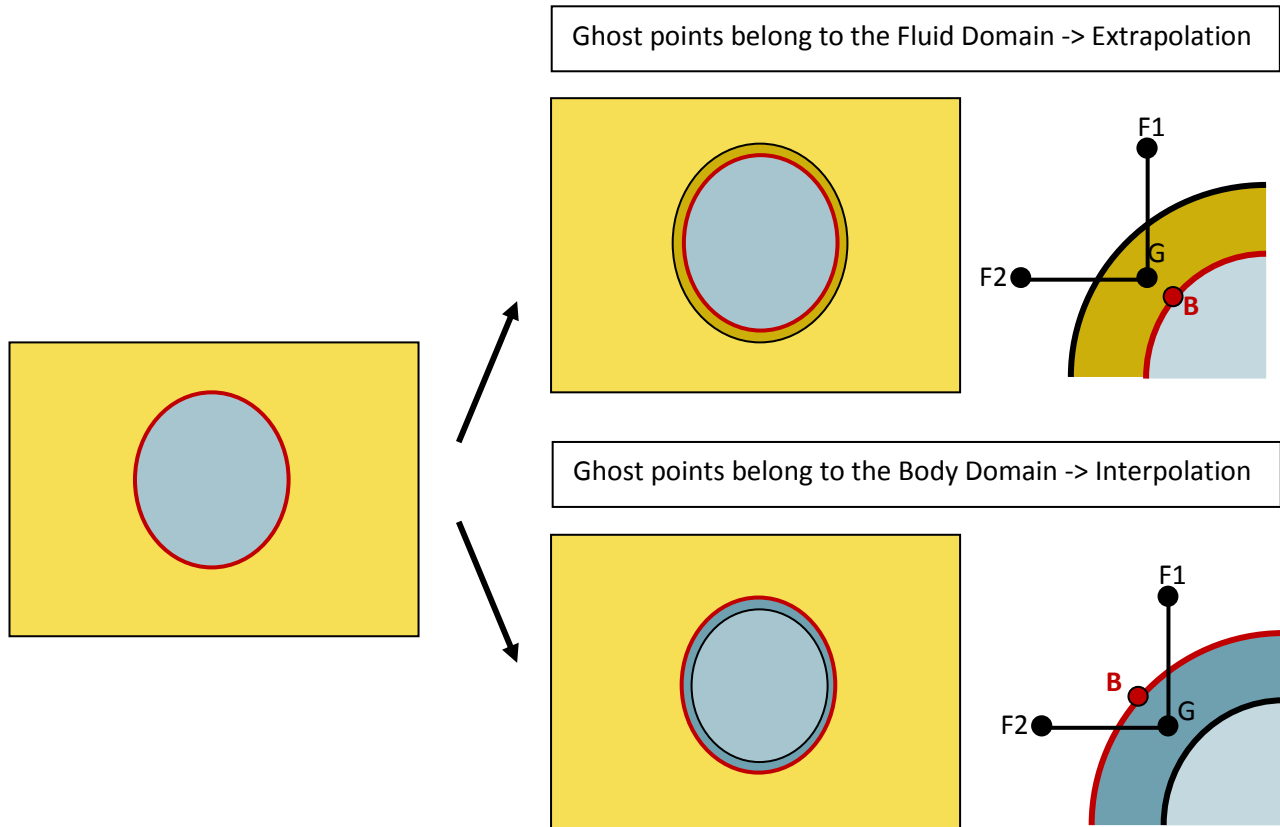


Figure 5.37. Ghost point identification

As interpolation usually provides more accurate results than extrapolation, the selection of the ghost cells inside the domain drives to better results. In the particular case of the circle, two types of ghost points can be distinguished:

- **Ghost points type A:** Interpolation to impose boundary conditions can be performed with nodes which belong to the fluid domain (Figure 5.38, blue points).
- **Ghost points type B:** At least one of the nodes used to interpolate has to belong to the solid (Figure 5.38, red points).

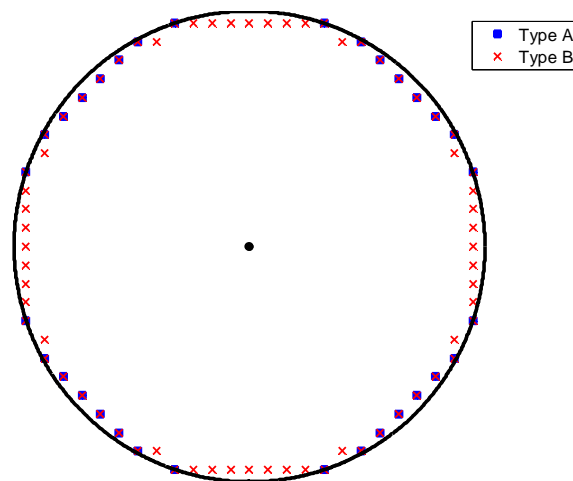


Figure 5.38. Ghost point identification

If only type A points are selected to impose the boundary conditions, big portions of the surface of the circle are not properly defined in terms of boundary conditions. Taking both types of nodes the solution is better. Using internal points of the body to interpolate the value of the ghost cell does not involve any inconvenience.

#### 5.6.4.2.2 Internal treatment of the body

The two options analyzed here are:

- To impose the velocity distribution inside the body (Case 1).
- To leave the interior of the body free to develop a flow without imposing anything (Case 2).

The numerical simulations performed show how the imposition of certain conditions inside the body leads to problems when dealing with the pressure. The problem does not converge and the pressure rises to very high values at certain points. When the interior of the body is free of immersed conditions, this problem disappears. As an example, Figure 5.39 presents the pressure distribution obtained for both cases.

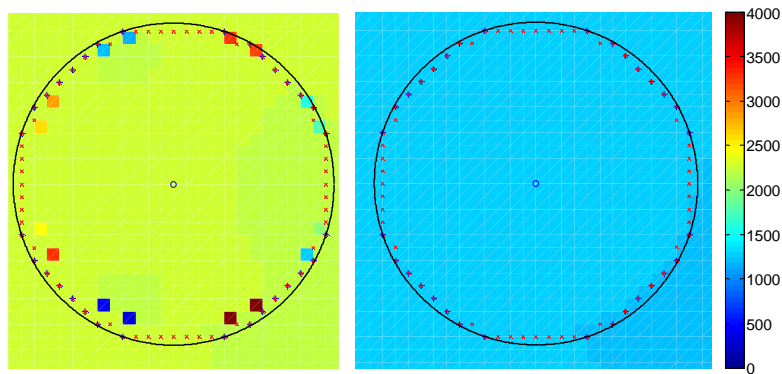


Figure 5.39. Pressure distribution imposing velocity inside the body (left) and leaving the interior flow free (right)

Obviously, the solution is not properly achieved. Even though, analyzing the velocity distributions obtained following both approaches, the differences are small.

Figure 5.40 presents the pressure (first row), velocity in x direction (second row) and velocity in r direction (third row). The first column corresponds to the case in which the conditions inside the body are imposed and the second column leaves free the flow inside the body. The third column shows the difference between them. The flow is the one that appears when the lower wall is moving, for a  $Re=1$ . The circle is centered close to the moving wall. It can be appreciated how the pressure is increasing every time step at different rates if the velocity is imposed or not inside the immersed body. This could involve a problem in the way of solving the singularity of the pressure. If we compare the standard deviation of the pressure instead of absolute values (Figure 5.41), both approaches yield to similar results. This means that we are reaching the solution

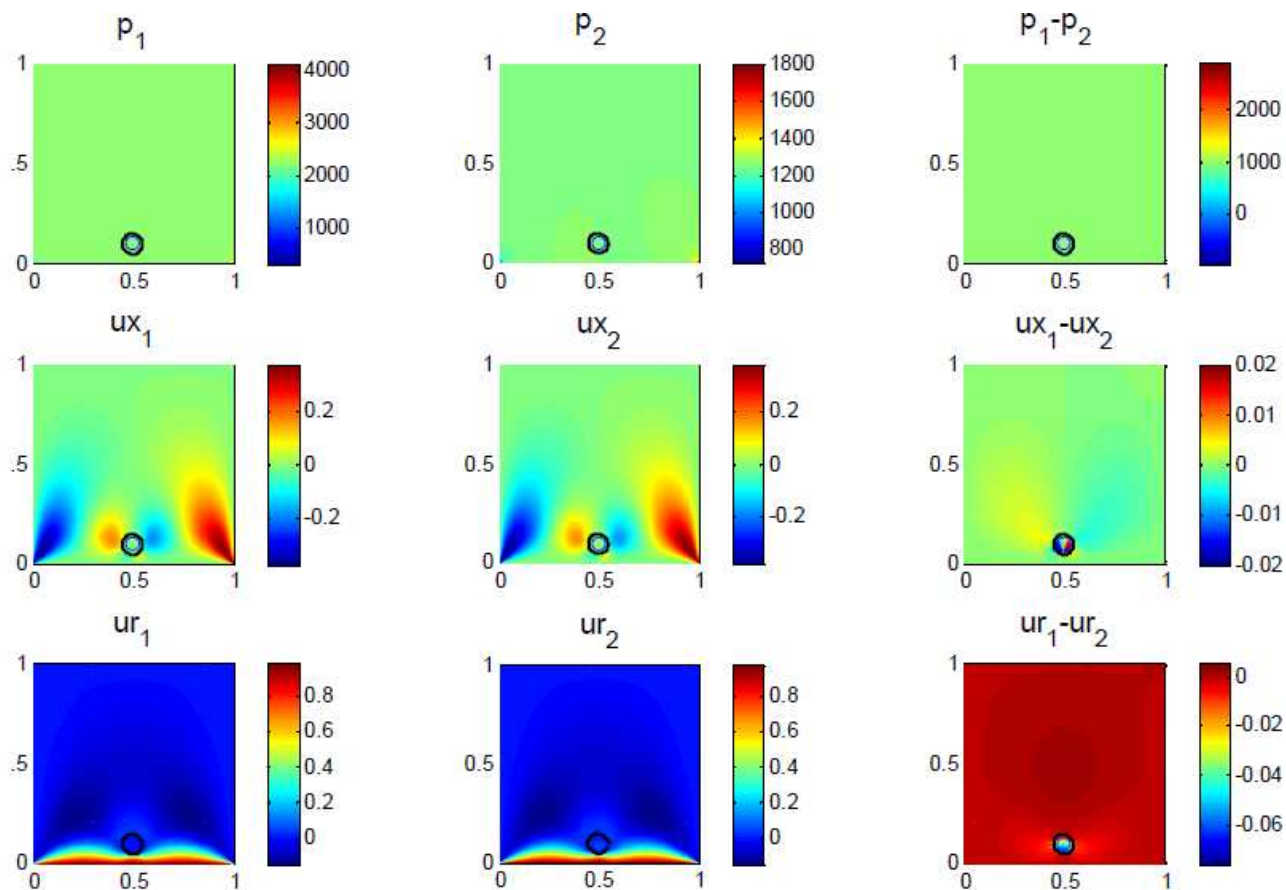


Figure 5.40. Pressure and velocity distribution imposing conditions imposing the velocity distribution inside the body (left) and leaving the interior of the body free (central column). Difference between them (right)

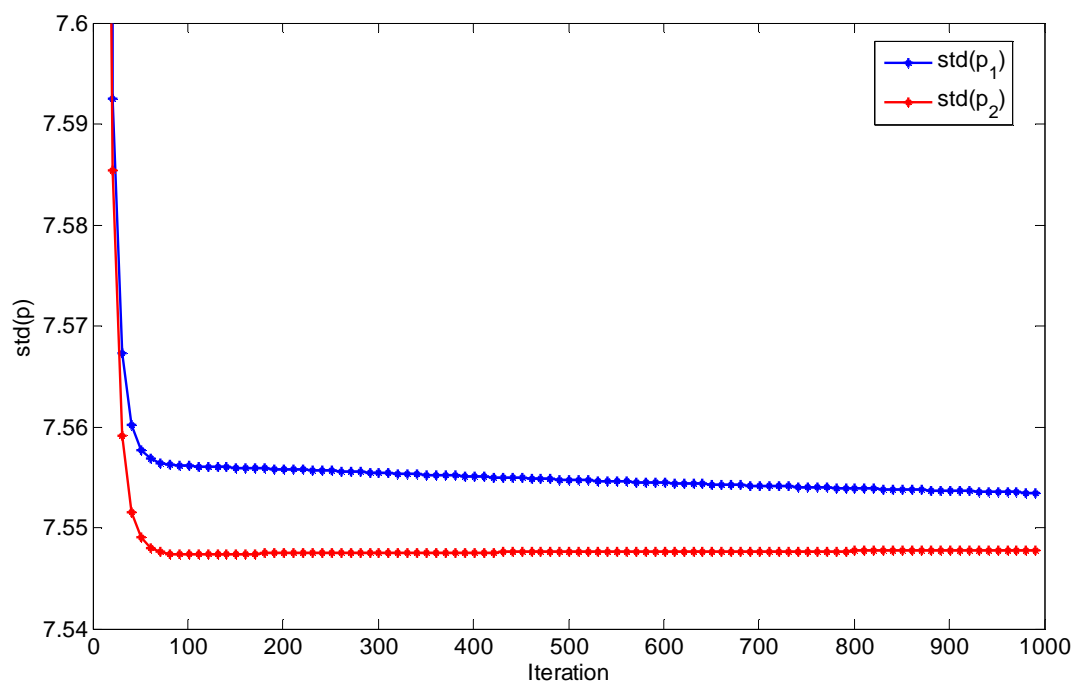


Figure 5.41. Standard deviation of the pressure as function of iterations for both approaches.

Figure 5.42 presents the sum of the square of the velocity at each point of the domain as function of the iteration number. The sum of the square of the velocity multiplied by  $dx \cdot dr$  gives the kinetic energy of the flow. Both approaches achieve similar values.

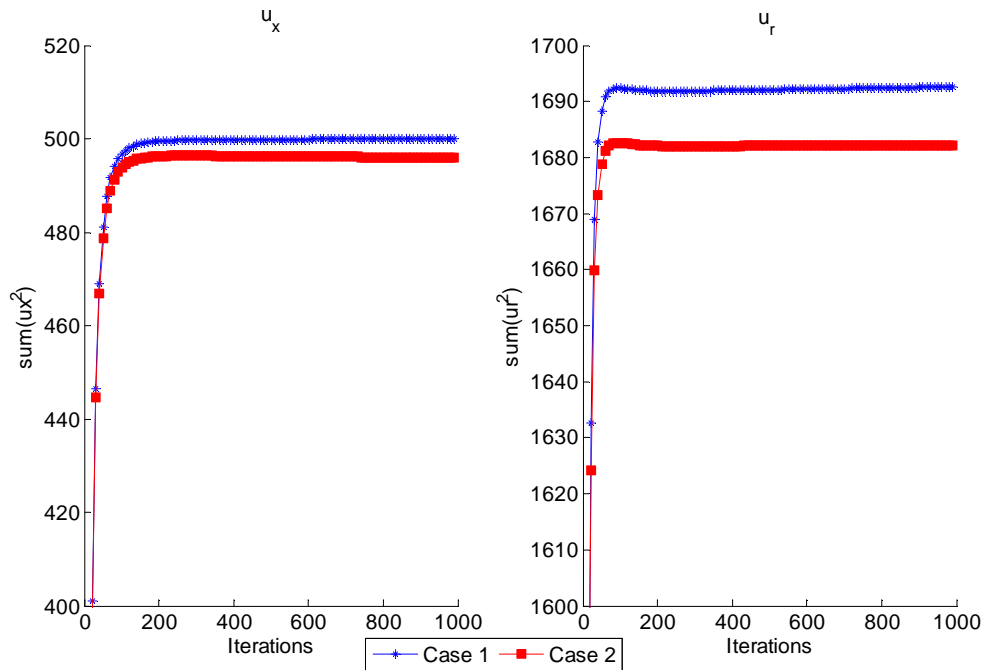


Figure 5.42. Sum of the square of the velocity at every cell.

Percentage differences among the monitored quantities are shown in Figure 5.43.

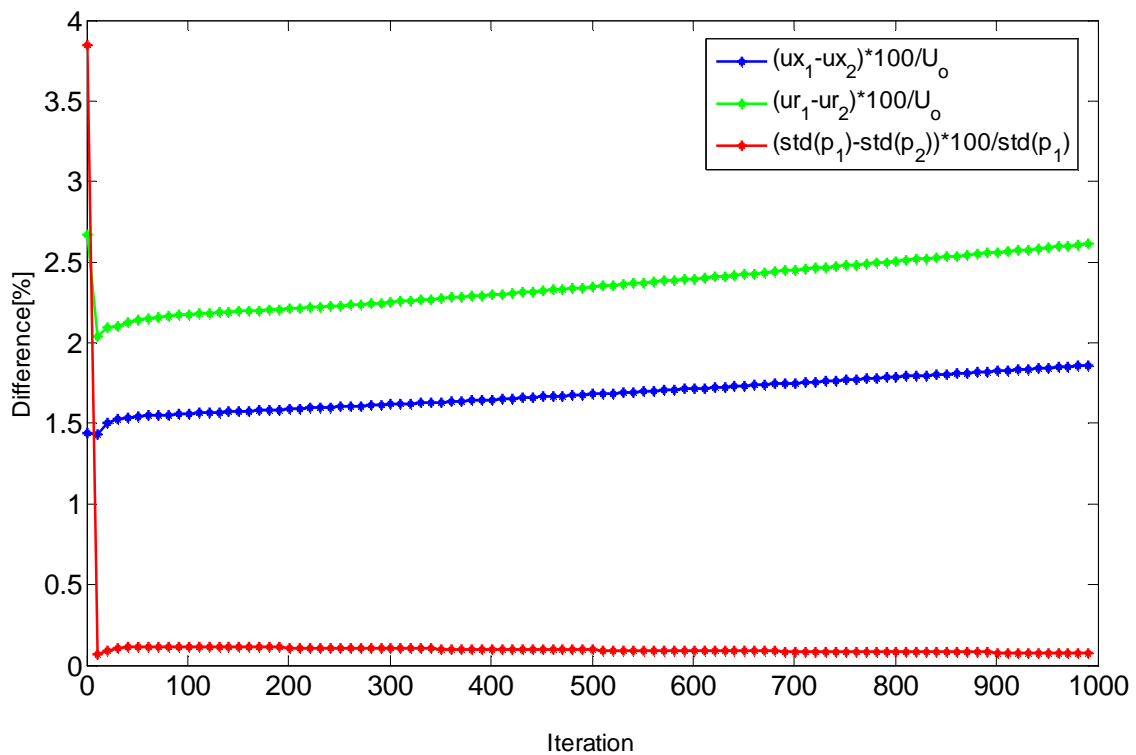


Figure 5.43. Difference of the standard deviation of the pressure and the square of the velocity between both approaches.

#### 5.6.4.3 Case 3b. Circle in presence of a vortex

Choosing an appropriate position for the vortex and the circle, the flow analysis in presence of a vortex can provide valuable information of the code behavior in terms of symmetry. As section 5.6.4.2.2 concludes that it is better to leave free the internal points of the body, the results here presented do not impose any condition at the inner points. Vortex and circle are placed at the same vertical, so the resultant flow should be symmetric with respect to the vertical axis as Figure 5.44 shows.

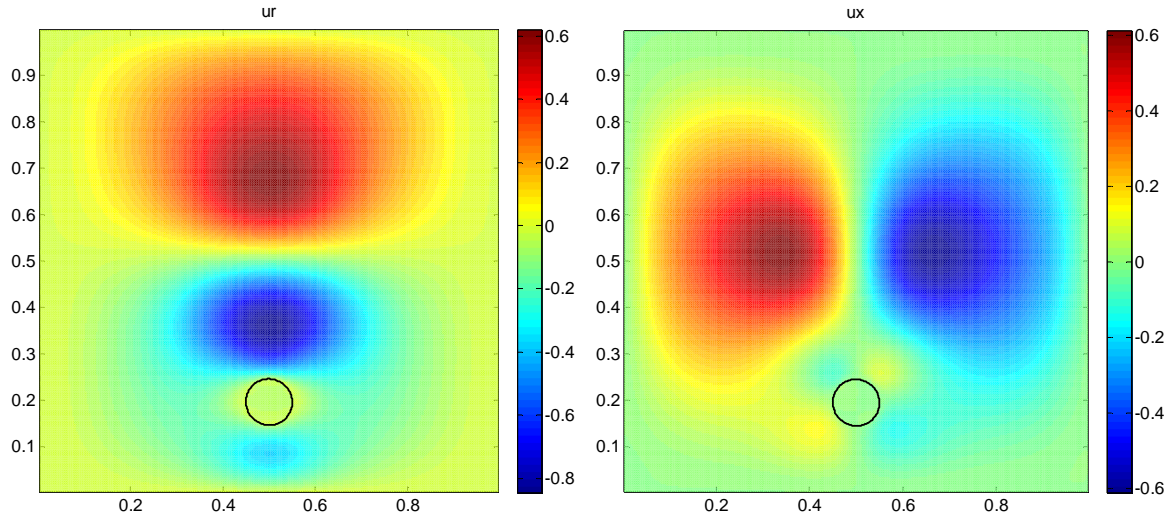


Figure 5.44. Velocity in r (left) and x (right) direction. Vortex and circle placed at the same vertical

The representation of the velocity vectors field provides an easier outstanding of the flow behavior.

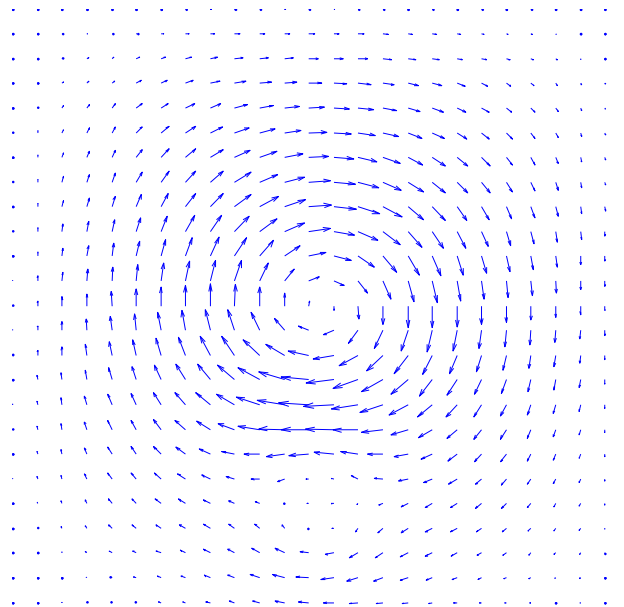


Figure 5.45. Velocity vectors field.

Section 5.6.2 points out the significance of vorticity, so this magnitude is here analyzed too. Figure 5.46 plots the vorticity distribution. As expected, it is symmetric with respect to the vertical axis which goes through the center of the core and the circle.



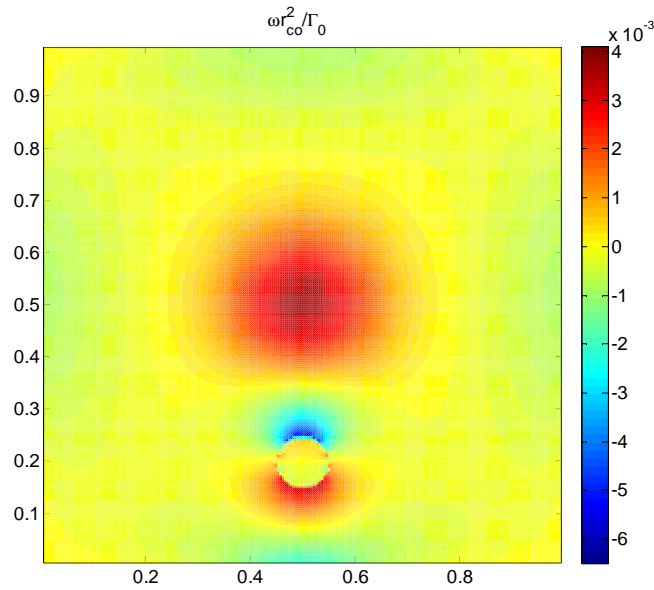


Figure 5.46. Vorticity. Vortex and circle placed at the same vertical

#### 5.6.4.4 Cases 3c and 3d. Moving circle

##### 5.6.4.4.1 Translation movement

Although the immersed boundary imposition needs to be improved before being able to accurately describe the behavior of a moving body introduced into the domain, it is possible to check if everything done until the moment is coherent.

The first trivial verification to perform is just checking that if a static body is introduced in a stand flow, the velocity and pressure solution is zero. This test assures that the introduction of an immersed boundary does not affect the solution or introduce unknown terms that could be omitted if this simple check is not performed.

One more aspect to define is the resolution at the border. The geometry and way of defining the points to impose the boundary conditions play a key role when the flow is produced due to the movement of the immersed boundary. Figure 5.47 presents the velocity in  $r$  direction, when a body moving at  $u_r = 1$  is introduced in the flow. The border is correctly defined, but at certain angles (especially at  $90^\circ$  and  $270^\circ$ ) there are points of the border where the velocity is not imposed.

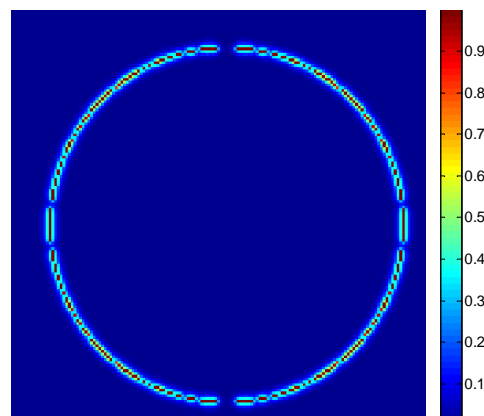


Figure 5.47. Boundary velocity.

Figure 5.48 presents the velocity field produced when a moving circle is introduced in the domain. The circle is moving in  $r$  direction at a speed  $u_r=0.05$ .

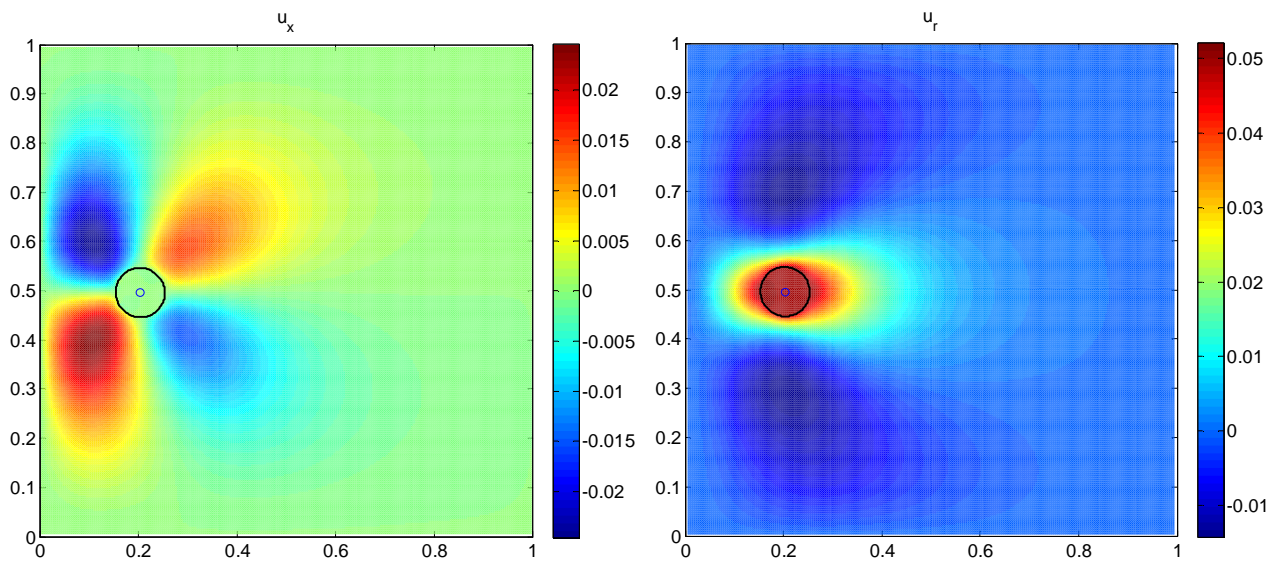


Figure 5.48. Velocity in  $x$  and  $r$  direction. Circle moving on  $r$  direction at  $u_r=0.05$ .

The representation of the velocity as a vector provides a faster interpretation. Figure 5.49 presents the velocity vectors field. On the left side, the absolute velocity is plotted. On the right, the velocity of the moving body is subtracted to de velocity field.

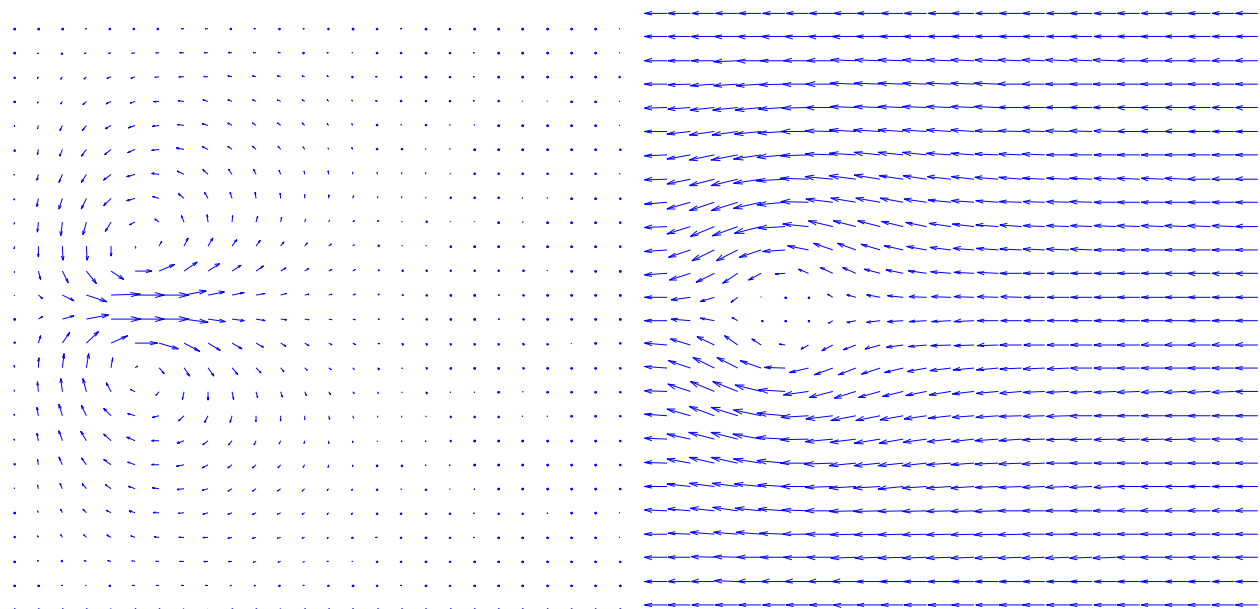


Figure 5.49. Velocity vectors. Absolute velocity (left) and relative velocity (right)

Once the velocity field is known, the calculation of the stream function is immediate. Figure 5.50 presents the stream function.

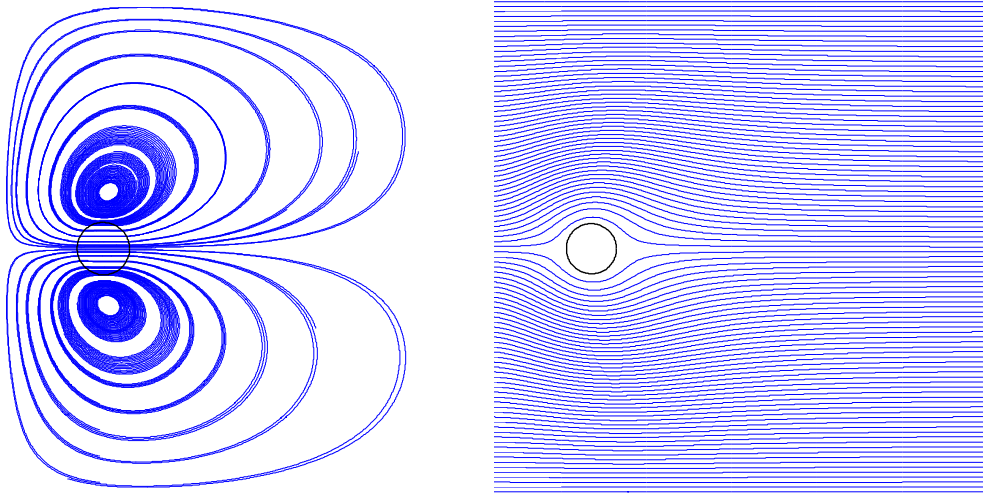


Figure 5.50. Stream lines. Absolute value (left) and relative value (right)

Figure 5.51 plots the pressure distribution. As the circle is moving to the right, an overpressure appears on the right part of the circle while the pressure on the left decreases.

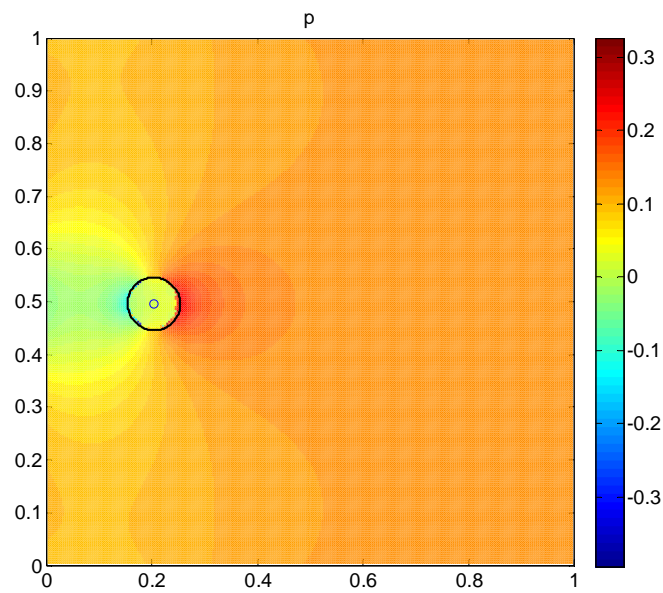


Figure 5.51. Pressure distribution

#### 5.6.4.4.2 Rotation movement

This section analyses what happens when the circle is moving at a constant rotation speed. Due to the geometry and the fact that there is not translation movement, the boundary position does not change with time so the problem can be solved with less computational effort: the interpolation coefficients and positions of the boundary points only need to be calculated once. The problem now arises with resolution. As the movement of the flow is initiated due the viscous efforts that appear because of the rotation of the circle, the viscous boundary layer plays a main role. In order to solve this boundary layer, a lot of points are required in the vicinity of the boundary and it is not feasible to solve the problem with the current implementation. Figure 5.52 presents the velocity distribution in x and r direction.

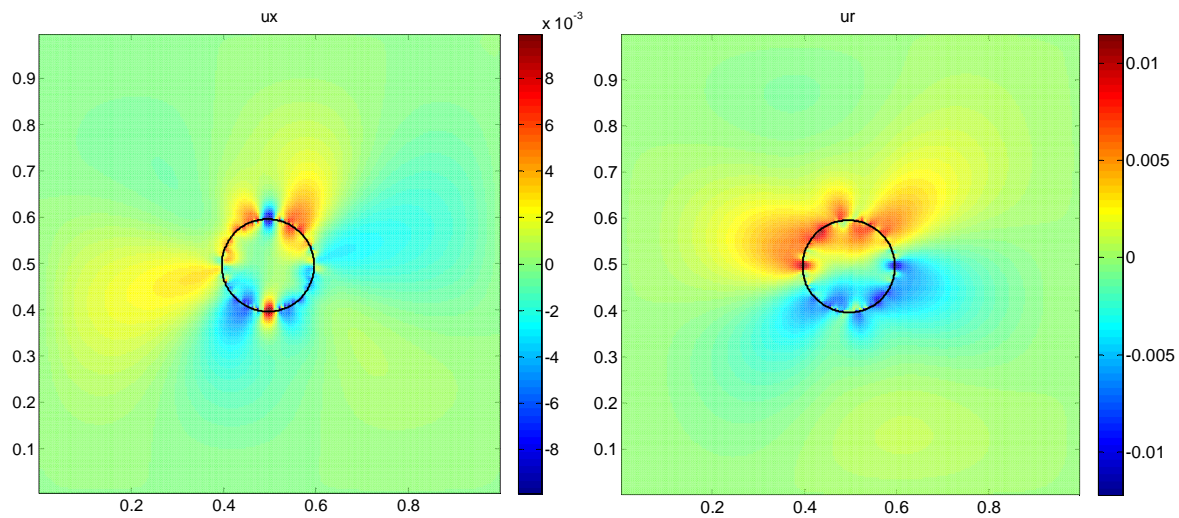


Figure 5.52. Velocity. Circle rotating at a speed  $w=CFL$

Plotting the velocity vectors it can be appreciated how flow is not adapted to the conditions imposed by the body.

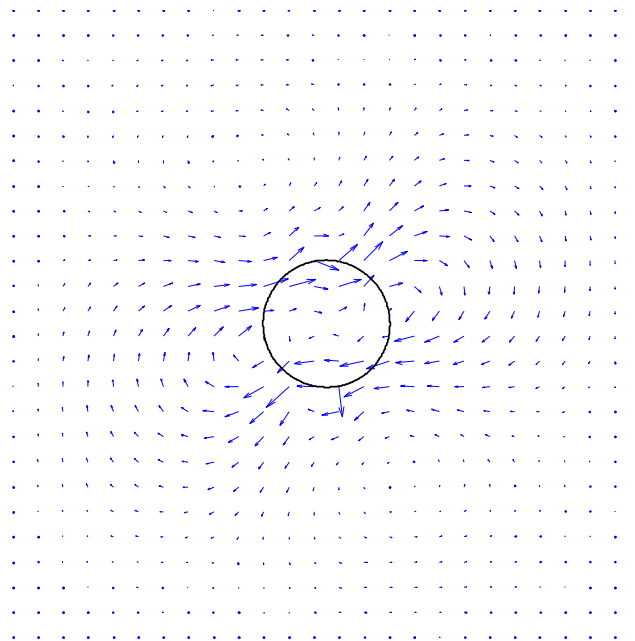


Figure 5.53. Velocity vectors

# Chapter 6

---

## 6 Conclusions and future work

This chapter remarks the conclusions reached along the work and the future lines to address the issues raised.

### 6.1 Conclusions

In the present work we have developed a 2D solver of the Navier-Stokes equations with an immersed boundary method to model complex boundaries. This solver is the first step towards the simulation of the filling process of the left ventricle. The main conclusions that can be extracted from this work are sorted in three groups. The first one corresponds to the immersed boundary method, the second one to the solution of the linear system of equations and the third one corresponds to the integration scheme.

1. Immersed boundaries

- a. The usage of the immersed boundary method enables to handle moving boundaries with less computational cost than competing methods.
- b. Having studied the available approaches to impose immersed boundaries, we conclude that direct forcing imposition is simpler and more efficient.
- c. Inverse weighting distance method is a simple approach to interpolate the boundary conditions with an acceptable accuracy.
- d. Regarding the internal treatment of the body, the best approach is leaving the interior of the body free to develop a flow without imposing any restriction other than the boundary



condition. The imposition of a forcing inside the body makes the problem more rigid and promotes the appearance of spurious pressure peaks.

2. Solution of the linear system of equations
  - a. Direct methods are prohibitively expensive when the number of variables is large.
  - b. Traditional iterative methods such as Jacobi and Gauss Seidel, without preconditioning, require too many iterations to reach the solution. They are not a competitive alternative to direct methods.
  - c. Sparse iterative methods are beneficial because they require less computer data usage.
  - d. Krylov subspace iterative methods, even with the simplest preconditioning scheme, are more adequate to solve the linear system of equations.
3. Temporal integration scheme
  - a. We implemented an integration method consisting of a fractional-step method in combination with a semi-implicit Runge-Kutta method achieves third order precision in the convective terms and second order in viscous and pressure terms, requiring lower storage capability than traditional third order Runge-Kutta methods.
  - b. The implemented fractional-step Runge-Kutta method allowed us to work with longer time steps than other methods, thereby decreasing the computational cost of the problem.
  - c. The method is compatible with the immersed boundary method because the pressure correction does not change the velocity imposed at the boundary.

## 6.2 Future work

In order to achieve the eventual aim of simulating numerically the filling process of the left ventricle, future work should address the following tasks:

1. To refine the immersed boundary method for moving geometries. This task will be accomplished by the following sub-tasks:
  - a. To fully understand the problems shown in the examples. In particular, we have to determine if the problem that arises in the rotational circle is solved when the size of the mesh decreases.
  - b. To develop a tool that enables the introduction of a general geometry and identifies the points to impose the boundary conditions.
  - c. To study the possibility of using different interpolation techniques which increase the accuracy.
2. To extend the implementation to three dimensions for axisymmetric geometries. The use of a mesh with axial symmetry is important because of two reasons:
  - a. It is compatible with the work performed until the moment.
  - b. It allows using of Fourier Spectral Method in the azimuthal direction. Using Fourier, we are exact on the derivatives calculations and the matrices that correspond to the viscous terms in the third direction are diagonal. Thus, instead of solving a system of dimension  $n^3$ , we can solve  $n$  systems of size  $n^2$ , which is much simpler.

The singularity that appears in axisymmetric geometries at  $r=0$  needs to be solved.

3. To develop a Multigrid Method to solve the linear system of discretized equations. The use of Multigrid Method will accelerate the convergence rate of the iterative method that currently solves the system of linear equations.
4. To parallelize the code to allow for multi-processor simulations dividing the large problem into smaller ones than can be solved concurrently.





# References

---

1. [www.cureresearch.com](http://www.cureresearch.com). Last visit: 10-10-2010
2. Kenchaiah S, Narula J, Vasan R. Risk factors of Heart Failure. Medical Clinics of North America. 2004;202;8:1145+.
3. Barker W, Mullooly J, Getchel W. Changing incidence and survival of heart failure in a well defined older population, 1970-1974 and 1990-1994. Circulation. 2006;119.
4. [www.who.int](http://www.who.int). [World Heart Organization]. Last visit: 10-10-2010
5. Owan TE, Hodge DO, Herges RM, Jacobsen SJ, Roger VL, Redfield MM. Trends in prevalence and outcome of heart failure with preserved ejection fraction. New England Journal of Medicine. 2006;355(3):251-9.
6. Bolger AF, Heiberg E, Karlsson M, Wigstrom L, Engvall J, Sigfridsson A, et al. Transit of blood flow through the human left ventricle mapped by cardiovascular magnetic resonance. J Cardiovasc Magn Reson. 2007;9(5):741-7.
7. Watanabe H, Sugiura S, Hisada T. The looped heart does not save energy by maintaining the momentum of blood flowing in the ventricle. American Journal of Physiology-Heart and Circulatory Physiology. 2008;294(5):H2191-H6.
8. Kilner PJ, Yang GZ, Wilkes AJ, Mohiaddin RH, Firmin DN, Yacoub MH. Asymmetric redirection of flow through the heart. Nature. 2000;404(6779):759-61.
9. Sengupta PP, Khandheria BK, Korinek J, Jahangir A, Yoshifuku S, Milosevic I, et al. Left ventricular isovolumic flow sequence during sinus and paced rhythms. J Am Coll Cardiol. 2007;49(8):899-908.
10. Gharib M, Rambod E, Kheradvar A, Sahn DJ, Dabiri JO. Optimal vortex formation as an index of cardiac health. Proceedings of the National Academy of Sciences of the United States of America. 2006;103(16):6305-8.
11. Yotti R, Bermejo J, Antoranz JC, Desco MM, Cortina C, Rojo-Alvarez JL, et al. A noninvasive method for assessing impaired diastolic suction in patients with dilated cardiomyopathy. Circulation. 2005;112(19):2921-9.
12. Cazeau S, Leclercq C, Lavergne T, Walker S, Varma C, Linde C, et al. Effects of multisite biventricular pacing in patients with heart failure and intraventricular conduction delay. New England Journal of Medicine. 2001;344(12):873-80.

13. Abraham WT, Fisher WG, Smith AL, Delurgio DB, Leon AR, Loh E, et al. Cardiac resynchronization in chronic heart failure. *New England Journal of Medicine*. 2002;346(24):1845-53.
14. Bristow MR, Saxon LA, Boehmer J, Krueger S, Kass DA, De Marco T, et al. Cardiac-resynchronization therapy with or without an implantable defibrillator in advanced chronic heart failure. *New England Journal of Medicine*. 2004;350(21):2140-50.
15. Cleland JGF, Daubert J, Erdmann E, Freemantle N, Gras D, Kappenberger L, et al. The effect of cardiac resynchronization on morbidity and mortality in heart failure. *New England Journal of Medicine*. 2005;352(15):1539-49.
16. Chung ES, Leon AR, Tavazzi L, Sun JP, Nihoyannopoulos P, Merlino J, et al. Results of the predictors of response to CRT (PROSPECT) trial. *Circulation*. 2008;117(20):2608-16.
17. Yu CM, Fung JWH, Zhang Q, Sanderson JE. Understanding nonresponders of cardiac resynchronization therapy - Current and future perspectives. *Journal of Cardiovascular Electrophysiology*. 2005;16(10):1117-24.
18. Pavlopoulos H, Nihoyannopoulos P. Recent advances in cardiac resynchronization therapy: echocardiographic modalities, patient selection, optimization, non-responders-all you need to know for more efficient CRT. *International Journal of Cardiovascular Imaging*. 2010;26(2):177-91.
19. Zhang Q, Fung JWH, Chan YS, Chan HCK, Lin H, Chan S, et al. The role of repeating optimization of atrioventricular interval during interim and long-term follow-up after cardiac resynchronization therapy. *International Journal of Cardiology*. 2008;124(2):211-7.
20. Auricchio A, Stellbrink C, Sack S, Block M, Vogt J, Bakker P, et al. Long-term clinical effect of hemodynamically optimized cardiac resynchronization therapy in patients with heart failure and ventricular conduction delay. *Journal of the American College of Cardiology*. 2002;39(12):2026-33.
21. Sawhney NS, Waggoner AD, Garhwal S, Chawla MK, Osborn J, Faddis MN. Randomized prospective trial of atrioventricular delay programming for cardiac resynchronization therapy. *Heart Rhythm*. 2004;1(5):562-7.
22. Hoppensteadt FC, Peskin CS. *Modeling and simulation in medicine and the Life Sciences* 2000.
23. Boron WF, Boulpaep EL. *Medical Physiology*. Elsevier, editor 2003.
24. Klein AL, Burstow DJ, Tajik AJ, Zachariah PK, Bailey KR, Seward JB. Effects of age on left-ventricular dimensions and filling dynamics in 117 normal persons. *Mayo Clinic Proceedings*. 1994;69(3):212-24.
25. [www.cvr.com](http://www.cvr.com). Last visit: 21-09-2010
26. Fung YC. *Biomechanics : circulation*. 2nd ed. New York: Springer; 1997.
27. Cecil RL, Bennett JC, Plum F. *Cecil textbook of medicine*. Philadelphia, Pa.: W.B. Saunders.
28. [www.health.com](http://www.health.com). Last visit: 23-09-2010
29. [www.cvphysiology.com](http://www.cvphysiology.com). Last visit: 05-10-2010
30. [www.vilastic.com](http://www.vilastic.com). Last visit: 23-09-2010
31. Garcia MJ, Smedira NG, Greenberg NL, Main M, Firstenberg MS, Odabashian J, et al. Color M-mode Doppler flow propagation velocity is a preload insensitive index of left ventricular relaxation: Animal and human validation. *Journal of the American College of Cardiology*. 2000;35(1):201-8.
32. Hong G-R, Pedrizzetti G, Tonti G, Li P, Wei Z, Kim JK, et al. Characterization and Quantification of Vortex Flow in the Human Left Ventricle by Contrast Echocardiography Using Particle Image Velocimetry. *J Am Coll Cardiol Img*. 2008;1(6):705-17.
33. Verma A, Solomon SD. Diastolic Dysfunction as a Link Between Hypertension and Heart Failure. *Medical Clinics of North America*. 2009;93(3):647-+.
34. Nikitin NP, Witte KKA. Application of tissue Doppler imaging in cardiology. *Cardiology*. 2004;101(4):170-84.
35. Jacobs LE, Kotler MN, Parry WR. Flow patterns in dilated cardiomyopathy: a pulsed-wave and color flow Doppler study. *J Am Soc Echocardiogr*. 1990;3(4):294-302.
36. Brun P, Tribouilloy C, Duval AM, Iserin L, Meguira A, Pelle G, et al. Left-ventricular flow propagation during early filling is related to wall relaxation - a color m-mode doppler analysis. *Journal of the American College of Cardiology*. 1992;20(2):420-32.

37. Vierendeels JA, Dick E, Verdonck PR. Hydrodynamics of color M-mode Doppler flow wave propagation velocity  $V(p)$ : A computer study. *Journal of the American Society of Echocardiography*. 2002;15(3):219-24.
38. Steen T, Steen S. Filling of a model left-ventricle studied by color m-mode doppler. *Cardiovascular Research*. 1994;28(12):1821-7.
39. Stugaard M, Brodahl U, Torp H, Ihlen H. Abnormalities of left-ventricular filling in patients with coronary-artery disease - assessment by color m-mode doppler technique. *European Heart Journal*. 1994;15(3):318-27.
40. Stugaard M, Smiseth OA, Risoe C, Ihlen H. Intraventricular early diastolic velocity profile during acute myocardial ischemia: a color M-mode Doppler echocardiographic study. *J Am Soc Echocardiogr*. 1995;8(3):270-9.
41. Garcia MJ, Palac RT, Malenka DJ, Terrell P, Plehn JF. Color M-mode Doppler flow propagation velocity is a relatively preload-independent index of left ventricular filling. *Journal of the American Society of Echocardiography*. 1999;12(2):129-37.
42. Abali G, Tokgozoglu L, Ozcebe OH, Aytemir K, Nazli N. Which Doppler parameters are load independent? A study in normal volunteers after blood donation. *Journal of the American Society of Echocardiography*. 2005;18(12):1260-5.
43. Asada-Kamiguchi J, Tabata T, Popovic ZB, Greenberg NL, Kim YJ, Garcia MJ, et al. Non-invasive assessment of left ventricular relaxation during atrial fibrillation using mitral flow propagation velocity. *European Journal of Echocardiography*. 2009;10(7):826-32.
44. Klein AL, Garcia MJ. *Diastology : clinical approach to diastolic heart failure*. 1st ed. Philadelphia: Saunders/Elsevier; 2008.
45. Otto CM. *Textbook of clinical echocardiography*. 3rd ed. Philadelphia, Pa.: Saunders; 2004.
46. Roelandt J, Pozzoli M. *Non-Invasive Assessment of Left Ventricular Diastolic (Dys) Function and Filling Pressure*.
47. Iyengar S, Abraham WT. Cardiac resynchronization therapy - A better and longer life for patients with advanced heart failure. *Circulation*. 2005;112(13):E236-E7.
48. Auricchio A, Stellbrink C, Block M, Sack S, Vogt J, Bakker P, et al. Effect of pacing chamber and atrioventricular delay on acute systolic function of paced patients with congestive heart failure. *Circulation*. 1999;99(23):2993-3001.
49. Kedia N, Ng K, Apperson-Hansen C, Wang CH, Tchou P, Wilkoff BL, et al. Usefulness of atrioventricular delay optimization using Doppler assessment of mitral inflow in patients undergoing cardiac resynchronization therapy. *American Journal of Cardiology*. 2006;98(6):780-5.
50. Aronoff RD, Zoghbi WA, Rokey R, Bolli R, Quinones MA. Assessment of diastolic pressure-volume relation in the intact left-ventricle by pulsed-doppler echocardiography. *Journal of the American College of Cardiology*. 1986;7(2):A244-A.
51. Kindermann M, Frohlig G, Doerr T, Schieffer H. Optimizing the AV delay in DDD pacemaker patients with high degree AV block: Mitral valve Doppler versus impedance cardiography. *Pace-Pacing and Clinical Electrophysiology*. 1997;20(10):2453-62.
52. Ritter P, Padeletti L, Gillio-Meina L, Gaggini G. Determination of the optimal atrioventricular delay in DDD pacing - Comparison between echo and peak endocardial acceleration measurements. *Europace*. 1999;1(2):126-30.
53. Mokrani B, Lafitte S, Deplagne A, Ploux S, Laborderie J, Reant P, et al. Echocardiographic study of the optimal atrioventricular delay at rest and during exercise in recipients of cardiac resynchronization therapy systems. *Heart Rhythm*. 2009;6(7):972-7.
54. Bordachar P, Lafitte S, Reuter S, Serri K, Garrigue S, Laborderie J, et al. Echocardiographic assessment during exercise of heart failure patients with cardiac resynchronization therapy. *American Journal of Cardiology*. 2006;97(11):1622-5.
55. van Gelder BM, Bracke FA, Meijer A, Lakerveld LJM, Pijls NHJ. Effect of optimizing the VV interval on left ventricular contractility in cardiac resynchronization therapy. *American Journal of Cardiology*. 2004;93(12):1500-3.

56. Sogaard P, Egeblad H, Pedersen AK, Kim WY, Kristensen BO, Hansen PS, et al. Sequential versus simultaneous biventricular resynchronization for severe heart failure - Evaluation by tissue Doppler imaging. *Circulation*. 2002;106(16):2078-84.
57. Kovacs SJ, McQueen DM, Peskin CS. Modelling cardiac fluid dynamics and diastolic function. *Philosophical Transactions of the Royal Society of London Series a-Mathematical Physical and Engineering Sciences*. 2001;359(1783):1299-314.
58. Milani RV, Lavie CJ, Mehra MR, Ventura HO, Kurtz JD, Messerli FH. Left ventricular geometry and survival in patients with normal left ventricular ejection fraction. *American Journal of Cardiology*. 2006;97(7):959-63.
59. Greenbaum RA, Ho SY, Gibson DG, Becker AE, Anderson RH. Left-ventricular fiber architecture in man. *British Heart Journal*. 1981;45(3):248-63.
60. Armour JA, Randall WC. Structural basis for cardiac function. *American Journal of Physiology*. 1970;218(6):1517-&.
61. Strobeck JE, Sonnenblick EH. Myocardial and ventricular-function .1. Isolated muscle. *Herz*. 1981;6(5):261-74.
62. Strobeck JE, Sonnenblick EH. Myocardial and ventricular-function .2. Intact heart. *Herz*. 1981;6(5):275-87.
63. Jones CJH, Raposo L, Gibson DG. Functional importance of the long axis dynamics of the human left-ventricle. *British Heart Journal*. 1990;63(4):215-20.
64. Mittal R, Iaccarino G. Immersed Boundary Methods. *Ann Rev Fluid Mech*. 2005;2005.37:239-61.
65. Kim Y, Peskin CS. Numerical study of incompressible fluid dynamics with nonuniform density by the immersed boundary method. *Physics of Fluids*. 2008;20(6).
66. Griffith BE, Hornung RD, McQueen DM, Peskin CS. An adaptive, formally second order accurate version of the immersed boundary method. *Journal of Computational Physics*. 2007;223(1):10-49.
67. Griffith BE, Peskin CS. On the order of accuracy of the immersed boundary method: Higher order convergence rates for sufficiently smooth problems. *Journal of Computational Physics*. 2005;208(1):75-105.
68. Briscolini M, Santangelo P. Development of the mask method for incompressible unsteady flows. *Journal of Computational Physics*. 1989;84(1):57-75.
69. Goldstein D, Handler R, Sirovich L. Modeling a no-slip flow boundary with an external force-field. *Journal of Computational Physics*. 1993;105(2):354-66.
70. Fadlun EA, Verzicco R, Orlandi P, Mohd-Yusof J. Combined immersed-boundary finite-difference methods for three-dimensional complex flow simulations. *Journal of Computational Physics*. 2000;161(1):35-71.
71. Ferziger JH, Peri\*\* M. Computational methods for fluid dynamics. Berlin ; New York: Springer-Verlag; 1996.
72. Spalart PR, Moser RD, Rogers MM. Spectral methods for the navier-stokes equations with one infinite and 2 periodic directions. *Journal of Computational Physics*. 1991;96(2):297-324.
73. Kim J, Moin P. Application of a fractional-step method to incompressible navier-stokes equations. *Journal of Computational Physics*. 1985;59(2):308-23.
74. Verzicco R, Orlandi P. A finite-difference scheme for three-dimensional incompressible flows in cylindrical coordinates. *Journal of Computational Physics*. 1996;123(2):402-14.
75. S. M, G. I, PA. D. RANS solver with adaptive structured boundary non-conforming grids. *Annu Res Briefs, Cent Turb Res*. 2001:353-64.
76. Shepard D. A two-dimensional interpolation function for computer mapping of irregularly spaced data. A two-dimensional interpolation function for computer mapping of irregularly spaced data. 1968:21.
77. Foley TA, Lane DA, Nielson GM, Franke R, Hagen H. Interpolation of scattered data on closed surfaces. *Computer-Aided Geometric Design*. 1990;7(1-4):303-12.
78. Franke R. Scattered data interpolation - tests of some methods. *Mathematics of Computation*. 1982;38(157):181-200.
79. Tseng YH, Ferziger JH. A ghost-cell immersed boundary method for flow in complex geometry. *Journal of Computational Physics*. 2003;192(2):593-623.

80. Saad Y, van der Vorst HA. Iterative solution of linear systems in the 20th century. *Journal of Computational and Applied Mathematics*. 2000;123(1-2):1-33.
81. Young DM. A historical overview of iterative methods. *Computer Physics Communications*. 1989;53(1-3):1-17.
82. [www.cs.colorado.edu](http://www.cs.colorado.edu). Last visit: 15-10-2010
83. Saffman PG. *Vortex dynamics*. 1st pbk. ed. Cambridge ; New York: Cambridge University Press; 1995.